Inducing Chirality in CdS Nanocrystals with Biomolecules

Christopher Lowe

A dissertation

submitted in partial fulfillment of the

requirements for the degree of

Doctor of Philosophy

University of Washington

2026

Reading Committee:

Brandi M. Cossairt, Chair

David Ginger

Dianne Xiao

Program Authorized to Offer Degree:

Chemistry

University of Washington

Abstract

Inducing Chirality in CdS Nanocrystals with Biomolecules

Christopher Lowe

Chair of the Supervisory Committee:
Brandi M. Cossairt
Department of Chemistry

Chiral CdE (E=S, Se, Te) nanocrystals (NCs) are an emerging class of materials with potential applications in optoelectronics, bioimaging, and sensing. Among the strategies for generating chiral CdE NCs, which include 1) chiral molecule templated nucleation and growth, 2) assembly of CdE NCs into chiral arrangements, and 3) chiral ligand exchange on the surface of the NCs, the latter is most attractive for biological applications because it enables direct interfacing between high-quality NCs and chiral biomolecules. Although ligand exchange with cysteine has been shown to induce chirality in CdE NCs, no prior studies have demonstrated the use of intrinsically chiral biomolecules, like peptides and proteins, to generate chiroptical responses in these materials.

Chapter 1 reviews the synthetic tunability of CdE NCs and current approaches of synthesizing chiral nanostructures. It then introduces the structural complexity of biomolecules and highlights existing strategies for assembling hybrid biomolecule:CdE systems. The relevant

chiral length scales of proteins and NCs are compared, motivating an interfacing strategy that couples biomolecular chirality with the surface-sensitive electronic structure of CdE NCs.

Chapter 2 establishes an aqueous ligand exchange process in which glycine (the only achiral amino acid) serves as a versatile intermediate for displacement by cysteine (Cys)-containing elastin-like polypeptides. This exchange results in clear chirality transfer, evidenced by circular dichroism (CD) signals at the QD electronic transitions. The resulting polypeptide-bound QDs also exhibit thermally reversible coacervation, characterized by dynamic light scattering (DLS), small-angle X-ray scattering (SAXS), and transmission electron microscopy (TEM).

Chapter 3 extends this glycine-mediated exchange strategy to CdS nanorods (NRs) and examines how Cys concentration and local coordination environment influence NR optical properties, including UV-Vis absorbance, CD, and photoluminescence. These studies reveal that Cys derivatives can be detected at μM concentrations and suggest that both internal and n-terminal Cys residues are capable of inducing strong chiroptical responses.

Chapter 4 applies these insights to protein-induced chirality in glycine-capped CdS NRs of two lengths. Incubation with a designed helical repeat protein containing four internal Cys residues (DHR-4Cys) rapidly displaces glycine and produces CD signals corresponding to the NR electronic transitions. NR length is found to have minimal influence on the resulting *g*-factors. TEM analysis reveals a substantial protein-derived ligand shell, and secondary structure analysis confirms that the protein remains folded upon binding. Remarkably, induced chirality is observed at nM protein loadings, corresponding to roughly two proteins per NR. This work represents the first demonstration of chirality induction in CdE NCs using an ordered protein scaffold.

TABLE OF CONTENTS

LIST OF FIGURES

LIST OF TABLES

DEDICATION

Obtaining a PhD has been an incredible journey that would not have been possible without the support of friends in family. First, I would like to thank my partner Rachelle, without your unwavering support this would not have been possible. We shared laughs and tears throughout this journey, and I am truly appreciative. To my parents Dave and Sonja, thank you for believing in me and supporting my academic journey. I took inspiration from both of your work ethic to complete this journey. To my siblings Kayla, Derek, and Dylan, thank you for the laughs and keeping me humble during my journey. To my work friends, thank you all for making graduate school more enjoyable and for your conversation. While there are many more than I have space to write in this section, I want to highlight some of the most memorable here. Alex, Maria and Dylan, thank you for your scientific support in my early graduate school career. You 3 showed me how to be an independent scientist. For those that I had the pleasure of working alongside in the Cossairt group, thank you all for welcoming me into the lab mid-grad school. Soren, your work-ethic inspired me throughout grad school to dig a little deeper, thank you for always bringing energy and laughs to the lab. Emi, thank you for teaching me how to be a good scientist, I always admired your work ethic and thank you for letting me make bad jokes in the office (and of course being IT). Hao, thank you for your friendship during this time, you are one the most impressive people I have worked with (you truly earned the nickname “boss”) and I always enjoyed talking tennis with you. Emily, thank you for your friendship, you were always incredibly caring and willing to listen. Sam, thank you for your spectroscopic knowledge and sense of humor. Izzy, thank you for being an incredible undergraduate researcher, I have no doubt that one day you will be writing one of these if you choose to continue your academic career. To Catie, Elise and Pedro, thank you three for the laughs and good science conversations

in the office, I am going to miss these interactions. Helen, thank you for welcoming me into the lab and teaching me about nanocrystal chemistry and your passion for TEM imaging. Florence, thank you for always bringing positive energy, I really enjoyed our conversations and appreciated how difficult your work was. Hunter and Micaela, thank you both for being available to help me in my scientific struggles. To Brandi, thank you for believing in me when I was doubting my abilities. You welcomed me into your lab mid-grad school when I had no nanocrystal chemistry experience. This journey would not have been possible without your mentorship and guidance

Chapter 1. INTRODUCTION TO CHIRAL CADMIUM CALCHOGENIDE NANOCRYSTALS

This chapter introduces the scientific context for the work presented in Chapters 2-4, which focuses on the emergence of chiroptical properties in CdS nanocrystals (NCs) when interfaced with polypeptides and proteins. To establish the foundation for these studies, we first outline the synthetic tunability of quantum confined semiconductor NCs, the structural diversity of biomolecular architectures, and current strategies for interfacing NCs with biomolecules. We then discuss chirality in both proteins and quantum confined NCs, setting the stage for understanding how biomolecules can impart new optical properties to inorganic nanomaterials.

1.1 QUANTUM CONFINED SEMICONDUCTOR NANOCRYSTALS

Quantum confined CdE (E=S, Se, Te) nanocrystals (NCs) are widely used in light-emitting diodes (LEDs),[1] photodetectors,[2] bioimaging,[3] catalysis,[4] and more.[5,6] Their defining feature is a size-dependent electronic structure that gives rise to discrete absorbance transitions (**Figure 1A**). These transitions originate from multiple non-degenerate near-band-edge orbitals (**Figure 1A inset**), which become quantized as the NC dimensions approach the exciton Bohr radius.[7] The ability to tune these optical properties through synthetic control has driven major advances in CdE quantum dot (QD) chemistry.[5]

A key consequence of quantum confinement is that the lowest energy UV-Vis absorbance transition provides a direct probe of QD size.[8] Peng and coworkers demonstrated that by adjusting precursor concentration, reactivity, and reaction temperatures, CdE QD growth can be monitored in real time.[9] For example, the evolution of CdS QD size over several hours can be

tracked through systematic shifts in the first excitonic absorbance feature (**FIGURE 1B**), allowing for precise size selection from ~2-5 nm.[8]

Beyond size control, synthetic advances have allowed for access to distinct crystal phases of CdE QDs, each with characteristic surface facets. Under kinetically controlled conditions and lower reaction temperatures, zinc blend CdE QDs form with two predominant facet types (**Figure 1Ci**). These include cadmium- and chalcogenide-rich {100} and {111} facets, which carry positive or negative surface charge, respectively.[10] The relatively uniform expression of these polar facets can direct growth into cubes, tetrahedra, and tetrapods.[10]

At higher temperatures or with more reactive precursors, the thermodynamically favored wurtzite phase is obtained (**Figure 1Cii**).[11–13] Wurtzite NCs expose different polar facets ({001} and {101}) and a stoichiometric nonpolar {100} facet.[12] The anisotropic distribution of these facets enables controlled uniaxial growth into nanorods (NRs), as first demonstrated by Alivisatos and coworkers (**Figure 1Ciii**).[14] In this growth mechanism, strongly bound ligands passivate the nonpolar facets, while partial passivation of the polar facets allows directional growth oriented along one axis.[12] CdSe NRs also exhibit linearly polarized emission due to reconfiguration of the frontier orbitals in the conduction band, making them attractive for liquid crystal display technologies.[15,16]

Another advantage of CdE NCs is their solution processability. Surface atoms of both zinc blend and wurtzite CdE NCs possess under-coordinated surface atoms that require ligand passivation for colloidal stability.[17] Hydrophobic ligands with long alkyl chains and anionic headgroups (e.g., carboxylates, phosphonates, thiolates) bind surface cadmium sites, stabilizing the NCs and influencing their electronic structure.[17] Because ligands modulate surface charge,

orbital energies, and facet expression, they play a central role in tuning NC optical properties and enabling their incorporation into inorganic-organic hybrid materials.

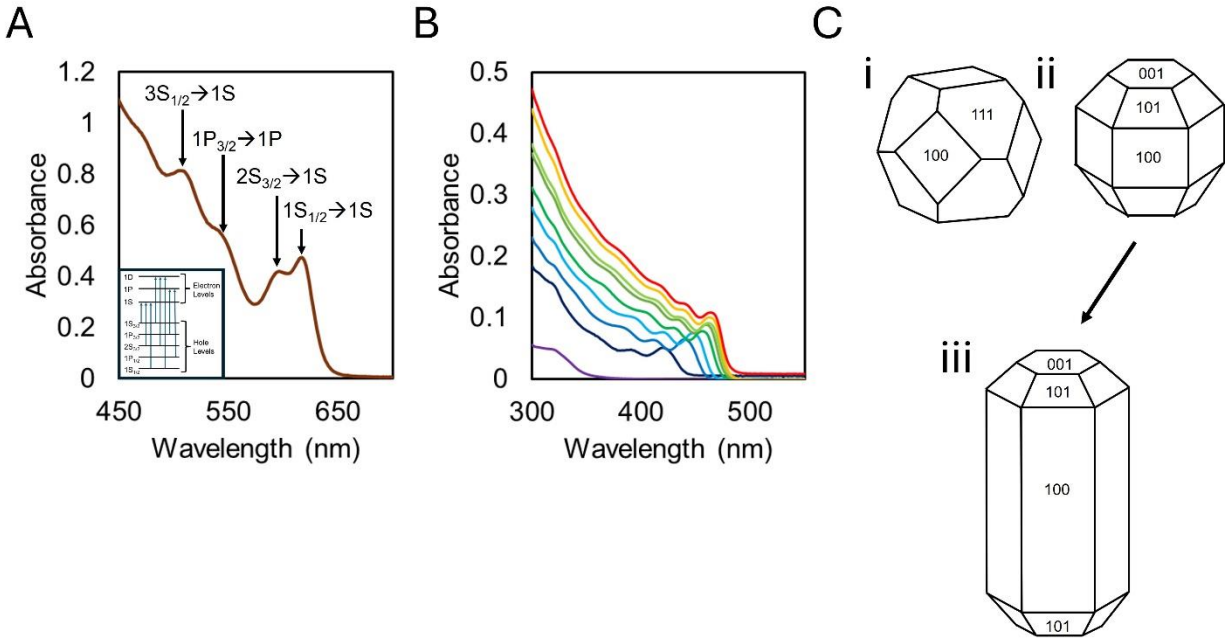

Figure 1.1 (A) Typical UV-Vis absorbance spectrum of CdSe QDs labelled with corresponding hole→electron transition levels and the general band structure of CdSe absorbance transitions (inset).[7] (B) UV-Vis absorbance spectra monitoring the growth of CdS QDs from the earliest aliquot (violet) to the final aliquot (red). (C) (i) Zinc blend CdE QD with 100 and 111 facets.[10] (ii) Simplified wurtzite CdE QD with 001 and 101 polar facets and non-polar 100 facets.[13] (iii) wurzite CdE NR with elongated 100 non-stoichiometric facet and polar 001 and 101 facets on the end of the NC.[12]

1.2 Biomolecule Architectures

Biomolecules such as DNA, proteins, and poly-N-substituted glycines (peptoids) are sequence-defined polymers whose structures are programmed by their chemical composition and assembly conditions. Their ability to form predictable, hierarchical architectures makes them powerful scaffolds for organizing inorganic nanomaterials. DNA offers some of the most

elaborate 2D assemblies due to the orthogonality of Watson-Crick base pairing. This property has enabled the development of complex DNA origami designs (**Figure 1.2A**).[18] These assemblies reliably adopt their target geometries because the hydrogen-bonding interactions that drive folding are both directional and programmable.[19] These assemblies often arise from the intrinsic charge distribution across protein surfaces, enabling predictable face to face interactions that stabilize extended structures. Peptoids provide a third route to programmable architectures. Their side chain diversity and backbone flexibility allow solvent interactions and sequence design to dictate morphological outcomes, including sheets, tubes, and other nanoscale assemblies (**Figure 1.2B**).[20] Because peptoids lack backbone chirality, their structures are governed primarily by side-chain chemistry and packing interactions.[21] Proteins can also access large-scale architectures, but through different interactions. Covalent side-chain chemistry and electrostatic complementarily drive proteins to assemble into ordered 2D arrays or crystalline lattices (**Figure 1.2C**).[22] Together, these examples illustrate the breadth of structural control available in biomolecular systems. Their tunable architectures, spanning nanometer to micron length scales, provide a versatile design space for organizing inorganic nanocrystals and motivating the hybrid materials explored in later chapters.

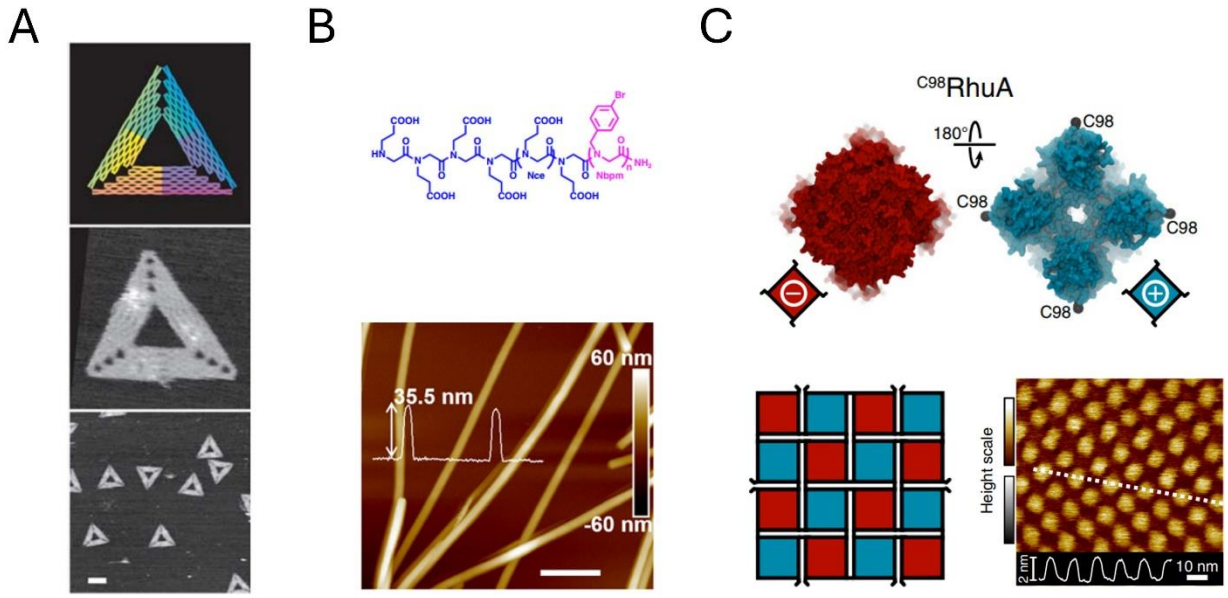

Figure 1.2 (A) Triangular DNA origami. (top) colored design diagram showing where DNA helices touch and bend apart (red is the first base pair, purple is the 7,000th). (middle) Zoomed in AFM image (165x165 nm) of DNA origami triangles. (bottom) representative AFM image of triangles. Scale bar 100 nm.[18] (B) (top) di-block peptoid sequence used in peptoid nanotube (PNT) assembly. (bottom) AFM height image showing assembled PNT in water, scale bar 500 nm.[20] (C) (top) C98RhuA electrostatic potential maps showing the C-terminal face as negatively charged (red) and the N-terminal face as positively charged (blue). (bottom left) schematic of assembled ^{C98}RhuA into solution-assembled close packed crystals. (bottom right) AFM topograph showing close-packed assembled ^{C98}RhuA.[22] Adapted from ref 18, 20 and 22.

1.3 Interfacing CdE-Biomolecule Materials

Ideal inorganic-biomolecule hybrid materials synergistically combine inorganic functionality with sequence-defined biomolecule structure and function. For the purposes of this thesis, we will introduce the work done specifically on the interfacing of CdE NCs and biomolecules. A key challenge in creating CdE-biomolecule hybrid materials is encoding desired

CdE interfacial interaction within the biomolecule sequence. Broadly, there are two general strategies of directing these interactions: 1) indirect ligand-mediated interactions and 2) direct interfacing of biomolecule onto the CdE NC surface.

Perhaps the most elaborate indirect ligand-mediated interaction example was reported by Bathe and coworkers who used 2D DNA origami architectures to orient CdSe/CdS QDs and NRs in extended 2D arrays (**Figure 1.3A**).[23] In this work, cysteine (Cys) modified single strand DNA (ssDNA) was conjugated to the QDs and NRs followed by assembly onto the origami architecture via matching base pair interactions on unhybridized DNA in the center of the origami. By passivating the CdE with ssDNA, this approach relies on the orthogonal electrostatic interactions of base pairs in the ssDNA on CdE and ssDNA in the rhomboid structures.

Similarly, Cossairt and coworkers reported the assembly CdSe QDs onto preformed peptoid tubes (**Figure 1.3B**).[24] In this example, Cys-capped CdSe QDs were conjugated to maleimide-containing peptoid tubes via click chemistry. More specifically, this report utilizes the Cys ligand on the CdSe surface to form covalent C-S bonds with maleimides on the peptoid surface. In this work, indirect, ligand-mediated covalent bonding drives the interfacing of CdE with biomolecules.

Finally, Liu et al. report direct interfacing of CdTe QDs with proteins for light harvesting (**Figure 1.3C**).[25] Here, negatively charged carboxylate groups in the pore of the protein hoops interact directly with the positively charged CdTe QD surface. This example demonstrates direct interfacing of CdE NCs with biomolecules.

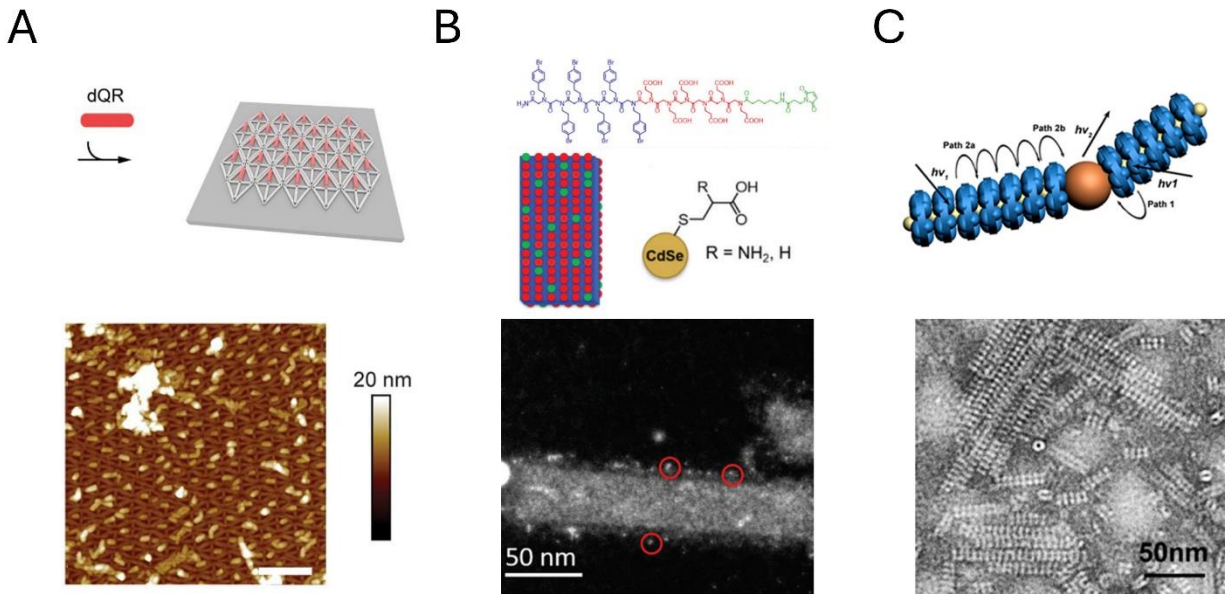

Figure 1.3 (A) (top) schematic of DNA conjugated CdSe/CdS NRs (red) added to assembled rhombic DNA origami. (bottom) 1 µm2 AFM image of CdSe/CdS assembled into DNA rhomboids.23 (B) (top) peptoid sequence used in assembly with hydrophobic portion (blue), hydrophilic portion (red), and maleimide portion (green) along with schematic showing small incorporation of maleimide in peptoid sheet or tube assemblies and cysteine ligated CdSe QDs. (bottom) STEM image of CdSe QDs conjugated with CdSe QDs.24 (C) (top) schematic of CdTe QDs assembled into stable protein one (SP1) nanoring highlighting different potential pathways for energy transfer pathways from the protein assembly to the QD. (bottom) TEM image of self-assembled SP1 and CdTe QDs.25 Adapted from ref 23, 24 and 25.

These three examples highlight the diversity of strategies available for creating CdE-biomolecule systems. Indirect ligand-mediated interfacing offers ligand-biomolecule programmability while direct CdE-biomolecule utilizes biomolecules programmability to interface with bare NC surfaces. Importantly, recent reports have demonstrated that direct

interfacing with chiral ligands can induce chirality in achiral CdE. This emerging optical property has motivated interest in directly interfacing CdE with intrinsically chiral biomolecules.

1.4 Merging Chirality of Proteins and CdE Nanocrystals

1.4.1 *Circular Dichroism Spectroscopy as a Probe for Chirality*

A consequence of sequence-defined chemistry with chiral molecular building blocks is the formation of chiral architectures. Before introducing chirality in proteins and CdE NCs, a brief introduction to circular dichroism (CD) as a probe for chirality is necessary. Historically, chirality is defined by molecules containing non-superimposable molecular arrangements, and CD spectroscopy probes this by differential left and right circularly polarized light.[26,27] Molecules containing a single chiral carbon center typically display a single CD absorbance feature (either positive or negative), whereas chiral chromophores will display a bisignate feature, where electronic transitions are split by both left and right circularly polarized light, also known as the Cotton effect.[28]

For quantum confined chiral CdE NCs, the CD absorbance spectra contain several bisignate features corresponding to the electronic transitions in the NC, making the CD spectra more complex than traditional chromophores transitions.[29] Since chiral biomolecules absorb in the UV while CdS and CdSe NCs absorb in the visible, CD spectroscopy serves as an excellent probe to confirm direct CdE-biomolecule interfacing. Beyond serving as a probe, direct protein-CdE interfacing may also lead to new chiroptical properties not present in either individual component.

1.4.2 *Protein Chirality Across Length Scales*

Since CD spectroscopy is diagnostic of chirality, it is widely used to characterize the hierarchical chirality of proteins. Amino acids and proteins are inherently homochiral, with 21 of the 22 most common amino acids containing a chiral carbon center (Figure 1.4 A). These L-amino acids are the building blocks for higher order chiral primary, secondary, and tertiary protein structures.[30]

In the case of a primary protein sequence (or intrinsically disordered protein), random helical coils exhibit structural dissymmetry that can be observed via circular dichroism (CD) absorbance spectroscopy in the UV.[31] These primary sequences can then fold into more ordered structures like α-helices and β-sheets, often on the 1-10 nm length scale, each of which has a distinct CD absorbance spectrum (**Figure 1.4B**).[32] These secondary structures can then assemble into 5-20 nm tertiary structures that stabilize secondary structures (**Figure 1.4C**).[30] At even larger scales, proteins can form extended chiral assemblies like helical fibers reaching micron length (**Figure 1.4D**).[33]

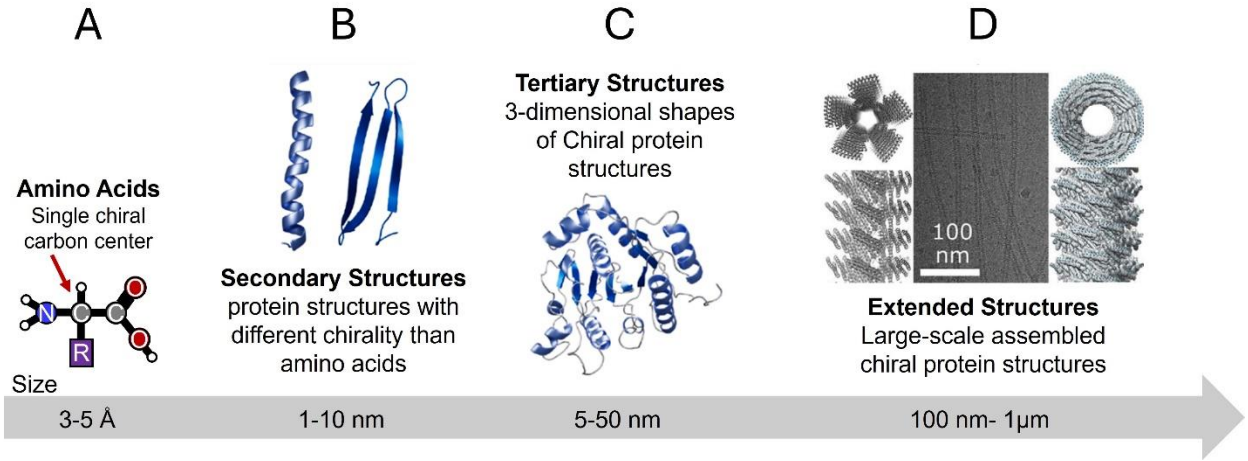

Figure 1.4 (A) General amino acid sequence highlighting the single chiral carbon center (red arrow) on the Å scale. (B) Chiral secondary structure protein sequences of alpha helices (left) and beta sheets (right) typically on the 1-10 nm length scale. (C) General Tertiary protein

structure containing both alpha helices and beta sheets in the same sequence typically on the 5-50 nm length scale.[30] (D) Extended chiral protein structure of designed helical fibers with structures extending up to a micron in length.[33] Adapted from ref 30 and 33.

1.4.3 *CdE Nanocrystal Chirality Across Length Scales*

While proteins exhibit chirality in their hierarchal architectures across length scales, CdE NCs have also displayed chirality across similar length scales. Chirality in inorganic NCs is typically reported as a dissymmetry factor (*g*-factor), which normalized CD intensity by linear absorbance. Often these values are reported as discrete values at the wavelength of the most intense CD absorbance.

Chiral CdE NCs have potential applications in chiral drug detection,[34–37] anti-counterfeit measures,[38] and catalysis.[39] Many reports utilize Cys or Cys derivatives as chiral interfacing ligands interfacing ligands. The first reported chiral CdE NCs were approximately 2 nm CdS QDs produced with penicillamine in an aqueous microwave synthesis by Kelly et al. in 2007, with no reported *g*-factor (**Figure 1.5A**).[40] While this was the first example of a chiral CdE QDs, controlling CdE NC morphology and optical properties in aqueous synthesis has proven to be an outstanding challenge.[41] More commonly, larger, high quality hydrophobic CdE NCs are made chiral and hydrophilic via ligand exchange with Cys and its derivatives (**Figure 1.5B**).[42,43] Generally, more anisotropic structures report higher *g*-factors wth values ranging from from 10^{-5}-10^{-3} [43–46] depending on morphology (**Figure 1.5C**).[47–50] At even larger length scales, chiral assemblies of CdTe QDs can reach *g*-factors approaching 10^{-1} (**Figure 1.5D**).[51,52]

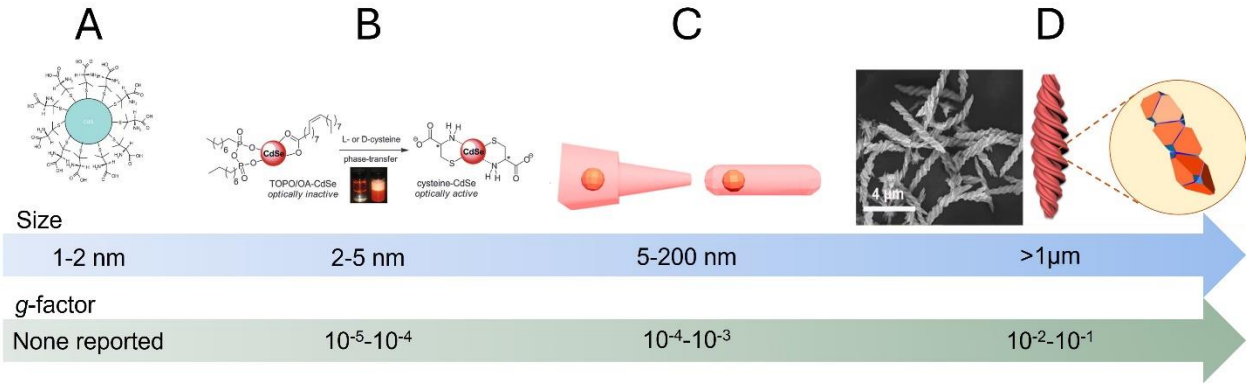

Figure 1.5 (A) L and D-penicillamine capped chiral CdS QDs (1-2 nm in diameter) made by microwave assisted aqueous synthesis with no reported *g*-factor.[40] (B) ligand exchanged hydrophobic CdSe QDs (2-5 nm) into aqueous media using L and D-Cys resulting in chiral QDs with *g*-factors of 10^{-5}-10^{-4}.[42,43] (C) Ligand exchanging L-Cys with more anisotropic CdSe/CdS NCs has resulted in larger *g*-factors of 10^{-4}-10^{-3}.[50] (D) Assembled cysteine-capped CdTe QDs into helices using a 2-solvent system results in g-factors of 10^{-2} to 10^{-1}. Adapted from ref 40, 42, and 50.

1.4.4 *Mechanism of Chirality Transfer to CdE Nanocrystals*

While there are many examples of chiral CdE NCs, mechanistic origins of their chirality are still actively investigated. In general, there are four proposed mechanisms to cause chirality in CdE NCs. The first mechanism proposes chiral ligand addition during the CdE NC nucleation and growth phase bias the CdE core to a specific handedness (**Figure 1.6A**).[53] The next mechanism proposes organized spatial arrangement (i.e. helical pitch) of CdE NCs leads to induced chirality of the system (**Figure 1.6B**).[51]

The third mechanism is used to describe post-synthetic ligand exchange chirality in previously achiral CdE NCs.[43–49] In this mechanism, chiral ligand exchange leads to a distortion of surface atoms in the crystal lattice that can also lead to a chiral arrangement of the ligand shell

around the inorganic core, as shown in CdSe nanoplatelets (**Figure 1.6C**).[54] While surface atom distortion has been experimentally demonstrated in CdSe nanoplatelets, it is unclear if this mechanism applies to larger NCs.

Finally, a fourth mechanism has been frequently employed to explain post-synthetic ligand induced chirality in CdE NCs. This mechanism described an electronic coupling between the highest unoccupied molecular orbitals of the chiral ligand and the hole generated in the electronic excitations of the NC (**Figure 1.6D**).[29] Importantly, this mechanism relies exclusively on theoretical works and has yet to be determined experimentally.

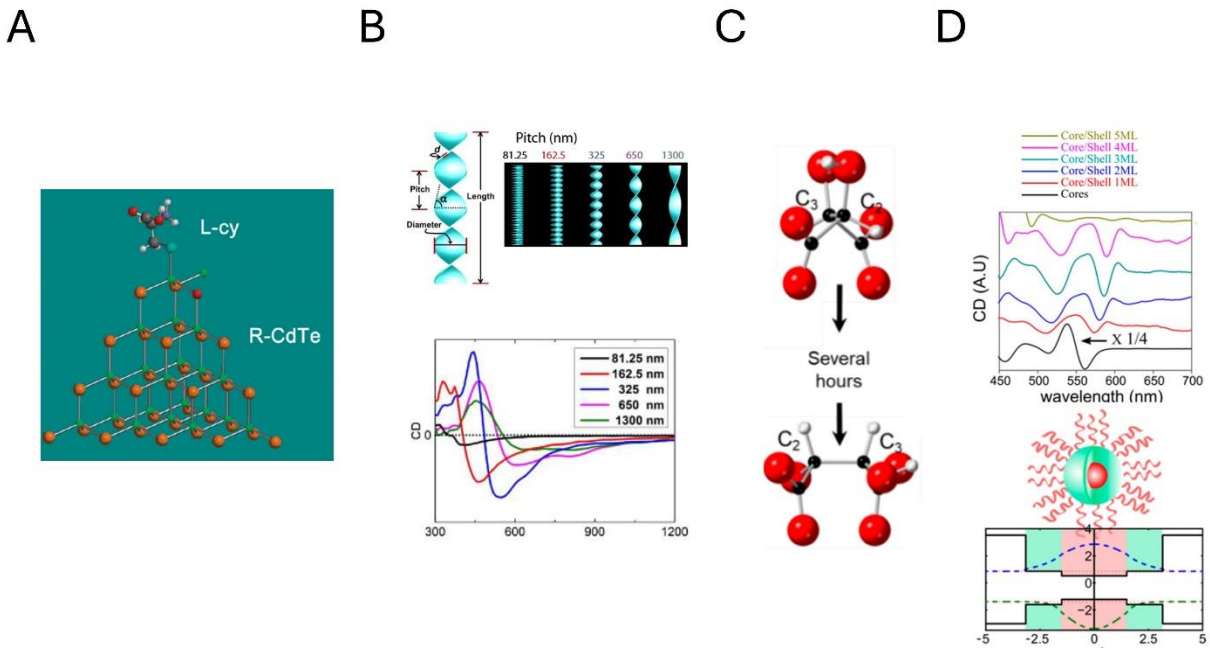

Figure 1.6 (A) Proposed structure matching or R-CdTe cores with L-Cys during the aqueous synthesis of CdTe QDs leading to chiral CdTe QDs.[53] (B) In large assemblies of CdE NCs, simulations demonstrate that the pitch length alters the chiroptical response of the assembly.[51] Post-synthetic ligand exchange induced chirality is proposed to happen by (C) re-arrangement of surface CdE[54] or (D) electronic coupling between the generated hole of CdE and the highest unoccupied molecular orbitals of Cys.[29] Adapted from Ref 53, 51, 54 and 29.

1.4.5 *Bridging Chial Length Scales of Proteins and CdE Nanocrystals*

These mechanistic insights suggest that any protein should induce chirality at the CdE NC interface. Surprisingly, there is only one report of using proteins to synthesize chiral CdE NCs to date. This report by Spangler and coworkers templated CdS QD nucleation and growth using protein side chain interactions.[55] While this is the only report of chiral protein:CdE NC materials, the QD optical properties are relatively poor compared to the highest quality CdE NCs prepared in non-polar, high boiling point solvents.[11]

Although biomolecule:CdE NC chiral assemblies are attractive due to potential for large *g*-factor at extended length scales, interfacial CdE chirality may also arise via direct protein conjugation to pre-synthesized NCs. This interfacial chemistry has been largely unexplored and could help realize biosensing and bioimaging applications of these materials.

1.5 Cys for Interfacing CdS Nanocrystals and Biomolecules

While Cys has been used to interface CdE NCs, it is also an amino acid found in many protein sequences. For these reasons, Cys is an excellent residue to encode within a protein sequence to interact directly with CdE NC interfaces. To access higher g-factors, we aim to synthesize high quality hydrophibic CdS NCs and subsequently perform an aqueous phase exchange. These ligand exchanges typically involve basic aqueous layers containing tetramethylammonium hydroxide and excess Cys.[43–47,49,50]

Through zinc-finger protein domains, it has been widely shown that Cd^{2+} has a high affinity for reduced Cys in proteins.[56–58] Relatedly, CdE NC synthetic methods result in excess surface cadmium that requires passivation for colloidal stability. Additionally, to understand the

binding affinity of thiols, Dempsey and coworkers employed 1H NMR studies to determine that thiols irreversibly replace carboxylate groups on the surface of CdSe QDs.[59]

Through these previous findings, we can conceptualize individual CdE NCs as positively charged cadmium superatoms. When approached in this manner, interfacing Cys-containing proteins with CdE NCs becomes a much simpler coordination chemistry problem. However, directly exchanging hydrophobic NCs with proteins in the aqueous phase is not feasible due to the harsh biphasic ligand exchange methods and large excess of hydrophilic ligand required. Instead, we look to preserve achiral nature of the starting NCs while making them water-soluble to interact with chiral Cys residues in proteins. Building on previous reports by Dempsey and coworkers, we want to use a temporary hydrophilic achiral carboxylic acid that will be irreversibly replaced by a chiral Cys in a protein structure.

1.6 REFERENCES

(1) Shirasaki, Y.; Supran, G. J.; Bawendi, M. G.; Bulović, V. Emergence of Colloidal Quantum-Dot Light-Emitting Technologies. Nat. Photonics 2013, 7 (1), 13–23. https://doi.org/10.1038/nphoton.2012.328.

(2) Konstantatos, G.; Sargent, E. H. Nanostructured Materials for Photon Detection. Nat. Nanotechnol. 2010, 5 (6), 391–400. https://doi.org/10.1038/nnano.2010.78.

(3) Bhandari, S.; Pramanik, S.; Biswas, N. K.; Roy, S.; Pan, U. N. Enhanced Luminescence of a Quantum Dot Complex Following Interaction with Protein for Applications in Cellular Imaging, Sensing, and White-Light Generation. ACS Appl. Nano Mater. 2019, 2 (4), 2358–2366. https://doi.org/10.1021/acsanm.9b00233.

(4) Enright, M. J.; Gilbert-Bass, K.; Sarsito, H.; Cossairt, B. M. Photolytic C–O Bond Cleavage with Quantum Dots. Chem. Mater. 2019, 31 (7), 2677–2682. https://doi.org/10.1021/acs.chemmater.9b00943.

(5) García de Arquer, F. P.; Talapin, D. V.; Klimov, V. I.; Arakawa, Y.; Bayer, M.; Sargent, E. H. Semiconductor Quantum Dots: Technological Progress and Future Challenges. Science 2021, 373 (6555), eaaz8541. https://doi.org/10.1126/science.aaz8541.

(6) Cotta, M. A. Quantum Dots and Their Applications: What Lies Ahead? ACS Appl. Nano Mater. 2020, 3 (6), 4920–4924. https://doi.org/10.1021/acsanm.0c01386.

(7) Charge Carrier Dynamics and Optical Gain in Nanocrystal Quantum Dots: From Fundamental Photophysics to Quantum-Dot Lasing. In Semiconductor and Metal Nanocrystals; CRC Press, 2003.
(8) Yu, W. W.; Qu, L.; Guo, W.; Peng, X. Experimental Determination of the Extinction Coefficient of CdTe, CdSe, and CdS Nanocrystals. Chem. Mater. 2003, 15 (14), 2854–2860. https://doi.org/10.1021/cm034081k.
(9) Yu, W. W.; Peng, X. Formation of High-Quality CdS and Other II–VI Semiconductor Nanocrystals in Noncoordinating Solvents: Tunable Reactivity of Monomers. Angew. Chem. Int. Ed. 2002, 41 (13), 2368–2371. https://doi.org/10.1002/1521-3773(20020703)41:13%253C2368::AID-ANIE2368%253E3.0.CO;2-G.
(10) Liu, L.; Zhuang, Z.; Xie, T.; Wang, Y.-G.; Li, J.; Peng, Q.; Li, Y. Shape Control of CdSe Nanocrystals with Zinc Blende Structure. J. Am. Chem. Soc. 2009, 131 (45), 16423–16429. https://doi.org/10.1021/ja903633d.
(11) Murray, C. B.; Norris, D. J.; Bawendi, M. G. Synthesis and Characterization of Nearly Monodisperse CdE (E = Sulfur, Selenium, Tellurium) Semiconductor Nanocrystallites. J. Am. Chem. Soc. 1993, 115 (19), 8706–8715. https://doi.org/10.1021/ja00072a025.
(12) Manna, L.; Wang; Cingolani, R.; Alivisatos, A. P. First-Principles Modeling of Unpassivated and Surfactant-Passivated Bulk Facets of Wurtzite CdSe: A Model System for Studying the Anisotropic Growth of CdSe Nanocrystals. J. Phys. Chem. B 2005, 109 (13), 6183–6192. https://doi.org/10.1021/jp0445573.
(13) Peng, X.; Wickham, J.; Alivisatos, A. P. Kinetics of II-VI and III-V Colloidal Semiconductor Nanocrystal Growth: "Focusing" of Size Distributions. J. Am. Chem. Soc. 1998, 120 (21), 5343–5344. https://doi.org/10.1021/ja9805425.
(14) Peng, X.; Manna, L.; Yang, W.; Wickham, J.; Scher, E.; Kadavanich, A.; Alivisatos, A. P. Shape Control of CdSe Nanocrystals. Nature 2000, 404 (6773), 59–61. https://doi.org/10.1038/35003535.
(15) Hu, J.; Wang; Li, L.; Yang, W.; Alivisatos, A. P. Semiempirical Pseudopotential Calculation of Electronic States of CdSe Quantum Rods. J. Phys. Chem. B 2002, 106 (10), 2447–2452. https://doi.org/10.1021/jp013204q.
(16) Hu, J.; Li, L.; Yang, W.; Manna, L.; Wang, L.; Alivisatos, A. P. Linearly Polarized Emission from Colloidal Semiconductor Quantum Rods. Science 2001, 292 (5524), 2060–2063. https://doi.org/10.1126/science.1060810.
(17) Boles, M. A.; Ling, D.; Hyeon, T.; Talapin, D. V. The Surface Science of Nanocrystals. Nat. Mater. 2016, 15 (2), 141–153. https://doi.org/10.1038/nmat4526.
(18) Rothemund, P. W. K. Folding DNA to Create Nanoscale Shapes and Patterns. Nature 2006, 440 (7082), 297–302. https://doi.org/10.1038/nature04586.
(19) Hong, F.; Zhang, F.; Liu, Y.; Yan, H. DNA Origami: Scaffolds for Creating Higher Order Structures. Chem. Rev. 2017, 117 (20), 12584–12640. https://doi.org/10.1021/acs.chemrev.6b00825.
(20) Jin, H.; Ding, Y.-H.; Wang, M.; Song, Y.; Liao, Z.; Newcomb, C. J.; Wu, X.; Tang, X.-Q.; Li, Z.; Lin, Y.; Yan, F.; Jian, T.; Mu, P.; Chen, C.-L. Designable and Dynamic Single-Walled Stiff Nanotubes Assembled from Sequence-Defined Peptoids. Nat. Commun. 2018, 9 (1), 270. https://doi.org/10.1038/s41467-017-02059-1.
(21) Zuckermann, R. N.; Kerr, J. M.; Kent, S. B. H.; Moos, W. H. Efficient Method for the Preparation of Peptoids [Oligo(N-Substituted Glycines)] by Submonomer Solid-Phase

Synthesis. J. Am. Chem. Soc. 1992, 114 (26), 10646–10647. https://doi.org/10.1021/ja00052a076.
(22) Zhang, S.; Alberstein, R. G.; De Yoreo, J. J.; Tezcan, F. A. Assembly of a Patchy Protein into Variable 2D Lattices via Tunable Multiscale Interactions. Nat. Commun. 2020, 11 (1), 3770. https://doi.org/10.1038/s41467-020-17562-1.
(23) Chen, C.; Luo, X.; Kaplan, A. E. K.; Bawendi, M. G.; Macfarlane, R. J.; Bathe, M. Ultrafast Dense DNA Functionalization of Quantum Dots and Rods for Scalable 2D Array Fabrication with Nanoscale Precision. Sci. Adv. 2023, 9 (32), eadh8508. https://doi.org/10.1126/sciadv.adh8508.
(24) Monahan, M.; Cai, B.; Jian, T.; Zhang, S.; Zhu, G.; Chen, C.-L.; Yoreo, J. J. D.; Cossairt, B. M. Peptoid-Directed Assembly of CdSe Nanoparticles. Nanoscale 2021, 13 (2), 1273–1282. https://doi.org/10.1039/D0NR07509D.
(25) Miao, L.; Han, J.; Zhang, H.; Zhao, L.; Si, C.; Zhang, X.; Hou, C.; Luo, Q.; Xu, J.; Liu, J. Quantum-Dot-Induced Self-Assembly of Cricoid Protein for Light Harvesting. ACS Nano 2014, 8 (4), 3743–3751. https://doi.org/10.1021/nn500414u.
(26) [4] Circular Dichroism. In Methods in Enzymology; Academic Press, 1995; Vol. 246, pp 34–71. https://doi.org/10.1016/0076-6879(95)46006-3.
(27) Nafie, L. A. Circular Polarization Spectroscopy of Chiral Molecules. J. Mol. Struct. 1995, 347, 83–100. https://doi.org/10.1016/0022-2860(95)08538-7.
(28) Matile, S.; Berova, N.; Nakanishi, K.; Novkova, S.; Philipova, I.; Blagoev, B. Porphyrins: Powerful Chromophores for Structural Studies by Exciton-Coupled Circular Dichroism. J. Am. Chem. Soc. 1995, 117 (26), 7021–7022. https://doi.org/10.1021/ja00131a033.
(29) Ben-Moshe, A.; Teitelboim, A.; Oron, D.; Markovich, G. Probing the Interaction of Quantum Dots with Chiral Capping Molecules Using Circular Dichroism Spectroscopy. Nano Lett. 2016, 16 (12), 7467–7473. https://doi.org/10.1021/acs.nanolett.6b03143.
(30) Zhu, J.; Avakyan, N.; Kakkis, A.; Hoffnagle, A. M.; Han, K.; Li, Y.; Zhang, Z.; Choi, T. S.; Na, Y.; Yu, C.-J.; Tezcan, F. A. Protein Assembly by Design. Chem. Rev. 2021, 121 (22), 13701–13796. https://doi.org/10.1021/acs.chemrev.1c00308.
(31) Miles, A. J.; Drew, E. D.; Wallace, B. A. DichroIDP: A Method for Analyses of Intrinsically Disordered Proteins Using Circular Dichroism Spectroscopy. Commun. Biol. 2023, 6 (1), 823. https://doi.org/10.1038/s42003-023-05178-2.
(32) Chen, Y.-H.; Yang, J. T.; Chau, K. H. Determination of the Helix and β Form of Proteins in Aqueous Solution by Circular Dichroism. Biochemistry 1974, 13 (16), 3350–3359. https://doi.org/10.1021/bi00713a027.
(33) Shen, H.; Fallas, J. A.; Lynch, E.; Sheffler, W.; Parry, B.; Jannetty, N.; Decarreau, J.; Wagenbach, M.; Vicente, J. J.; Chen, J.; Wang, L.; Dowling, Q.; Oberdorfer, G.; Stewart, L.; Wordeman, L.; De Yoreo, J.; Jacobs-Wagner, C.; Kollman, J.; Baker, D. De Novo Design of Self-Assembling Helical Protein Filaments. Science 2018, 362 (6415), 705–709. https://doi.org/10.1126/science.aau3775.
(34) Zhang, L.; Xu, X.; Chen, Y.; Zhang, S.; Lin, Z.; Li, D.; Li, J. Portable Multimodal Sensor for Chiral Drug Recognition: β-Cyclodextrin-Quantum Dot Synergy on Screen-Printed Electrodes. Microchem. J. 2025, 219, 115867. https://doi.org/10.1016/j.microc.2025.115867.
(35) Carrillo-Carrión, C.; Cárdenas, S.; Simonet, B. M.; Valcárcel, M. Selective Quantification of Carnitine Enantiomers Using Chiral Cysteine-Capped CdSe(ZnS)

Quantum Dots. Anal. Chem. 2009, 81 (12), 4730–4733. https://doi.org/10.1021/ac900034h.
(36) Zhu, F.; Wang, J.; Xie, S.; Zhu, Y.; Wang, L.; Xu, J.; Liao, S.; Ren, J.; Liu, Q.; Yang, H.; Chen, X. L-Pyroglutamic Acid-Modified CdSe/ZnS Quantum Dots: A New Fluorescence-Responsive Chiral Sensing Platform for Stereospecific Molecular Recognition. Anal. Chem. 2020, 92 (17), 12040–12048. https://doi.org/10.1021/acs.analchem.0c02668.
(37) Delgado-Pérez, T.; Bouchet, L. M.; de la Guardia, M.; Galian, R. E.; Pérez-Prieto, J. Sensing Chiral Drugs by Using CdSe/ZnS Nanoparticles Capped with N-Acetyl-L-Cysteine Methyl Ester. Chem. – Eur. J. 2013, 19 (33), 11068–11076. https://doi.org/10.1002/chem.201300875.
(38) Chen, L.; Lai, C.; Marchewka, R.; Berry, R. M.; Tam, K. C. Use of CdS Quantum Dot-Functionalized Cellulose Nanocrystal Films for Anti-Counterfeiting Applications. Nanoscale 2016, 8 (27), 13288–13296. https://doi.org/10.1039/C6NR03039D.
(39) Sun, M.; Xu, L.; Qu, A.; Zhao, P.; Hao, T.; Ma, W.; Hao, C.; Wen, X.; Colombari, F. M.; de Moura, A. F.; Kotov, N. A.; Xu, C.; Kuang, H. Site-Selective Photoinduced Cleavage and Profiling of DNA by Chiral Semiconductor Nanoparticles. Nat. Chem. 2018, 10 (8), 821–830. https://doi.org/10.1038/s41557-018-0083-y.
(40) Moloney, M. P.; Gun'ko, Y. K.; Kelly, J. M. Chiral Highly Luminescent CdS Quantum Dots. Chem. Commun. 2007, No. 38, 3900–3902. https://doi.org/10.1039/B704636G.
(41) Moloney, M. P.; Govan, J.; Loudon, A.; Mukhina, M.; Gun'ko, Y. K. Preparation of Chiral Quantum Dots. Nat. Protoc. 2015, 10 (4), 558–573. https://doi.org/10.1038/nprot.2015.028.
(42) Tohgha, U.; Varga, K.; Balaz, M. Achiral CdSe Quantum Dots Exhibit Optical Activity in the Visible Region upon Post-Synthetic Ligand Exchange with D- or L-Cysteine. Chem. Commun. 2013, 49 (18), 1844–1846. https://doi.org/10.1039/C3CC37987F.
(43) Tohgha, U.; Deol, K. K.; Porter, A. G.; Bartko, S. G.; Choi, J. K.; Leonard, B. M.; Varga, K.; Kubelka, J.; Muller, G.; Balaz, M. Ligand Induced Circular Dichroism and Circularly Polarized Luminescence in CdSe Quantum Dots. ACS Nano 2013, 7 (12), 11094–11102. https://doi.org/10.1021/nn404832f.
(44) Kuznetsova, V. A.; Mates-Torres, E.; Prochukhan, N.; Marcastel, M.; Purcell-Milton, F.; O'Brien, J.; Visheratina, A. K.; Martinez-Carmona, M.; Gromova, Y.; Garcia-Melchor, M.; Gun'ko, Y. K. Effect of Chiral Ligand Concentration and Binding Mode on Chiroptical Activity of CdSe/CdS Quantum Dots. ACS Nano 2019, 13 (11), 13560–13572. https://doi.org/10.1021/acsnano.9b07513.
(45) Purcell-Milton, F.; Visheratina, A. K.; Kuznetsova, V. A.; Ryan, A.; Orlova, A. O.; Gun'ko, Y. K. Impact of Shell Thickness on Photoluminescence and Optical Activity in Chiral CdSe/CdS Core/Shell Quantum Dots. ACS Nano 2017, 11 (9), 9207–9214. https://doi.org/10.1021/acsnano.7b04199.
(46) Choi, J. K.; Haynie, B. E.; Tohgha, U.; Pap, L.; Elliott, K. W.; Leonard, B. M.; Dzyuba, S. V.; Varga, K.; Kubelka, J.; Balaz, M. Chirality Inversion of CdSe and CdS Quantum Dots without Changing the Stereochemistry of the Capping Ligand. ACS Nano 2016, 10 (3), 3809–3815. https://doi.org/10.1021/acsnano.6b00567.
(47) Gao, X.; Zhang, X.; Deng, K.; Han, B.; Zhao, L.; Wu, M.; Shi, L.; Lv, J.; Tang, Z. Excitonic Circular Dichroism of Chiral Quantum Rods. J. Am. Chem. Soc. 2017, 139 (25), 8734–8739. https://doi.org/10.1021/jacs.7b04224.

(48) Liu, M.; Li, G.; Wei, S.; Liu, H.; Yang, G. Ligand-Induced Chiroptical Properties in Nanocrystals with Different Core–Shell Band Structures. ACS Appl. Nano Mater. 2025, 8 (4), 1843–1851. https://doi.org/10.1021/acsanm.4c06205.
(49) Cheng, J.; Hao, J.; Liu, H.; Li, J.; Li, J.; Zhu, X.; Lin, X.; Wang, K.; He, T. Optically Active CdSe-Dot/CdS-Rod Nanocrystals with Induced Chirality and Circularly Polarized Luminescence. ACS Nano 2018, 12 (6), 5341–5350. https://doi.org/10.1021/acsnano.8b00112.
(50) Hao, J.; Li, Y.; Miao, J.; Liu, R.; Li, J.; Liu, H.; Wang, Q.; Liu, H.; Delville, M.-H.; He, T.; Wang, K.; Zhu, X.; Cheng, J. Ligand-Induced Chirality in Asymmetric CdSe/CdS Nanostructures: A Close Look at Chiral Tadpoles. ACS Nano 2020, 14 (8), 10346–10358. https://doi.org/10.1021/acsnano.0c03909.
(51) Feng, W.; Kim, J.-Y.; Wang, X.; Calcaterra, H. A.; Qu, Z.; Meshi, L.; Kotov, N. A. Assembly of Mesoscale Helices with Near-Unity Enantiomeric Excess and Light-Matter Interactions for Chiral Semiconductors. Sci. Adv. 2017, 3 (3), e1601159. https://doi.org/10.1126/sciadv.1601159.
(52) Zhou, Y.; Marson, R. L.; van Anders, G.; Zhu, J.; Ma, G.; Ercius, P.; Sun, K.; Yeom, B.; Glotzer, S. C.; Kotov, N. A. Biomimetic Hierarchical Assembly of Helical Supraparticles from Chiral Nanoparticles. ACS Nano 2016, 10 (3), 3248–3256. https://doi.org/10.1021/acsnano.5b05983.
(53) Zhou, Y.; Yang, M.; Sun, K.; Tang, Z.; Kotov, N. A. Similar Topological Origin of Chiral Centers in Organic and Nanoscale Inorganic Structures: Effect of Stabilizer Chirality on Optical Isomerism and Growth of CdTe Nanocrystals. J. Am. Chem. Soc. 2010, 132 (17), 6006–6013. https://doi.org/10.1021/ja906894r.
(54) Lehouelleur, H.; Po, H.; Makké, L.; Fu, N.; Curti, L.; Dabard, C.; Roux-Byl, C.; Baptiste, B.; Van Zee, N. J.; Pons, T.; Lhuillier, E.; Li, J.; Ithurria, S. Self-Assembly of Chiral Ligands on 2D Semiconductor Nanoplatelets for High Circular Dichroism. J. Am. Chem. Soc. 2024, 146 (45), 30871–30882. https://doi.org/10.1021/jacs.4c08981.
(55) Spangler, L. C.; Yao, Y.; Cheng, G.; Yao, N.; Chari, S. L.; Scholes, G. D.; Hecht, M. H. A de Novo Protein Catalyzes the Synthesis of Semiconductor Quantum Dots. Proc. Natl. Acad. Sci. 2022, 119 (51), e2204050119. https://doi.org/10.1073/pnas.2204050119.
(56) Brandis, J. E. P.; Zalesak, S. M.; Kane, M. A.; Michel, S. L. J. Cadmium Exchange with Zinc in the Non-Classical Zinc Finger Protein Tristetraprolin. Inorg. Chem. 2021, 60 (11), 7697–7707. https://doi.org/10.1021/acs.inorgchem.0c03808.
(57) Krepkiy, D.; Försterling, F. H.; Petering, D. H. Interaction of Cd2+ with Zn Finger 3 of Transcription Factor IIIA: Structures and Binding to Cognate DNA. Chem. Res. Toxicol. 2004, 17 (7), 863–870. https://doi.org/10.1021/tx030057+.
(58) Malgieri, G.; Palmieri, M.; Esposito, S.; Maione, V.; Russo, L.; Baglivo, I.; Paola, I. de; Milardi, D.; Diana, D.; Zaccaro, L.; Pedone, P. V.; Fattorusso, R.; Isernia, C. Zinc to Cadmium Replacement in the Prokaryotic Zinc-Finger Domain. Metallomics 2013, 6 (1), 96–104. https://doi.org/10.1039/C3MT00208J.
(59) Knauf, R. R.; Lennox, J. C.; Dempsey, J. L. Quantifying Ligand Exchange Reactions at CdSe Nanocrystal Surfaces. Chem. Mater. 2016, 28 (13), 4762–4770. https://doi.org/10.1021/acs.chemmater.6b01827.

Chapter 2. INDUCED CHIRALITY IN QDS USING THERMORESPONSIVE ELASTIN-LIKE POLYPEPTIDES

2.1 INTRODUCTION

Circular dichroism (CD) has emerged as a powerful spectroscopic probe for studying chiral small molecules as surface ligands on quantum dots (QDs). In 2013, Tohgha et al. demonstrated that absorbance and luminescence chirality could be induced on achiral and hydrophobic CdSe QDs by post-synthetic ligand exchange with L and D-cysteine.[1,2] While the origin and mechanism of this induced chirality are still not wholly understood, two theories have been introduced to explain this phenomenon. The first is a physical distortion of the QD lattice through chiral ligand coordination to surface metal ions.[3–5] The second is the hybridization of the QD hole wavefunction and molecular orbitals of the ligands, which splits the electron excitation into two sublevels, as evident in the CD.[2,6,7]

While there are examples using CD to confirm chiral ligand exchanges on achiral QDs, this technique has seldom been used to confirm the conjugation of complex ligands such as polypeptides and proteins on QDs. Previous reports have demonstrated ligand exchange of CdSe and CdS QDs with peptides[8], poly-N-substituted glycines[9,10], and DNA[11] in aqueous environments but relied on UV-Vis absorbance, photoluminescence, and nuclear magnetic resonance spectroscopies to confirm conjugation. QDs are used increasingly in applications for biological systems, including bioimaging,[12] disease detection,[13] drug delivery,[14] and site-

selective DNA scission,[15] highlighting the importance of understanding the interaction of the QD surface with its biological environment.

Drawing inspiration from tropoelastin, water-soluble elastin-like polypeptides (ELPs) are genetically engineered, low-complexity proteins consisting of a repeated sequence of five amino acids (valine, proline, glycine, X, glycine) (VPGXG), where X is any amino acid except proline.[16,17] The identity of this guest residue and the number of repeated pentamers both impact the phase transition temperature (T_t) [18] above which ELPs reversibly collapse into phase-segregated liquid droplets known as coacervates. Adding to their thermoresponsiveness, ELPs can be engineered with a variety of terminal amino acids,[19] making them attractive for drug delivery,[20] metal removal,[21] protein purification,[22] and tissue engineering.[23]

Leveraging ELP's stimuli-responsiveness and sequence-defined chemistry to coordinate inorganic nanoparticles exhibiting unique electronic and spectroscopic characteristics enables the rational design of dynamic hybrid nanomaterials.[24] While there are examples of QDs in biologically relevant environments,[25] there are few examples of cadmium chalcogenide QDs with ELPs. In 2010, Fahmi et al. demonstrated a colloidal bottom-up synthesis of CdSe with ELPs, which made QD-decorated nanofibrils that could permeate cell membranes and demonstrated no cytotoxicity.[26] In 2011, Biswas et al. described the post-synthetic conjugation of a protein containing an ELP domain to QDs that were used to image cellular processes.[27] However, neither study reported on the surface interaction of the ELP with the QD or on the thermoresponsiveness of the resulting ELP-QD conjugates.

Recently, an ELP with the sequence $(VPGVG)_{96}C$ (referred to as V96-Cys) was shown to decorate gold nanoparticle surfaces and form particle-dense coacervates at elevated temperatures, which led to a plasmonic shift of the gold nanoparticles.[28] Due to the low

complexity, lack of internal amino acid binding groups, and C-terminal cysteine of V96-Cys, this polypeptide also provides a platform, for the first time, for ligand exchange onto achiral CdS QDs. Additionally, by engineering a second ELP sequence with the same binding group and a shorter amino acid sequence $(VPGVG)_{54}C$ (referred to as V54-Cys), we can gain a better understanding of how the ligand length in the hybrid systems impacts their thermoresponsiveness. Finally, because both sequences contain one amino-acid binding residue on the surface, we can extend the induced chirality in CdS to polypeptides for the first time.

Here, we describe a simple two-step method for the synthesis and characterization of V96-Cys:CdS and V54-Cys:CdS QD conjugates at μM concentration and neutral pH conditions in an aqueous system starting from traditional hydrophobic CdS QDs. We use CD to probe the surface interaction of the C-terminal cysteine of the ELP with CdS QDs and examine pH influence on their CD spectra. We then examine the dynamic thermoresponsive coacervation of hybrid ELP:QD conjugates using CD, dynamic light scattering (DLS), small angle x-ray scattering (SAXS), and electron microscopy. To the best of our knowledge, this is the first example of post-synthetically inducing chirality in QDs using polypeptides. Additionally, for the first time, we demonstrate the thermoresponsiveness of ELP:CdS as the resulting hybrids show dynamic and cyclable coacervation where both the polypeptide and QD undergo a spatial rearrangement in solution with structure dictated by the sequence lengths of the ELP.

2.2 Results and Discussion

2.2.1 *Glycine:CdS QD Ligand Exchange*

Typical CdS QD synthesis schemes use long-chain fatty acid ligands and have been optimized to control the size, morphology, and optical properties of the nanocrystals.[29–31]

Therefore, post-synthetic ligand exchange is generally required to produce high-quality water-soluble QDs. These ligand exchanges commonly use basic conditions (pH > 11) and alkyl ammonium cations.[1,2,6,32–36] Base is necessary to deprotonate the desired binding groups on the aqueous ligand, while alkyl ammonium is believed to play a key role in reducing the hydrophilicity of the anionic aqueous ligand to allow for the exchange.[36]

Unfortunately, using alkyl ammonium hydroxides is detrimental to exchanging hydrophobic QD ligands directly with proteins, as basic conditions can disrupt the hydrogen bonding network, and alkyl ammonium cations are potent protein precipitating agents in the Hoffmeister series.[37,38] To circumvent these issues, exchange methods have been designed to replace hydrophobic ligands with short-chain linkers, which are then covalently attached to polypeptides or proteins containing polydentate binding groups.[39–42]

In this study, we avoided ELP precipitation by solubilizing native oleate-capped CdS QDs (oleate:CdS) in an aqueous solution of glycine and tetramethylammonium hydroxide (TMAOH) using a method adapted from Tohgha et al.[1,2] (see **2.2.4** experimental). Glycine was chosen as the intermediate ligand because it is a simple achiral amino acid. After the glycine ligand exchange, transmission electron microscopy (TEM) sizing analysis shows slight etching of the QDs from 4.8 nm to 4.1 nm in diameter (**Figure 2.1**), which has been previously observed in aqueous ligand exchanges.[9,10,35] This size decrease is also observed in the UV-Vis absorbance and photoluminescence spectra of the glycine-capped CdS QDs (glycine:CdS) (**Figure 2.2A, B**). Importantly, there is no CD response in the visible region of the spectrum corresponding to the QD absorbance because of the achiral QDs and achiral glycine.

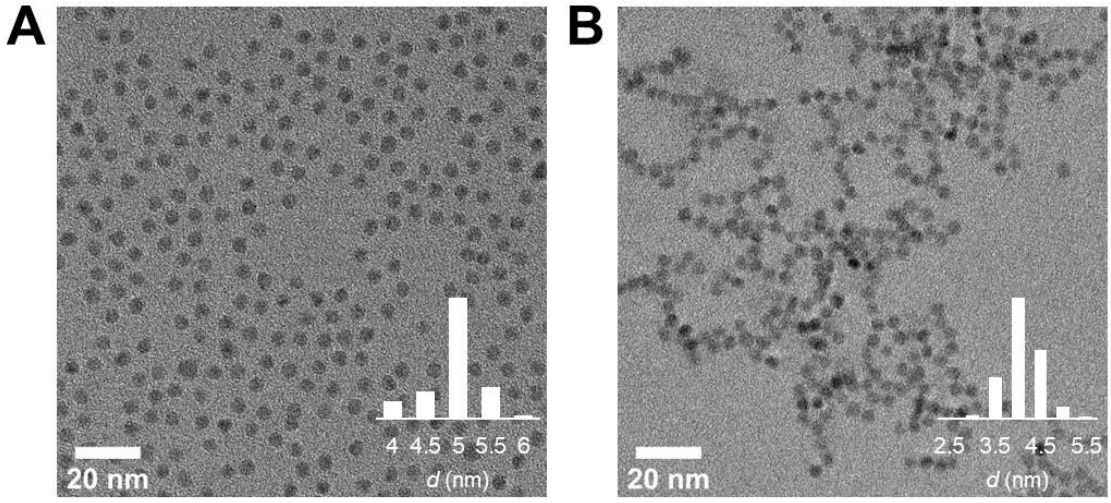

Figure 2.1 (A) TEM image of oleate:CdS with an average diameter of 4.8 ± 0.4 nm. (B) TEM image of glycine:CdS at pH 7 with an average diameter of 4.1 ± 0.4 nm.

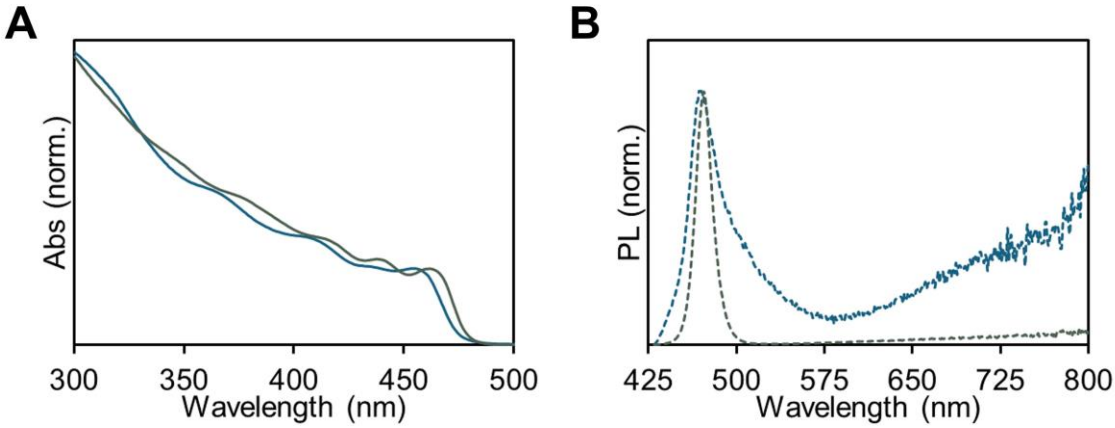

Figure 2.2 (A) Normalized UV-vis of glycine:CdS QDs (blue) in water and oleate:CdS QDs (gray) in toluene. (B) Normalized PL spectra of glycine:CdS QDs (blue) in water and oleate:CdS QDs (gray) in toluene. Excitation at 412 nm.

2.2.2 *ELP Ligand Exchange*

To exchange the achiral glycine ligands with ELPs terminated by a chiral Cys residue, glycine:CdS was incubated with 200 μM of V96-Cys or V54-Cys at 4 °C for 24 hours with

TMAOH and the reducing agent tris(2-carboxyethyl)phosphine hydrochloride (TCEP·HCl) (see **2.4.5** experimental). The incubated QDs show a CD response in the visible range in as little as 1 hour, but the intensity and lineshape do not significantly change from 3 hours to 24 hours, signifying ligand exchange has gone to completion within 3 hours (**Figure 2.3A, B**). The TMAOH and TCEP·HCl are removed through dialysis, and the purified ELP:CdS aqueous solutions exhibit a strong CD signal (**Figure 2.4A-2,3**). The chiral response in the visible region corresponds to the visible QD absorbance (**Figure 2.4B**) and indicates interactions of the chiral ELP with the surface of the QD. As mentioned before, the starting glycine:CdS shows no CD signal (**Figure 2.4A-1**), and the molecular chirality of the ELP itself appears in the ultraviolet region of the CD spectrum (**Figure 2.5A, B**). Therefore, through CD, we can conclude that ELP is present on the surface of the QD. Additionally, the QDs maintain their absorption features and band edge emission with increased trap-state emission after exchanging glycine:CdS samples with V96-Cys, V54-Cys, and NAC (**Figure 2.6**).

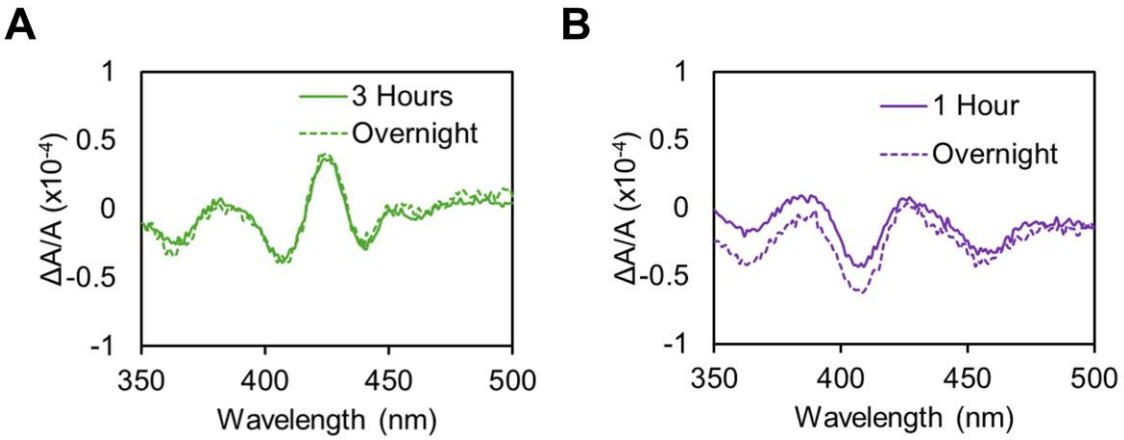

Figure 2.3 (A) Normalized CD spectra of incubating V96-Cys:CdS 1 hour to 24 hours at pH 11 and 4 °C. (B) Normalized CD spectra of Incubating V54-Cys:CdS 3 hours to 24 hours at pH 11 and 4 °C. Spectra were normalized by absorbance at lowest energy electronic transition (458 nm).

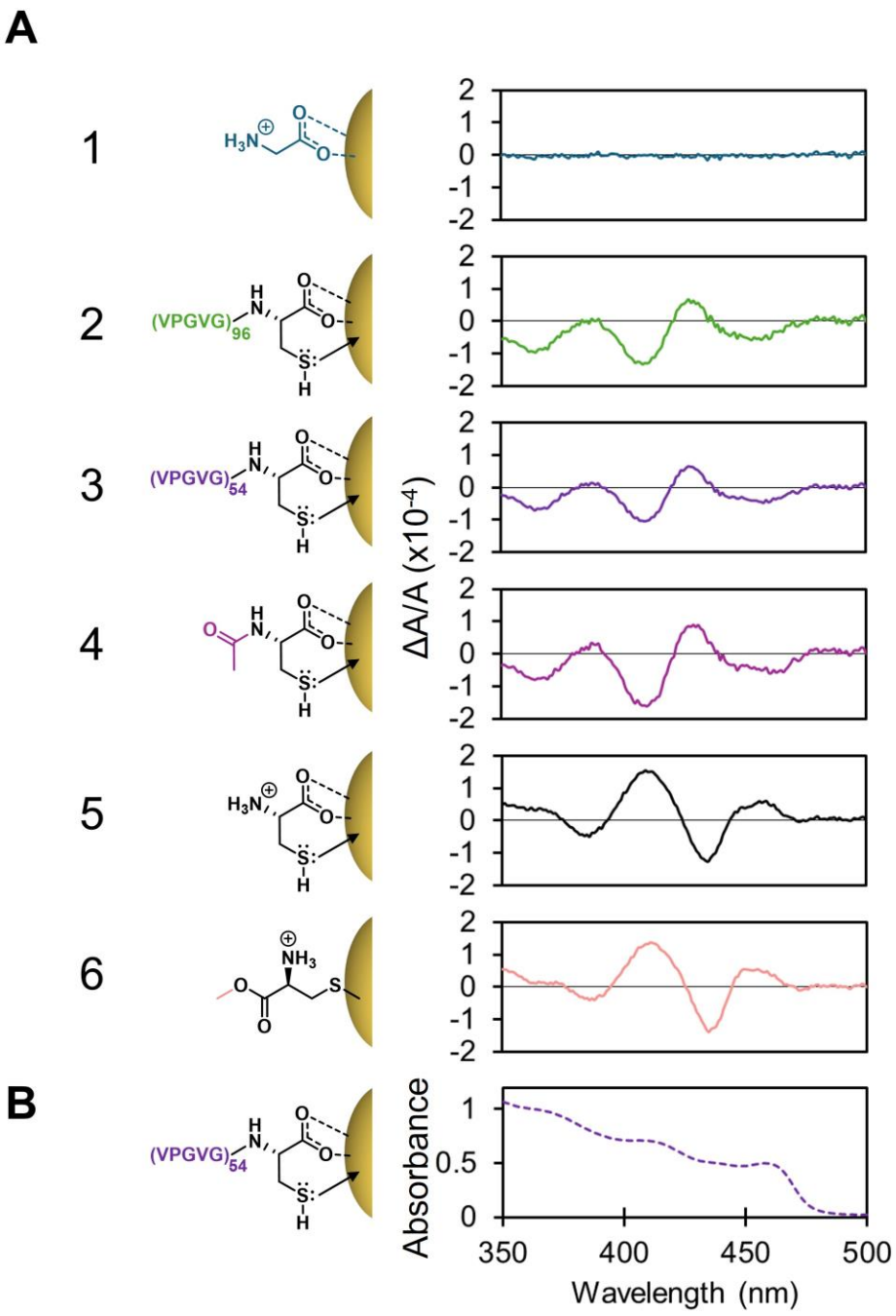

Figure 2.4 (A) Normalized CD spectra at pH 7 of: glycine:CdS (blue, 1), V96-Cys:CdS (green, 2), V54-Cys:CdS (plum, 3), NAC:CdS (magenta, 4), L-Cys:CdS (black, 5), and L-Cys-Me:CdS (orange, 6). (B) UV-Vis absorbance spectrum of V54-Cys:CdS (plum). Binding modes were

assigned based on pKa values. All CD spectra were normalized by absorbance at the lowest energy electronic transition.

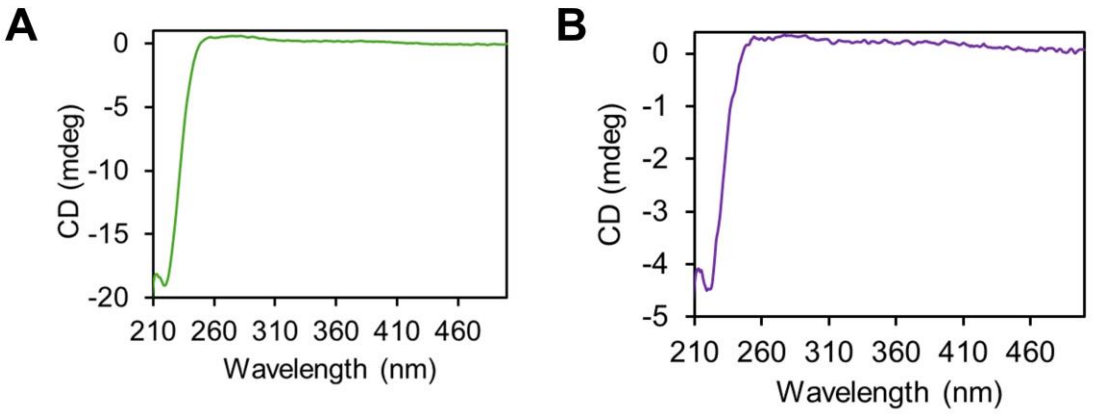

Figure 2.5 (A) CD spectrum of 1 μM V96-Cys in water at 20 °C. (B) CD spectrum of 1 μM V54-Cys in water at 20 °C.

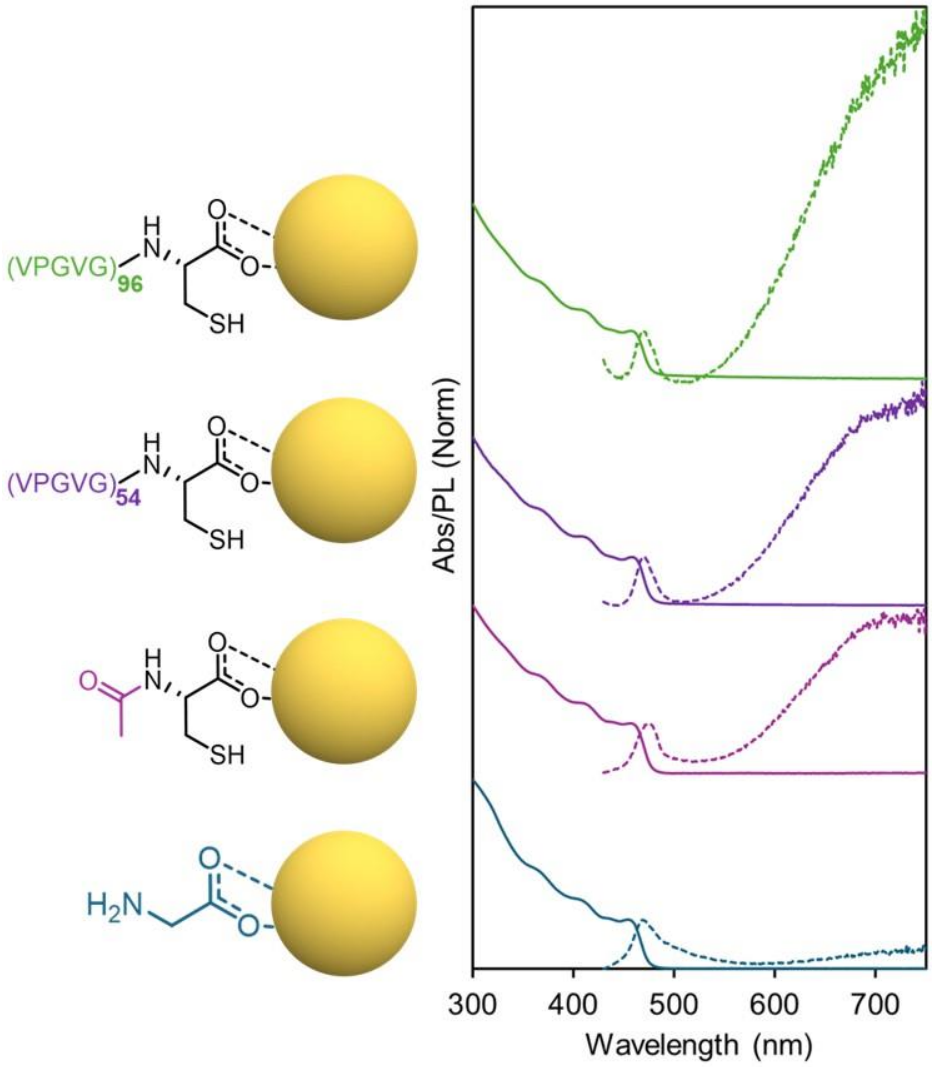

Figure 2.6 Normalized UV-vis and PL spectra of V96-Cys:CdS (green), V54-Cys:CdS (purple), NAC:CdS (plum), and glycine:CdS (blue). All spectra were taken at pH 7 in water at 20 °C.

While UV-Vis and photoluminescence spectroscopies can signify successful exchange of QDs into the aqueous layer of a biphasic solution, they do not offer structural information about the ligands exchanged onto the QD surface. Beyond signifying successful chiral ligand exchange, CD can provide important information about the surface interaction of complex polypeptides with the QDs. The sequence of the ELP was designed with a C-terminal cysteine

residue to bind to the QD. To investigate the binding of the ELP to the QD, three molecular analogs exemplifying possible cysteine coordination motifs were exchanged onto the surface of glycine:CdS: n-acetyl-L-cysteine (NAC), L-cysteine (L-Cys), and L-cysteine methyl ester (L-Cys-Me). NAC (**Figure 2.4A-4**) was used to model an ELP bound to the QD through a C-terminal cysteine, L-Cys (**Figure 2.4A-5**) was used to model free L-Cys bound to the QD, and L-Cys-Me (**Figure 2.4A-6**) was used to model an ELP bound through an N-terminal cysteine residue. Importantly, all three analog:CdS samples were prepared using an analogous procedure to the ELP samples (see **2.4.6-8** experimental).

The normalized CD spectra of V96-Cys:CdS and V54-Cys:CdS closely resemble the spectra of NAC:CdS but have inverted chirality relative to L-Cys:CdS and L-Cys-Me:CdS samples (**Figure 2.4A**). The CD lineshape is identical for the ELP-Cys:CdS and NAC:CdS systems, signifying the same surface interaction for NAC and the C-terminal cysteine on the ELP. This is expected because the amine group of the ELP C-terminal cysteine is participating in an amide bond and is less available to interact with the QD, so NAC is a more appropriate molecular analog than L-Cys and L-Cys-Me. The CD sign inversion for ELP:CdS compared to L-Cys-Me and L-Cys:CdS is expected based on previous work by Choi et al., who demonstrated that NAC:CdS and L-Cys:CdS have inverted chirality, while L-Cys and L-Cys-Me have the same CD lineshape.[32] While the cause of this inversion is not fully understood, Choi and coworkers used simulations to propose that the carbonyl on the acetyl group acts as an L-type ligand on the surface of CdSe, which causes the CD inversion of NAC compared to L-Cys and L-Cys-Me.[32] Previous findings and the results reported here suggest that the chiroptical response of QDs could selectively report on N-terminal cysteine coordination in a protein containing

multiple cysteines. This is because only N-terminal cysteine contains an amine on the nearest chiral carbon that is not an amide (**Figure 2.7**).

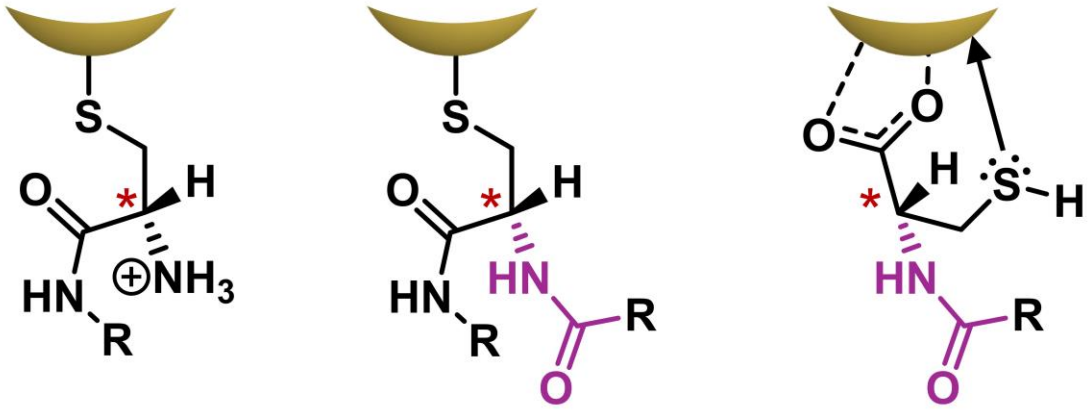

Figure 2.7 Hypothetical binding modes of a protein containing cysteine at the N-terminus, internal, and C-terminus positions at pH 7.

The precise assignment of ligand binding modes by CD is challenging. This is highlighted by the lack of observable change in lineshape between L-Cys:CdS and L-Cys-Me:CdS at pH 7 (**Figure 2.4A-5** and **2.4A-6**). L-Cys-Me does not have a carboxylate group available to bind to the QD, unlike L-Cys, but contains a thiol with a pKa value of 6.5.[43] At pH 7, we presume L-Cys-Me to be predominately a thiolate species, whereas the L-Cys thiol has a pKa value of 8.7[43] and is presumed to remain predominately in the thiol form. It should be noted that the amines of both L-Cys and L-Cys-Me are likely in a dynamic L-type ligand binding equilibrium adding an anchoring point on the QD surface based on previous works.[44,45] While NMR and infrared spectroscopies were useful in elucidating binding modes of L-Cys in these studies, the concentration of L-Cys (>1 mM) is almost an order of magnitude or greater than the

concentration of ELP in our samples, which is limited due to solubility of the poly-peptides. Additionally, the NMR in these studies were performed at pH values greater than 11 which makes direct comparisons to our systems at pH 7 challenging. The lack of CD lineshape differences between L-Cys:CdS and L-Cys-Me:CdS demonstrate the shortcomings of CD when probing thiolate vs. carboxylate binding modes of chiral ligands with primary amines on their α-carbons.

To support the carboxylate binding assignment of V96-Cys:CdS and V54-Cys:CdS at pH 7, as shown in **Figure 2.4**, we investigated bidentate carboxylate and thiolate vs. monodentate carboxylate X-type binding modes using CD. To do this, we examined the lineshapes of L-cystine (L-Cys-Cys):CdS vs. L-Cys:CdS at pH 11 to induce deprotonation of the L-cysteine thiol (pKa of 8.7).[43] L-Cys-Cys, the disulfide dimer of L-cysteine, contains two carboxyl groups but lacks the thiol group of L-cysteine. Exchanging L-Cys-Cys onto glycine:CdS proved unsuccessful, as judged by the absence of changes in the CD spectra after 24 hours of incubation. However, exchanging oleate:CdS with L-Cys-Cys using a procedure adapted from Tohgha et al.[1,2] (see **2.4.9** experimental) produces chiral samples with slightly red-shifted absorbance spectra compared to L-Cys exchanged onto glycine (**Figure 2.8A,B**) (462 nm for L-Cys-Cys:CdS vs. 455 nm for L-Cys:CdS, a difference that we attribute to the distinct ligand exchange methods used in the preparation of the two samples). After purification, pH adjustment, and correcting for the wavelength of the lowest energy electronic transition, the peak locations and sign of the CD lineshape in the L-Cys-Cys:CdS spectrum match L-Cys:CdS at pH 11 (**Figure 2.8C**), indicating a lack of CD lineshape dependence on thiolate binding modes. These findings are also consistent with recent computational work by Han et al.,[7] which predict no changes in the lineshape of the CD spectra between a carboxylate-only binding mode and a thiolate-

carboxyl binding mode of L-Cys-Cys. Therefore, the primary carboxylate binding modes of V96-Cys and V54-Cys at pH 7 are rationalized in our study using pKa values of the thiol (9.4) and carboxyl (3.1) groups of NAC, respectively.[46] Notably, carboxylate binding has been proposed for Cd^{2+} in NAC:Cd complexes in aqueous solutions at pH 7.5, while at pH 11, all Cd^{2+} were bound to thiolates.[47]

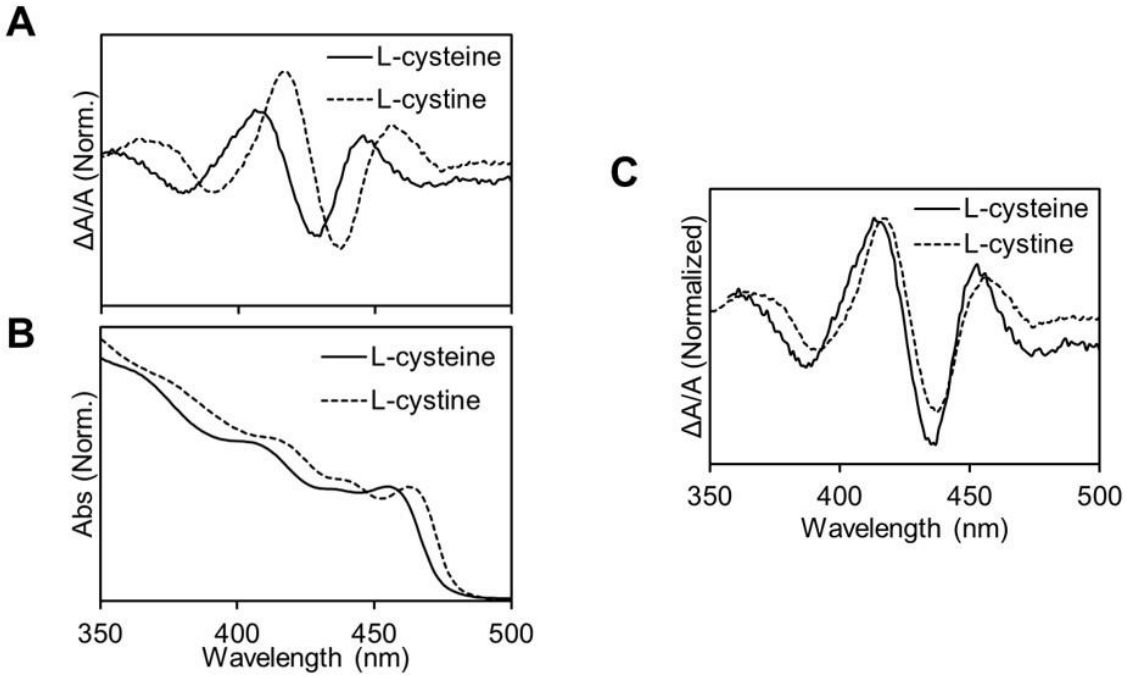

Figure 2.8 (A) Normalized CD spectra of L-cysteine and L-cystine at pH 11. Normalized by absorbance at lowest energy electronic transition. (B) Normalized UV-vis spectra of L-cysteine and L-cystine at pH 11. (C) Normalized CD spectra of L-cysteine and L-cystine at pH 11 after correcting for the wavelength differences in lowest energy electronic transition.

In our study, we found ligands containing thiolate groups exchange readily onto glycine:CdS at pH 11, which can be rationalized by the computations of Han and coworkers, who calculated a 0.11 eV adsorption energy difference favoring thiolate and carboxyl adsorption to CdSe over carboxylate-only adsorption.[7] These previous studies and our observation that L-Cys-Cys does not exchange with glycine while L-Cys does at pH 11 demonstrate that ligand

exchange from glycine becomes more favorable with ligands containing thiolate groups. We attribute this behavior to the thermodynamic favorability of thiolate-cadmium bonds versus carboxylate-cadmium bonds. For these reasons, we hypothesize that the C-terminal cysteines of V96-Cys and V54-Cys provide thiolate groups at pH 11that drive exchange with glycine on the surface of glycine:CdS.

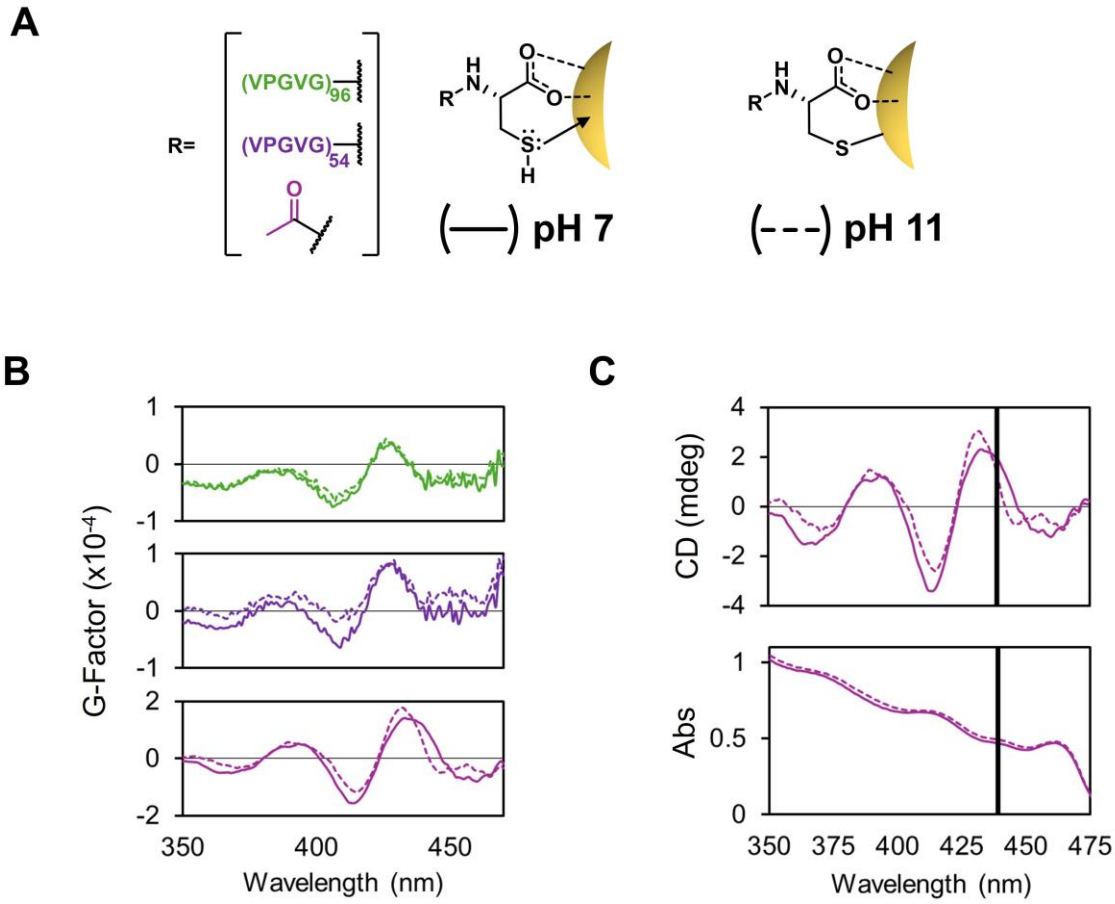

Figure 2.9 (A) Hypothesized binding modes at pH 7 (solid) and 11 (dashed). (B) g-factor spectra of purified: V96-Cys:CdS (green), V54-Cys:CdS (purple) and NAC:CdS (plum,). (C) CD spectra of purified NAC:CdS at pH 7 (solid) and pH 11 (dashed) and UV-Vis of NAC:CdS at pH 7 (solid) and pH 11 (dashed). Purified samples were pH adjusted with NaOH and TCEP•HCl.

To gain insight into the role of pH in determining the shape of the CD spectra of these samples we aimed to probe the protonation state of the thiol in V96-Cys:CdS, V54-Cys:CdS and NAC:CdS (**Figure 2.9A**). Purified samples of V96-Cys:CdS, V54-Cys:CdS, and NAC:CdS were pH adjusted using TCEP·HCl and sodium hydroxide (NaOH) (see **2.4.10** for experimental). First, TCEP·HCl was added to the samples to minimize disulfide bond formation, followed by NaOH addition until the solutions reached pH 11. The dissymmetry factors (*g*-factors, see **2.4.12.1 Eq 2.3** for method) were then plotted at pH values above and below the pKa of the thiol (**Figure 2.9B**). In general, when adjusting above and below the pKa of the thiol, we observed a modest change in the g-factor magnitudes at different wavelengths that were more prominent in the case of NAC:CdS and V54-Cys:CdS versus the V96-Cys:CdS sample (**Figure 2.9B**). Interestingly, for NAC:CdS the decrease in g-factor magnitude around 450 nm when comparing the pH 7 (solid) and pH 11 (dashed) spectra is notable. Overlaying the CD spectra and UV-Vis spectra of NAC:CdS suggest a sharpening of the derivative-shaped CD transition corresponding to the 2nd lowest energy electronic transition of the QD at pH 11 as highlighted by the black vertical line (**Figure 2.9C**). Previous work from Owen has demonstrated that the 2nd electronic transition is sensitive to surface chemistry,[48] and we hypothesize that X-type thiolate binding vs. L-type thiol binding can explain the sharpness in this transition at pH 11. Since similar changes are observable in V54-Cys:CdS but are less evident in V96-Cys:CdS, we propose that the steric bulk associated with the longer V96 peptide chain impedes ligand rearrangement on the surface of the QDs due to the sizeable entropic barrier that would need to be overcome.

To understand the impact of pH on the chirality of V96-Cys:CdS, V54-Cys:CdS and NAC:CdS, the magnitude of the average g-factors centered around the wavelength of the most intense transition (418 nm for ELP:CdS and 423 nm for NAC:CdS) (**Table 2.1**). From this data it

can be concluded there are no significant changes in the magnitude of chirality when probing thiolate vs. thiol coordination on the surface of the QDs. While there was no increase in the magnitude of chirality at this transition, we did observe more than a 2-fold increase in g-factor magnitude of NAC:CdS vs. the ELP:CdS. Previously Puri et. al. reported CdSe QDs with dicarboxylic acid having one additional chiral carbon center can increase g-factors by 30-fold when compared to their monocarboxylic acid counterparts.[34] Since the V96-Cys and V54-Cys have 289 and 163 chiral carbon centers respectively, we were expecting to see an increase in g-factor proportional to increase in ELP length which was not observed. However, due to the steric bulk of the ELPs vs. NAC we hypothesize that the surface ligand coverage is likely not the same between samples, making this comparison difficult.

Table 2.1 pH dependent average g-factors of ELP:CdS and NAC:CdS samples at their most intense responses.

	$\lvert g^{+}\text{-}g^{-} \rvert /2_{\text{ pH 11}}$	$\lvert g^{+}\text{-}g^{-} \rvert /2_{\text{ pH 7}}$
V96-Cys:CdS (418 nm)	$0.5\text{x}10^{-4}$	$0.6\text{x}10^{-4}$
V54-Cys:CdS (418 nm)	$0.5\text{x}10^{-4}$	$0.7\text{x}10^{-4}$
NAC:CdS (423 nm)	$1.5\text{x}10^{-4}$	$1.5\text{x}10^{-4}$

The ELP ligand exchange can also be monitored through changes in the hydrodynamic diameter of the ligand:CdS conjugate using DLS (**Figure 2.10**). After exchanging the hydrophobic oleate:CdS with glycine, the hydrodynamic diameter decreases from 11.5 ± 2.5 nm

to 6.7 ± 0.5 nm, consistent with a decrease in ligand length from oleate to glycine. Once the glycine:CdS are exchanged with V54-Cys and V96-Cys, the hydrodynamic diameter increases to 40 ± 0.5 and 45 ± 1.1 nm, respectively. These data are also in agreement with the larger hydrodynamic diameter of V96-Cys (10.5 ± 1.0 nm) relative to V54-Cys (8.4 ± 0.6 nm) (**Figure 2.11**).

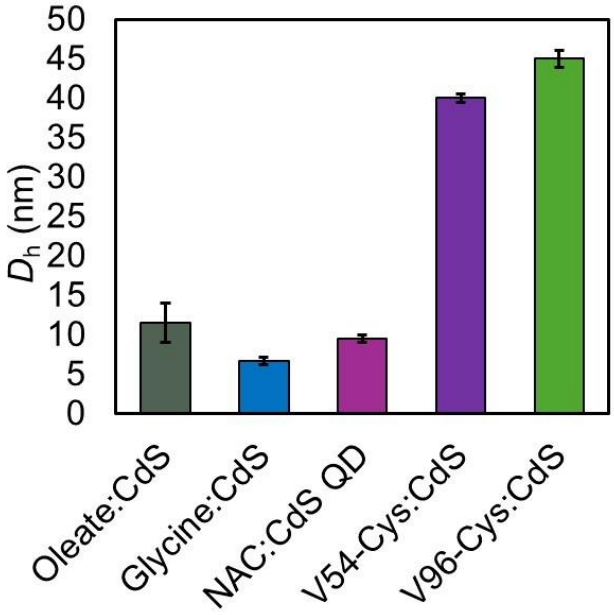

Figure 2.10 Average hydrodynamic diameter of CdS QDs with corresponding ligands as determined by DLS at 20 °C. The oleate:CdS was measured in toluene, while the remaining samples were measured in water.

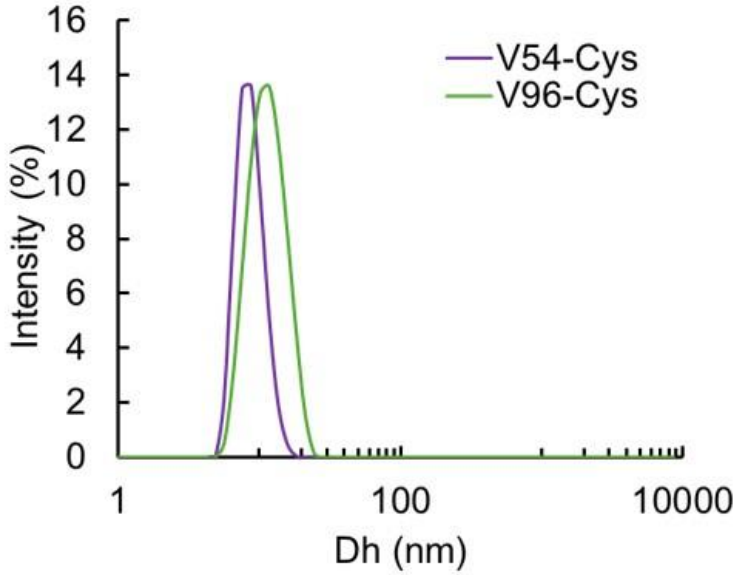

Figure 2.11 Size distribution of V54-Cys and V96-Cys in water at 20 °C at pH 7.

2.2.3 *Reversible ELP:CdS QD Thermoresponsive Coacervation*

The thermoresponsiveness of ELPs makes them attractive ligands for the synthesis of reconfigurable organic-inorganic hybrid materials. The most common example of these types of systems is ELP:gold nanoparticle (Au NP) conjugates.[28,49–55] Recently, V96-Cys ELP was successfully conjugated to 20 and 60 nm Au NP, with the ELP's dynamic coacervation resulting in red-shifted gold plasmonic absorbance features.[28] While ELP:CdSe nanostructures have been reported,[56] no information was provided on the dynamic coacervation of the hybrid material. In this section, we discuss the measured spectroscopic temperature response of V54-Cys:CdS and compare the V96-Cys:CdS and V54-Cys:CdS systems using SAXS. We note that a stark increase in turbidity accompanies spatial rearrangement during coacervation. Thus, the influence of coacervation on the optical properties of QDs cannot be studied in detail. Both V96-Cys:CdS and V54-Cys:CdS collapse into QD-dense coacervates when heated above the ELP transition temperatures, which are 32 °C[28] and 38 °C (**Figure 2.12**), respectively. While both the V96-

Cys:CdS and V54-Cys:CdS assemble, the spectroscopic response of the V54-Cys:CdS variant will be highlighted. For details on the thermoresponsive spectroscopic characterization of the V96-Cys:CdS system see (**Figure 2.13, Figure 2.14**).

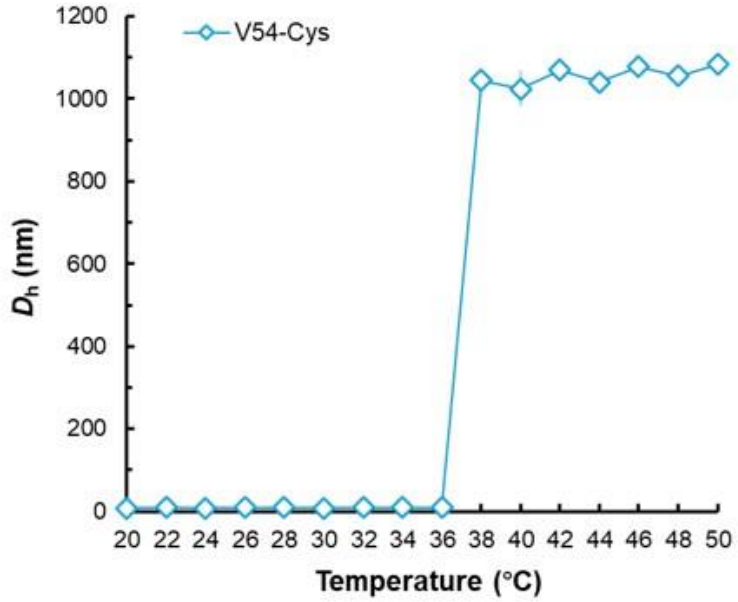

Figure 2.12 V54-Cys Transition temperature measured by DLS in water.

Variable temperature DLS spectra of the V54-Cys:CdS show that the particle-dense coacervates produced at 45 °C have an average size of 397 ± 4 nm and that they transition back to ELP-decorated QDs 50 ± 1 nm in average size upon incubation at 20 °C. This temperature-driven assembly-disassembly process is highly reproducible for at least three heating and cooling cycles (**Figure 2.13**). ELP-mediated clustering of QDs is also observed upon incubation of V96-Cys:CdS samples at 40 °C with larger coacervates (510 ± 2 nm) produced above the transition temperature and an average size of 53 ± 2 nm after a return to 20 °C. Like V54-Cys:CdS, the V96-Cys:CdS system also exhibits robust thermoreversibility over multiple heating and cooling cycles (**Figure 2.14**). Notably, for both V96-Cys:CdS and V54-Cys:CdS, the average particle

size after the first cycle at 20 °C is slightly larger than the original, consistent with hysteresis observed in similar dynamic polymer-nanoparticle systems.[28,57,58]

While DLS gives us insight into coacervate size, variable temperature CD of dilute (see SI) ELP:CdS provides information about secondary structure changes of the polypeptide bound to the QDs in solution. At 20 °C, ELP:CdS exhibits a strong negative CD signal at 196 nm, and when heated above the ELP transition temperature, the CD magnitude at 196 nm and 209 nm decreases (**Figure 2.13C**, **Figure 2.15**). Literature suggests this corresponds to the conversion of polyproline II-like helical structures to β-structures during coacervation.[55,59–61] These secondary structure changes are also observed for the coacervation of the native ELP (**Figure 2.16A, B**). Unfortunately, the turbidity of the ELP:CdS coacervates makes it difficult to observe spectroscopic changes at visible wavelengths in these samples (**Figure 2.17)**.

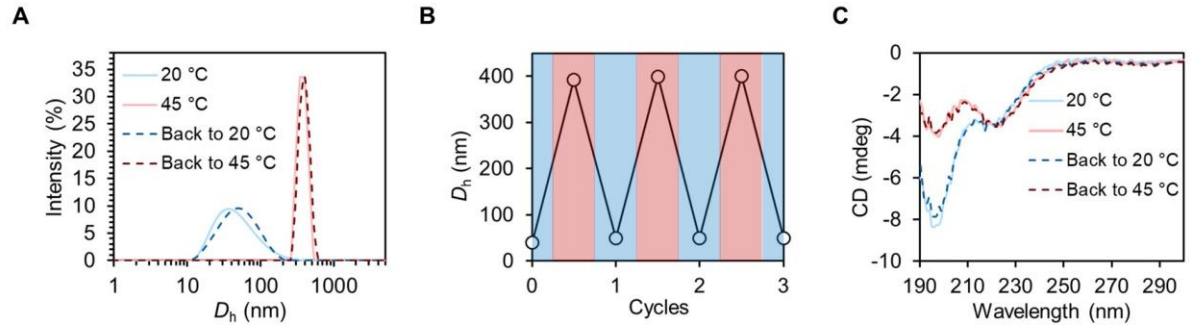

Figure 2.13 (A) Variable temperature DLS spectra of V54-Cys:CdS and (B) corresponding hydrodynamic diameter during temperature cycling. (C) Deep UV variable temperature CD spectra of V54-Cys:CdS.

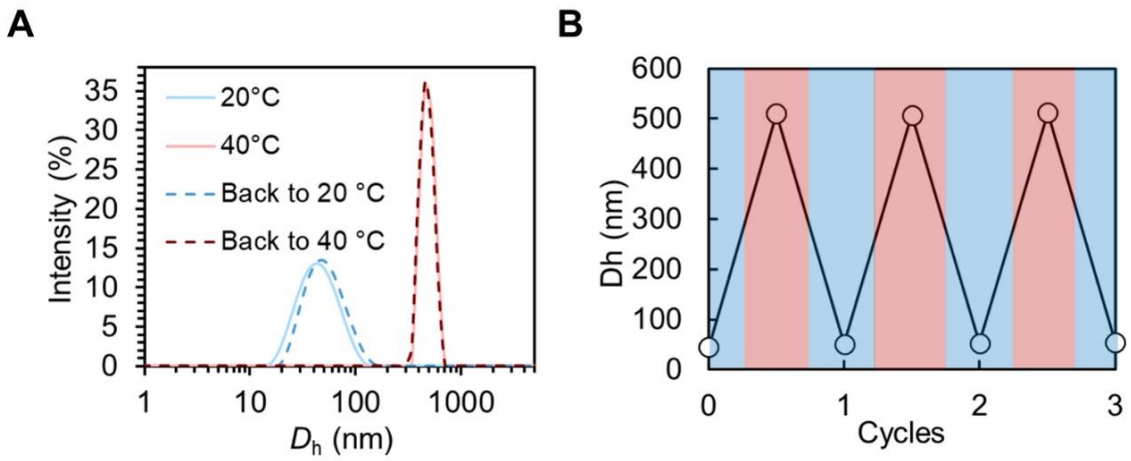

Figure 2.14 (A) Variable temperature DLS of V96-Cys:CdS in water. (B) Variable temperature cycles of V96-Cys:CdS.

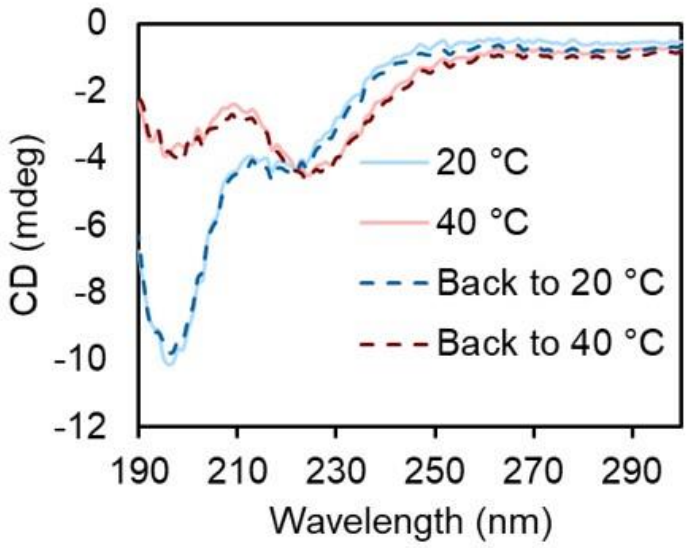

Figure 2.15 Variable temperature CD spectra of V96-Cys:CdS in water.

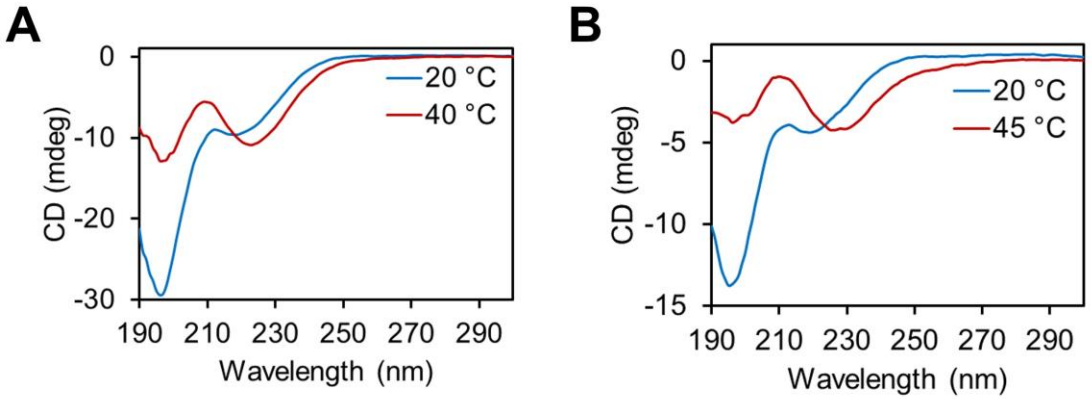

Figure 2.16 (A) Variable temperature CD of 0.5 μM V96-Cys ELP in water. (B) Variable temperature CD of 1 μM V54-Cys in water.

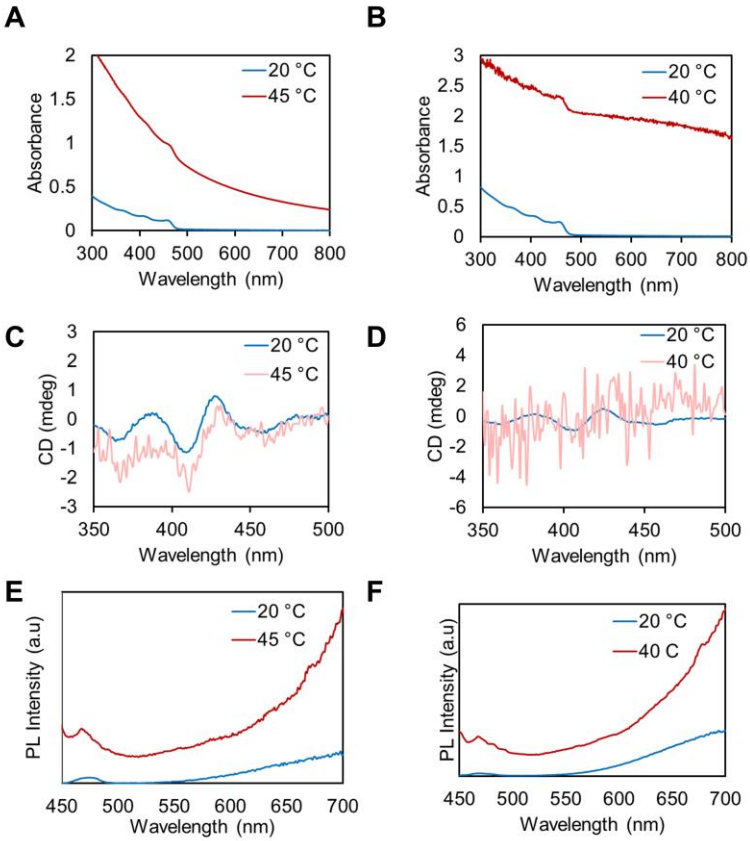

Figure 2.17 (A) Variable temperature UV-vis spectra of V54-Cys:CdS in water. (B) Variable temperature UV-vis spectra of V96-Cys:CdS in water. (C) Variable temperature CD spectra of V54-Cys:CdS in water. (D) Variable temperature CD spectra of V96-Cys:CdS in water. (E)

Variable temperature PL spectra of V54-Cys:CdS in water. (F) Variable temperature PL spectra of V96-Cys:CdS in water.

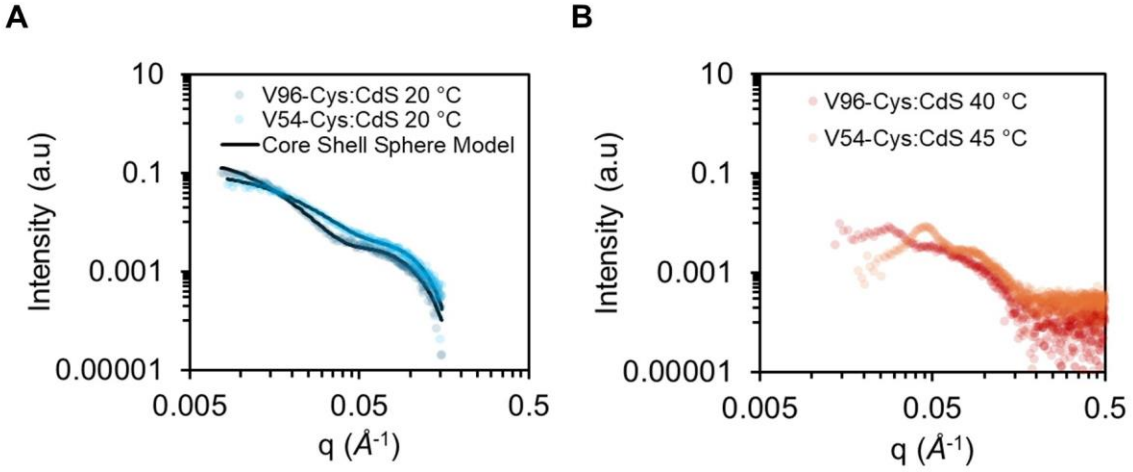

Figure 2.18 (A) Scattering Curves of V96-Cys:CdS (gray) and V54-Cys:CdS (blue) at 20 °C. The core shell model was used to fit both curves (black line). (B) Scattering curves of V96-Cys:CdS (red) and V54-Cys:CdS at 40 °C and 45 °C, respectively.

SAXS profiles reveal the presence of QDs in V96-Cys:CdS and V54-Cys:CdS coacervates in the solution phase. The initial measurement of the V96-Cys:CdS and V54-Cys:CdS samples were taken at 20 °C (**Figure 2.18A**) and fit to a core-shell sphere model[62] revealing QDs 4.6 nm in diameter, with a shell thickness of 8.6 nm for V96-Cys:CdS and 6.2 nm for the V54-Cys:CdS, respectively (for further explanation including assumptions and limitations of the core-shell sphere model, see **2.4.15** experimental). When the ELP:CdS solutions are heated above their transition temperatures, distinct scattering features are observed in both ELP:CdS samples (**Figure 2.18B**) that are not present in the glycine:CdS samples (**Figure 2.19**). These peaks imply a dense CdS QD particle packing mediated by the coacervated ELPs that decorate their surface. Fitting coacervated samples of V96-Cys:CdS and V54-Cys:CdS using a broad peak model reveals interparticle distances of 22.9 nm and 13.7 nm, respectively. The

distance discrepancy of the ELP:CdS systems are rationalized by the ligand shell thickness of V96-Cys:CdS (8.6 nm) and V54-Cys:CdS (6.2 nm). These systems were also tested for reversibility by collecting scattering curves at 20 °C after coacervation. The V96-Cys:CdS QD scattering curve at 20 °C after cycling to 40 °C is similar to the original 20 °C curve (**Figure 2.20A**), demonstrating reversible coacervation. However, the V54-Cys:CdS samples displayed less reversibility based on the scattering curve at 20 °C after heating to 45 °C (**Figure 2.20B)**. These differences are consistent with the DLS measurements taken at 20 °C after heating of the V96-Cys:CdS and V54-Cys:CdS systems (**Figure 2.13, Figure 2.14**, blue dashed lines), where the V96-Cys:CdS system has a narrower size population distribution than V54-Cys:CdS after heat cycling. These differences in reversibility indicate ELP-dependent hysteresis in the assembly/disassembly of this organic-inorganic hybrid material, which we hypothesize may be due to (1) differences in the polypeptide:QD size ratios (~1.9 for V96-Cys:CdS and ~1.3 for V54-Cys:CdS) and (2) the differences in hydrophobicity of ELPs with the change in length. The second point is corroborated by Unsworth and coworkers, who found an inverse relationship between chain length and hysteresis.[63] Moving forward, the length of the ELPs should be considered for the rational design of these thermally responsive hybrid materials.

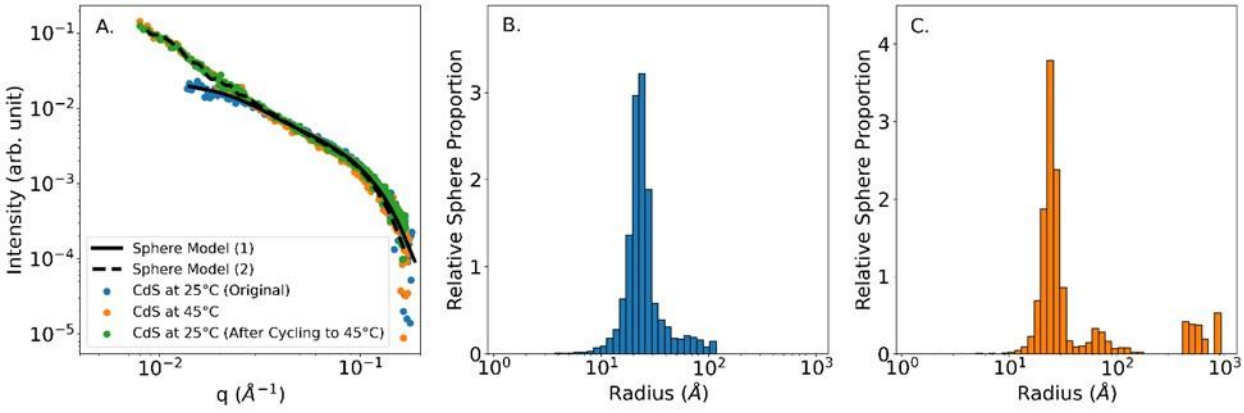

Figure 2.19 (A) Scattering curves of glycine:CdS in water. A measurement was taken of the sample at either 25°C or 45°C and a polydisperse sphere model was used to fit the data to

determine the size distribution. The first measurement, CdS at 25°C (Original), was taken after setting the sample's temperature to 25°C. The second, (2) CdS at 45°C, was when the sample was then heated to 45°C, and the third, CdS at 25°C (After Cycling to 45°C), was when the sample was cooled back to 25°C. (B) Size distribution of sphere sizes obtained from fitting Sphere Model (1) on the scattering data. (C) Size distribution of sphere sizes obtained from fitting Sphere Model (2) on the scattering data. Model fitting was performed using the McSAS software.

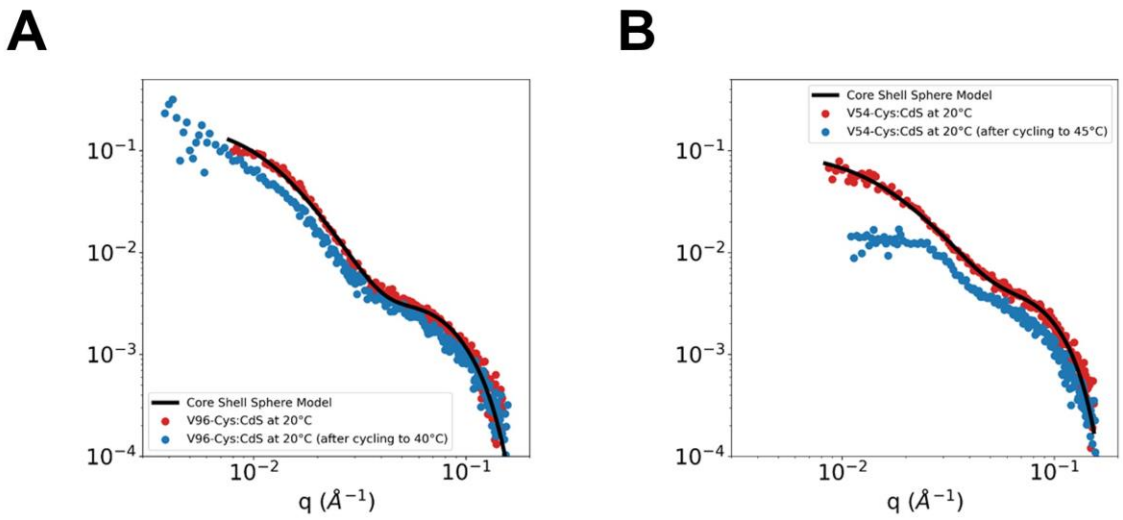

Figure 2.20 (A) Scattering curves of V96-Cys:CdS at 20°C and 20°C after cycling to 45°C. The core shell sphere model was used to fit the data. From the fit, a core radius of 2.3 nm was obtained with a shell thickness of 8.6 nm, a thickness lognormal polydispersity of 0.39, and a shell scattering length density of 1.11×10^{-5} Å^{-2}. The scattering length density of the core was assumed to be that of CdS which was 6.54×10^{-5} Å^{-2} and the solvent was assumed to be that of water which was 9.74×10^{-6} Å^{-2}. (B) Scattering curves of V54-Cys:Cds at 20°C and 20°C after cycling to 45°C. The core shell sphere model was used to fit the data. From the fit, a core radius of 2.3 nm was obtained with a shell thickness of 6.2 nm, a shell scattering length density of 1.12×10^{-5} Å^{-2}, and a shell thickness lognormal polydispersity of 0.39. The scattering

length density of the core was assumed to be that of CdS which was 6.54×10^{-5} Å^{-2} and the solvent was assumed to be that of water which was 9.74×10^{-6} Å^{-2}.

Finally, the structure of the V54-Cys:CdS particle-dense coacervates was investigated by (S)TEM (**Figure 2.21**) as well as V96-Cys:CdS coacervates (**Figure 2.22**). Below the ELP transition temperature, V54-Cys:CdS particles are relatively dispersed and do not show interparticle close-packing on the TEM grid (**Figure 2.21A**). QDs with relatively short ligands, such as the oleate:CdS or glycine:CdS (**Figure 2.1**), exhibit close-packing on the TEM grid, and the absence of this effect for the V54-Cys:CdS can be rationalized by the relatively large size of the ELP ligand. To confirm the structure of the coacervate, V54-Cys:CdS was incubated above the transition temperature and prepared for electron microscopy (see **2.4.14** experimental). Bright-field TEM reveals quasi-spherical coacervates around 500 nm in diameter composed of dense QDs presumably held together by coacervated ELP ligands (**Figure 2.21B**). Scanning TEM reveals the organic ELP component at a higher contrast, observed as the white haze surrounding the QDs within the coacervate (**Figure 2.21C**). The coacervate is decorated by small organic structures about 15-35 nm in diameter, seen both in the bright-field TEM and scanning TEM images, and these are assigned to QD-free ELP clusters. Higher magnification images of the coacervates (**Figure 2.21B**, inset) reveal the individual QDs within the coacervate. It is worth noting that the QDs are not ordered in the dried coacervate, and cryogenic TEM images (**Figure 2.21D**) of small coacervates also do not show ordering.

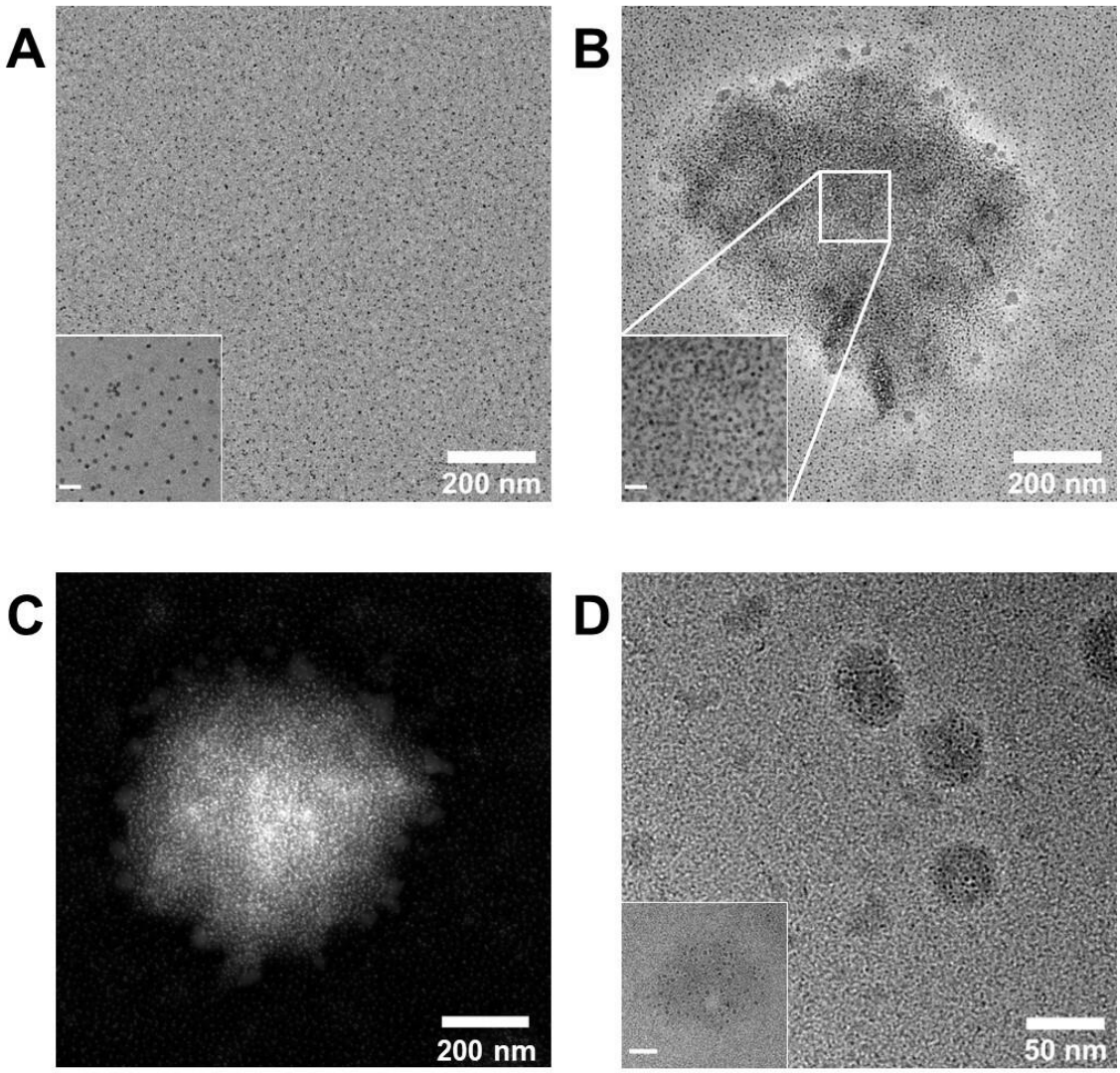

Figure 2.21 TEM images of V54-Cys:CdS prepared at (A) 20 °C and at (B) 45 °C. (C) Scanning TEM image of V54-Cys:CdS prepared at 45 °C. (D) Cryogenic TEM images of V54-Cys:CdS prepared at 45 °C. Higher magnification insets have a 20 nm scale bar.

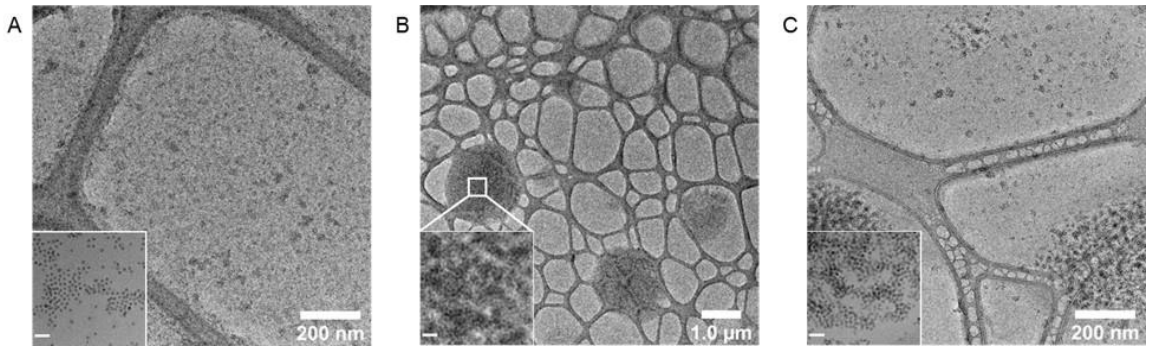

Figure 2.22 TEM images of V96-Cys:CdS prepared at 20 °C (A) and at 40 °C (B and C), with insets of higher magnification, 20 nm scale bars. Below the transition temperature, V96-Cys:CdS is observed in monolayers or small (<20 nm) aggregates. Above the transition temperature, 1-2 µm coacervates are observed with densely packed interiors (B). The coacervates appear to have some structuring of small aggregates (C) similar to those observed below the transition temperature.

2.3 CONCLUSIONS

In summary, we have developed a two-step ligand exchange method to bind V96-Cys and V54-Cys ELPs to CdS QDs. The exchange is confirmed using CD spectroscopy in the visible light region by observing a chiral absorbance corresponding to the excitonic transitions of the CdS QD. By comparing the chirality-induced CD response for a range of small molecule model ligands, including NAC, L-Cys, and L-Cys-Me, V96-Cys, and V54-Cys were determined to bind to CdS QDs through the C-terminal cysteine residue preferentially. This is the first literature example of post-synthetically inducing exciton chirality in QDs using proteins or polypeptides. Notably, we were able to identify the amino acid bound to the QD surface using µM concentration of polypeptide compared to the mM or higher concentrations previously used with L-Cys and QDs for NMR studies. This highlights the advantage of using CD to determine

protein-QD surface interaction, particularly in biologically relevant environments, where protein concentration is limited by solubility. Additionally, for the first time, we reported the reversible coacervation of ELP:CdS by DLS and CD spectroscopies and confirmed the coacervate structure through (S)TEM. Moreover, analysis of SAXS data revealed increased spatial ordering of CdS QDs in both V96-Cys:CdS and V54-Cys:CdS systems, highlighting the ELP's ability to drive assembly in these hybrid materials. This study demonstrates the usefulness of circular dichroism in determining the success of a biological ligand exchange on quantum dots. We believe this technique can be applied to a diverse set of bio-ligand:QD systems in the future. Furthermore, leveraging the knowledge gained in this study about the ELP:QD surface interaction, we aim to study more complex inorganic nanostructures conjugated with ELPs that dynamically coacervate in a manner that exploits both the properties of the ELP and the inorganic nanostructure to access a broad library of functional hybrid materials with emergent functionality.

2.4 Experimental Section

2.4.1 *Materials*

Oleic acid (90%), tetramethylthiourea (98%), tetramethyl ammonium hydroxide (1M aqueous), glycine (98%), N-acetyl-L-cysteine (≥99%), L-cysteine (97%), L-cystine (99.7%), L-cysteine methyl ester hydrochloride (≥95%), Tris(2-carboxyethyl)phosphine hydrochloride (≥98%), methanol (≥99.9%), and toluene (≥99.8%) were purchased from MilliporeSigma and used without further purification. Dowtherm® was purchased from Dow Inc. and used without further purification. Hexadecane (99%) was purchased from MilliporeSigma, dried over calcium choride, distilled, and stored in a glovebox. Cadmium oleate was synthesized following a literature procedure.[64] 18.2 MΩ water was collected from an EMD Millipore purification system.

UV-vis spectra were collected on a Cary 60 spectrophotometer from Agilent. Photoluminescence spectra were collected on a Horiba Scientific FluoroMax-4 Spectrofluorometer.

2.4.2 *Synthesis of $(VPGVG)_{54}$-Cys and $(VPGVG)_{96}$-Cys ELPs*

The construction of plasmid pET25(+)-ELP(V96), which encodes V96-Cys, was previously described.[49]The gene encoding V54-Cys was obtained as a truncated PCR amplification product during the construction of pET25(+)-ELP(V96). It was inserted into pET25(+) to produce pET25(+)-ELP(V54). Plasmids were introduced into *E. coli* BL21(DE3) cells and proteins were expressed and purified as described[28] and stored at 4 °C.

2.4.3 *Synthesis of Oleate:CdS*

The synthesis of CdS QDs was adapted from Hamachi et al.[64] Cadmium oleate (1.287g, 1.9 mmol), oleic acid (1.3 mL, 4.1 mmol), and hexadecane (60 mL) were added to a dried three-neck 250 mL round-bottom flask equipped with a stir bar, thermowell, reflux condenser, and rubber septum. The flask was evacuated at 90 °C for 1 h. Next, the flask was put under dynamic nitrogen and heated to 230 °C. In a nitrogen atmosphere, tetramethylthiourea (TMTU, 0.2075 g, 1.6 mmol) was dissolved in Dowtherm (3.0 mL). The TMTU solution was rapidly injected into the cadmium oleate solution and allowed to react for 3 h until there were no UV-Vis absorbance changes. The temperature was then lowered to 120 °C, and the condenser was quickly replaced by a distillation arm equipped with a 250 mL round-bottom flask, and the solvent was removed via vacuum distillation. Once cooled to room temperature, in air, minimal toluene was added, and the solution was transferred to centrifuge tubes followed by precipitation with methanol (3:1, methanol: toluene) and centrifugation at 8,000 RPM for 10 mins. The supernatant was discarded,

and the yellow pellet was redissolved in minimal toluene. This process was repeated for 3 precipitation and centrifugation cycles. The pellet was then suspended in 10 mL of toluene and centrifuged at 8,000 RPM for 10 minutes. The yellow supernatant was then decanted away and stored in a vial in the air. The QDs were characterized by an absorption maximum at 461 nm and were 4.8 ± 0.4 nm in diameter via TEM analysis.

2.4.4 *Synthesis of Glycine:CdS*

The synthesis of Glycine:CdS was adapted from Tohga et al.[1] The concentration of QDs was determined using the Peng sizing curve.[31] To a vial, oleate:CdS (10 nmoles) was added and dried. In a separate vial, glycine (0.589 g, 7.8 mM) was added with 1M aqueous tetramethylammonium hydroxide (TMAOH, 3 mL) and stirred at room temperature for 10 minutes. The TMAOH solution was then added to the QD solid and stirred vigorously in the dark for 24 h. To this solution, 3 mL of toluene was added and vigorously stirred. This solution was centrifuged at 8,000 RPM for 10 minutes, producing a slightly yellow organic layer and a dark yellow bottom layer. The top layer was removed, and 3 mL of toluene was added, followed by vortexing. This washing and centrifugation process was repeated for 3 total cycles. The resulting solution was then centrifuged using a 15,000 kDa centrifuge filter and centrifuged at 5,000 RPM for 10 minutes. The colorless filtrate was discarded, and 2 mL of 18 MΩ water was added to the QD solution. This centrifuge filtration process was repeated 3 times. The resulting QDs show an absorption maximum at 455 nm and were 4.11 ± 0.4 nm in diameter via TEM analysis.

2.4.5 *Synthesis of V96-Cys:CdS and V54-Cys:CdS*

The concentration of Glycine:CdS QDs was determined using the Peng sizing curve.[31] $(VPGVG)_{96}C$ or $(VPGVG)_{54}C$ (V96-Cys, V54-Cys, 0.5 μmol) was dissolved in 18 MΩ water (1.5 mL). In a separate vial, a solution of Tris(2-carboxyethyl)phosphine hydrochloride (TCEP•HCl, 67.1 mg, 0.234 mmol) in 18 MΩ water (1 mL) was prepared. The TCEP•HCl solution (21.4 μL, 5 μmol) was then added to the V96-Cys or V54-Cys solutions and stored at 4 °C for 1 h. Next, glycine:CdS QDs (387 μL, 1.4 nmol) were added to the ELP solutions and diluted with water (591 μL). The solutions were then pH adjusted with TMAOH (1M, 200 μL) until pH was 11. These solutions were stored in the dark at 4 °C overnight. After overnight incubation, the QD solutions were heated to 45 °C for 20 minutes and centrifuged at 5,000 PM for 10 minutes. The resulting colorless supernatant was discarded, and the yellow pellet was dissolved in chilled 18 MΩ water (2 mL). The heat centrifugation was repeated for 2 cycles, and the resulting pellet was dissolved in 2 mL of 18 MΩ water and transferred to a prepared Float-A-Lyzer® dialysis device. The solutions were dialyzed against 500 mL of 18 MΩ water. The water was replaced at 2 and 4 hours before leaving overnight in 1 L of 18 MΩ water. The dialyzed samples were then lyophilized overnight, and the resulting yellow solid was dissolved in 18 MΩ water (2.5 mL) and stored in the dark at 4 °C unless being used for analysis. [V96-Cys:CdS]: 0.180 μM [V54-Cys:CdS]: 0.310 μM calculated from Peng sizing curve.[31]

2.4.6 *Synthesis of N-Acetyl-L-Cysteine (NAC):CdS*

Samples were prepared in a similar manner as V96-Cys:CdS and V54-Cys:CdS QD. First, NAC (9.1 mg, 56 μmol) was dissolved in 18 MΩ water (10 mL). Next, TCEP•HCl (67.1 mg, 0.234 mmol) was prepared in 18 MΩ water (1 mL). The NAC solution (89.3 μL, 0.5 μmol) was then

added to a new vial, followed by the addition of the TCEP solution (21.4 µL, 5 µmol) and stored at 4 °C for 1 hour. After 1 hour, added glycine:CdS QDs (221 µL, 1.4 nmol) and additional 18 MΩ water (1.968 mL) followed by TMAOH (1M, 200 µL) and stored at 4 °C overnight. After incubation, the solution was centrifuged at 8,000 RPM for 10 minutes. The supernatant was then transferred to a 30 kDa centrifuge filter and centrifuged at 8,000 RPM for 5 minutes. The colorless filtrate was discarded, and 18 MΩ water was added to the QD solution, and it was centrifuged again at 8,000 RPM for 5 minutes; this process was repeated for 5 cycles. After the 5th cycle, 18 MΩ water (2.3 mL) was added back to the final solution and was stored at 4 °C in the dark unless being used for analysis. [NAC:CdS]: 0.180 µM calculated from Peng sizing curve.[31]

2.4.7 *Synthesis of L-Cysteine (L-Cys):CdS*

Samples were prepared in a similar manner as V96-Cys:CdS and V54-Cys:CdS QD. First, L-Cys (5.5 mg, 45 µmol) was dissolved in 18 MΩ water (10 mL). Next, TCEP•HCl (18.2 mg, 0.0635 mmol) was prepared in 18 MΩ water (1 mL). The L-Cys solution (112 µL, 0.5 µmol) was then added to a new vial, followed by the addition of the TCEP solution (78.7 µL, 5 µmol) and stored at 4 °C for 1 hour. After 1 hour, added glycine:CdS QDs (420 µL, 1.4 nmol) and an additional 18 MΩ water (1.681 mL) followed by TMAOH (1M, 200 µL) and stored at 4 °C overnight. After incubation, the solution was centrifuged at 8,000 RPM for 10 minutes. The supernatant was then transferred to a 30 kDa centrifuge filter and centrifuged at 8,000 RPM for 5 minutes. The colorless filtrate was discarded, and 18 MΩ water was added to the QD solution, and it was centrifuged again at 8,000 RPM for 5 minutes; this process was repeated for 5 cycles. After the 5th cycle, 18 MΩ water (2.3 mL) was added back to the final solution and was stored at

4 °C in the dark unless being used for analysis. [L-Cys:CdS]: 0.400 μM calculated from Peng sizing curve.[31]

2.4.8 *Synthesis of L-Cysteine Methyl Ester (L-Cys-Me):CdS*

Samples were prepared in a similar manner as V96-Cys:CdS and V54-Cys:CdS QD. First, L-Cys-Me•HCl (9.6 mg, 56 μmol) was dissolved in 18 MΩ water (10 mL). Next, TCEP•HCl (18.2 mg, 0.0635 mmol) was prepared in 18 MΩ water (1 mL). The L-Cys-Me solution (87.7 μL, 0.5 μmol) was then added to a new vial, followed by the addition of the TCEP solution (78.7 μL, 5 μmol) and stored at 4 °C for 1 hour. After 1 hour, added glycine:CdS QDs (420 μL, 1.4 nmol) and an additional 18 MΩ water (1.714 mL) followed by TMAOH (1M, 200 μL) and stored at 4 °C overnight. After incubation, the solution was centrifuged at 8,000 RPM for 10 minutes. The supernatant was then transferred to a 30 kDa centrifuge filter and centrifuged at 8,000 RPM for 5 minutes. The colorless filtrate was discarded, and 18 MΩ water was added to the QD solution, and it was centrifuged again at 8,000 RPM for 5 minutes; this process was repeated for 5 cycles. After the 5th cycle, 18 MΩ water (2.3 mL) was added back to the final solution and was stored at 4 °C in the dark unless being used for analysis. [L-Cys-Me:CdS]: 0.390 μM calculated from Peng sizing curve.[31]

2.4.9 *Synthesis of L-Cystine (L-Cys-Cys):CdS*

The synthesis of Glycine:CdS was adapted from Tohga et al.[1] The concentration of QDs was determined using the Peng sizing curve.[31] To a vial, oleate:CdS (6.9 nmoles) was added and dried. In a separate vial, L-cystine (0.075 g, 0.31 mM) was added with 1M aqueous

tetramethylammonium hydroxide (TMAOH, 2 mL) and stirred at room temperature for 10 minutes. The TMAOH solution was then added to the QD solid and stirred vigorously in the dark for 24 h. To this solution, 3 mL of toluene was added and vigorously stirred. This solution was centrifuged at 8,000 RPM for 10 minutes, producing a slightly yellow organic layer and a dark yellow bottom layer. The top layer was removed, and 3 mL of toluene was added, followed by vortexing. This washing and centrifugation process was repeated for 3 total cycles. The resulting solution was then centrifuged using a 15,000 kDa centrifuge filter and centrifuged at 8,000 RPM for 5 minutes. The colorless filtrate was discarded, and 2 mL of 18 MΩ water was added to the QD solution. This centrifuge filtration process was repeated 5 times. After the 5th cycle, 18 MΩ water (2.3 mL) was added back to the final solution and was stored at 4 °C in the dark unless being used for analysis. [L-Cystine:CdS]: 0.290 μM calculated from Peng sizing curve.[31]

2.4.10 *pH Adjustment of ELP:CdS and NAC:CdS Samples*

TCEP•HCl (0.207 M, aqueous, 27.1 μL) was added to V96-Cys:CdS, V54-Cys:CdS and NAC:CdS solutions to prevent disulfide bond formation (pH~5). NaOH (1N, aqueous) was then added to each of the samples in 10 uL aliquots until pH was 11 (~50 μL). To adjust the pH to 7 TCEP•HCl (0.207 M, aqueous) was added in 10 uL aliquots until pH was 7 (~20 μL).

2.4.11 *Concentration of ELP:CdS in Deep UV CD*

Both V96-Cys:CdS and V54-Cys:CdS samples were diluted by a factor of 167. [V96-Cys:CdS]: 0.1 nM, [V54-Cys:CdS]: 0.2 nM.

2.4.12 *Circular Dichroism*

Spectra were collected on a Jasco J-720 spectrophotometer equipped with a temperature controller from Jasco. Scan rate: 100 nm, Data pitch: 1nm, bandwidth: 10 nm, path length:1 cm.

Equation 2.1 ΔA/A normalization of CD spectra

$$\frac{\Delta A}{A_{\lambda max}} = \frac{\frac{CD(mdeg)}{32980}}{\text{Abs at lowest energy } \lambda_{max} \text{ electronic transition}}$$

Equation 2.2 *g*-factor at specific wavelength

$$\frac{\Delta A}{A} = \frac{\frac{CD(mdeg)}{32980}}{Abs}$$

Equation 2.3 Average *g*-factor

$$\frac{|g^+ - g^-|}{2}$$

$$= \frac{\left| \frac{\frac{CD(mdeg) \text{ at } \lambda_{max} \text{ of most positive intensity}}{32980}}{\text{Abs at } \lambda_{max} \text{ of most positive intensity}} - \frac{\frac{CD(mdeg) \text{ at } \lambda_{max} \text{ of most negative intensity}}{32980}}{\text{Abs at } \lambda_{max} \text{ of most negative intensity}} \right|}{2}$$

2.4.13 *DLS Analysis*

Dynamic light scattering (DLS) measurements were performed on a Malvern Zetasizer Nano ZS with an 800 nm laser. The extinction coefficient used was for bulk CdS for all samples, and the refractive index used was for water in all samples except Oleate:CdS samples. Scattering data were fit using a multipeak model in the Malvern Zetasizer software.

2.4.14 *TEM Preparation and Analysis*

TEM images were collected on a FEI Tecnai G2 F20 SuperTwin microscope operated at 200 keV for bright field, cryo and STEM. Solutions of ligand:CdS were prepared for TEM grid preparation by diluting by a factor of 2 from the solutions used for CD and SAXS. Room temperature samples were prepared by dropcasting 5 μL of ligand:QD in water (or toluene for native oleate-capped QDs) onto a suspended TEM grid, which was then allowed to dry fully (10 min) and placed under vacuum overnight. To prepare TEM grids at 45 °C, the V54-Cys:QD solution was placed in a 45 °C chamber for 4 minutes (solution becomes turbid), dropcast 5 μL onto a suspended TEM grid, which was then allowed to dry in the warm 45 °C chamber (5 min) and placed under vacuum overnight. TEM size analysis was performed using manual analysis in ImageJ based on images from at least two different grid locations and over 300 particle diameter measurements per sample. Cryogenic TEM samples were prepared using a Vitrobot Mark IV System, with liquid ethane as the coolant. Samples were prepared as above, incubated on a hot plate at 45 °C, and dropcast onto C-flat^{TM} grids. Imaging was performed using the Gatan CT3500 single-tilt liquid nitrogen cryo-transfer holder.

2.4.15 *SAXS Analysis*

SAXS was performed on a Xenocs Xeuss 3.0 (Grenoble, France) instrument with an x-ray energy of 8.04 keV (wavelength 1.54 Å) using a copper K-α microfocus source. Data was collected in two configurations: mid-q (0.007 - 0.020 Å^{-1}) for 30 minutes, and high-q (0.020 - 0.200 Å^{-1}) for 15 minutes. Samples were loaded in a 1.5mm diameter thin-walled quartz capillary purchased from Charles Supper (Westborough, MA, USA). The Peltier stage provided by Xenocs was used to vary the temperature of the samples. Background subtraction was

performed by subtracting the scattering of water measured using the same configurations. Data reduction and merging were performed using the XSCAT software (Xenocs Inc.). Data fitting was performed using either Sasview (*http://www.sasview.org/*) or McSAS.[65]

2.5 REFERENCES

(1) Tohgha, U.; Varga, K.; Balaz, M. Achiral CdSe Quantum Dots Exhibit Optical Activity in the Visible Region upon Post-Synthetic Ligand Exchange with D- or L-Cysteine. Chem. Commun. 2013, 49 (18), 1844–1846. https://doi.org/10.1039/C3CC37987F.

(2) Tohgha, U.; Deol, K. K.; Porter, A. G.; Bartko, S. G.; Choi, J. K.; Leonard, B. M.; Varga, K.; Kubelka, J.; Muller, G.; Balaz, M. Ligand Induced Circular Dichroism and Circularly Polarized Luminescence in CdSe Quantum Dots. ACS Nano 2013, 7 (12), 11094–11102. https://doi.org/10.1021/nn404832f.

(3) Moloney, M. P.; Gun'ko, Y. K.; Kelly, J. M. Chiral Highly Luminescent CdS Quantum Dots. Chem. Commun. 2007, No. 38, 3900–3902. https://doi.org/10.1039/B704636G.

(4) Elliott, S. D.; Moloney, M. P.; Gun'ko, Y. K. Chiral Shells and Achiral Cores in CdS Quantum Dots. Nano Lett. 2008, 8 (8), 2452–2457. https://doi.org/10.1021/nl801453g.

(5) Zhou, Y.; Yang, M.; Sun, K.; Tang, Z.; Kotov, N. A. Similar Topological Origin of Chiral Centers in Organic and Nanoscale Inorganic Structures: Effect of Stabilizer Chirality on Optical Isomerism and Growth of CdTe Nanocrystals. J. Am. Chem. Soc. 2010, 132 (17), 6006–6013. https://doi.org/10.1021/ja906894r.

(6) Ben-Moshe, A.; Teitelboim, A.; Oron, D.; Markovich, G. Probing the Interaction of Quantum Dots with Chiral Capping Molecules Using Circular Dichroism Spectroscopy. Nano Lett. 2016, 16 (12), 7467–7473. https://doi.org/10.1021/acs.nanolett.6b03143.

(7) Han, P.; Du, T.; Yang, X.; Zhao, Y.; Zhou, S.; Zhao, J. Optical Activity and Excitonic Characteristics of Chiral CdSe Quantum Dots. J. Phys. Chem. Lett. 2024, 15 (12), 3249–3257. https://doi.org/10.1021/acs.jpclett.3c03554.

(8) Dameron, C. T.; Winge, D. R. Characterization of Peptide-Coated Cadmium-Sulfide Crystallites. Inorg. Chem. 1990, 29 (7), 1343–1348. https://doi.org/10.1021/ic00332a011.

(9) Monahan, M.; Cai, B.; Jian, T.; Zhang, S.; Zhu, G.; Chen, C.-L.; Yoreo, J. J. D.; Cossairt, B. M. Peptoid-Directed Assembly of CdSe Nanoparticles. Nanoscale 2021, 13 (2), 1273–1282. https://doi.org/10.1039/D0NR07509D.

(10) Monahan, M.; Homer, M.; Zhang, S.; Zheng, R.; Chen, C.-L.; De Yoreo, J.; Cossairt, B. M. Impact of Nanoparticle Size and Surface Chemistry on Peptoid Self-Assembly. ACS Nano 2022, 16 (5), 8095–8106. https://doi.org/10.1021/acsnano.2c01203.

(11) Ma, N.; Yang, J.; Stewart, K. M.; Kelley, S. O. DNA-Passivated CdS Nanocrystals: Luminescence, Bioimaging, and Toxicity Profiles. Langmuir 2007, 23 (26), 12783–12787. https://doi.org/10.1021/la7017727.

(12) Gil, H. M.; Price, T. W.; Chelani, K.; Bouillard, J.-S. G.; Calaminus, S. D. J.; Stasiuk, G. J. NIR-Quantum Dots in Biomedical Imaging and Their Future. iScience 2021, 24 (3), 102189. https://doi.org/10.1016/j.isci.2021.102189.

(13) Garai-Ibabe, G.; Saa, L.; Pavlov, V. Enzymatic Product-Mediated Stabilization of CdS Quantum Dots Produced In Situ: Application for Detection of Reduced Glutathione, NADPH, and Glutathione Reductase Activity. Anal. Chem. 2013, 85 (11), 5542–5546. https://doi.org/10.1021/ac4007705.
(14) Probst, C. E.; Zrazhevskiy, P.; Bagalkot, V.; Gao, X. Quantum Dots as a Platform for Nanoparticle Drug Delivery Vehicle Design. Inorg. Nanoparticle Platf. 2013, 65 (5), 703–718. https://doi.org/10.1016/j.addr.2012.09.036.
(15) Sun, M.; Xu, L.; Qu, A.; Zhao, P.; Hao, T.; Ma, W.; Hao, C.; Wen, X.; Colombari, F. M.; de Moura, A. F.; Kotov, N. A.; Xu, C.; Kuang, H. Site-Selective Photoinduced Cleavage and Profiling of DNA by Chiral Semiconductor Nanoparticles. Nat. Chem. 2018, 10 (8), 821–830. https://doi.org/10.1038/s41557-018-0083-y.
(16) Urry, D. W. Free Energy Transduction in Polypeptides and Proteins Based on Inverse Temperature Transitions. Prog. Biophys. Mol. Biol. 1992, 57 (1), 23–57. https://doi.org/10.1016/0079-6107(92)90003-O.
(17) Urry, D. W.; Long, M. M.; Cox, B. A.; Ohnishi, T.; Mitchell, L. W.; Jacobs, M. The Synthetic Polypentapeptide of Elastin Coacervates and Forms Filamentous Aggregates. Biochim. Biophys. Acta BBA - Protein Struct. 1974, 371 (2), 597–602. https://doi.org/10.1016/0005-2795(74)90057-9.
(18) Roberts, S.; Dzuricky, M.; Chilkoti, A. Elastin-like Polypeptides as Models of Intrinsically Disordered Proteins. FEBS Lett. 2015, 589 (19PartA), 2477–2486. https://doi.org/10.1016/j.febslet.2015.08.029.
(19) McDaniel, J. R.; MacKay, J. A.; Quiroz, F. G.; Chilkoti, A. Recursive Directional Ligation by Plasmid Reconstruction Allows Rapid and Seamless Cloning of Oligomeric Genes. Biomacromolecules 2010, 11 (4), 944–952. https://doi.org/10.1021/bm901387t.
(20) Rodríguez-Cabello, J. C.; Arias, F. J.; Rodrigo, M. A.; Girotti, A. Elastin-like Polypeptides in Drug Delivery. Adv. Drug Deliv. Rev. 2016, 97, 85–100. https://doi.org/10.1016/j.addr.2015.12.007.
(21) Kostal, J.; Mulchandani, A.; Chen, W. Tunable Biopolymers for Heavy Metal Removal. Macromolecules 2001, 34 (7), 2257–2261. https://doi.org/10.1021/ma001973m.
(22) Mullerpatan, A.; Chandra, D.; Kane, E.; Karande, P.; Cramer, S. Purification of Proteins Using Peptide-ELP Based Affinity Precipitation. J. Biotechnol. 2020, 309, 59–67. https://doi.org/10.1016/j.jbiotec.2019.12.012.
(23) Nettles, D. L.; Chilkoti, A.; Setton, L. A. Applications of Elastin-like Polypeptides in Tissue Engineering. Adv. Drug Deliv. Rev. 2010, 62 (15), 1479–1485. https://doi.org/10.1016/j.addr.2010.04.002.
(24) Shao, L.; Ma, J.; Prelesnik, J. L.; Zhou, Y.; Nguyen, M.; Zhao, M.; Jenekhe, S. A.; Kalinin, S. V.; Ferguson, A. L.; Pfaendtner, J.; Mundy, C. J.; De Yoreo, J. J.; Baneyx, F.; Chen, C.-L. Hierarchical Materials from High Information Content Macromolecular Building Blocks: Construction, Dynamic Interventions, and Prediction. Chem. Rev. 2022, 122 (24), 17397–17478. https://doi.org/10.1021/acs.chemrev.2c00220.
(25) Rosenthal, S. J.; Chang, J. C.; Kovtun, O.; McBride, J. R.; Tomlinson, I. D. Biocompatible Quantum Dots for Biological Applications. Chem. Biol. 2011, 18 (1), 10–24. https://doi.org/10.1016/j.chembiol.2010.11.013.
(26) Fahmi, A.; Pietsch, T.; Bryszewska, M.; Rodríguez-Cabello, J. C.; Koceva-Chyla, A.; Arias, F. J.; Rodrigo, M. A.; Gindy, N. Fabrication of CdSe-Nanofibers with Potential for

Biomedical Applications. Adv. Funct. Mater. 2010, 20 (6), 1011–1018. https://doi.org/10.1002/adfm.200902013.
(27) Biswas, P.; Cella, L. N.; Kang, S. H.; Mulchandani, A.; Yates, M. V.; Chen, W. A Quantum-Dot Based Protein Module for in Vivo Monitoring of Protease Activity through Fluorescence Resonance Energy Transfer. Chem. Commun. 2011, 47 (18), 5259–5261. https://doi.org/10.1039/C1CC10648A.
(28) Cai, Y.; Naser, N. Y.; Ma, J.; Baneyx, F. Precision Loading and Delivery of Molecular Cargo by Size-Controlled Coacervation of Gold Nanoparticles Functionalized with Elastin-like Peptides. Biomacromolecules 2024, 25 (4), 2390–2398. https://doi.org/10.1021/acs.biomac.3c01312.
(29) Murray, C. B.; Norris, D. J.; Bawendi, M. G. Synthesis and Characterization of Nearly Monodisperse CdE (E = Sulfur, Selenium, Tellurium) Semiconductor Nanocrystallites. J. Am. Chem. Soc. 1993, 115 (19), 8706–8715. https://doi.org/10.1021/ja00072a025.
(30) Katari, J. E. B.; Colvin, V. L.; Alivisatos, A. P. X-Ray Photoelectron Spectroscopy of CdSe Nanocrystals with Applications to Studies of the Nanocrystal Surface. J. Phys. Chem. 1994, 98 (15), 4109–4117. https://doi.org/10.1021/j100066a034.
(31) Peng, Z. A.; Peng, X. Formation of High-Quality CdTe, CdSe, and CdS Nanocrystals Using CdO as Precursor. J. Am. Chem. Soc. 2001, 123 (1), 183–184. https://doi.org/10.1021/ja003633m.
(32) Choi, J. K.; Haynie, B. E.; Tohgha, U.; Pap, L.; Elliott, K. W.; Leonard, B. M.; Dzyuba, S. V.; Varga, K.; Kubelka, J.; Balaz, M. Chirality Inversion of CdSe and CdS Quantum Dots without Changing the Stereochemistry of the Capping Ligand. ACS Nano 2016, 10 (3), 3809–3815. https://doi.org/10.1021/acsnano.6b00567.
(33) Varga, K.; Tannir, S.; Haynie, B. E.; Leonard, B. M.; Dzyuba, S. V.; Kubelka, J.; Balaz, M. CdSe Quantum Dots Functionalized with Chiral, Thiol-Free Carboxylic Acids: Unraveling Structural Requirements for Ligand-Induced Chirality. ACS Nano 2017, 11 (10), 9846–9853. https://doi.org/10.1021/acsnano.7b03555.
(34) Puri, M.; Ferry, V. E. Circular Dichroism of CdSe Nanocrystals Bound by Chiral Carboxylic Acids. ACS Nano 2017, 11 (12), 12240–12246. https://doi.org/10.1021/acsnano.7b05690.
(35) Joh, Y. A.; Kwon, Y. H.; Tannir, S.; Leonard, B. M.; Kubelka, J.; Varga, K.; Balaz, M. The Effect of Molecular Isomerism on the Induced Circular Dichroism of Cadmium Sulfide Quantum Dots. J. Mater. Chem. C 2021, 9 (48), 17483–17495. https://doi.org/10.1039/D1TC04496F.
(36) Kwon, Y. H.; Joh, Y. A.; Leonard, B. M.; Balaz, M.; Varga, K. Threonine Functionalized Colloidal Cadmium Sulfide (CdS) Quantum Dots: The Role of Solvent and Counterion in Ligand Induced Chiroptical Properties. J. Colloid Interface Sci. 2023, 642, 771–778. https://doi.org/10.1016/j.jcis.2023.03.177.
(37) Baldwin, R. L. How Hofmeister Ion Interactions Affect Protein Stability. Biophys. J. 1996, 71 (4), 2056–2063. https://doi.org/10.1016/S0006-3495(96)79404-3.
(38) Kunz, W.; Henle, J.; Ninham, B. W. 'Zur Lehre von Der Wirkung Der Salze' (about the Science of the Effect of Salts): Franz Hofmeister's Historical Papers. Curr. Opin. Colloid Interface Sci. 2004, 9 (1), 19–37. https://doi.org/10.1016/j.cocis.2004.05.005.
(39) Ma, L.; Tu, C.; Le, P.; Chitoor, S.; Lim, S. J.; Zahid, M. U.; Teng, K. W.; Ge, P.; Selvin, P. R.; Smith, A. M. Multidentate Polymer Coatings for Compact and Homogeneous

Quantum Dots with Efficient Bioconjugation. J. Am. Chem. Soc. 2016, 138 (10), 3382–3394. https://doi.org/10.1021/jacs.5b12378.
(40) Zhang, H.; Chen, J.; Xiao, C.; Tao, Y.; Wang, X. A Multifunctional Polypeptide via Ugi Reaction for Compact and Biocompatible Quantum Dots with Efficient Bioconjugation. Bioconjug. Chem. 2018, 29 (4), 1335–1343. https://doi.org/10.1021/acs.bioconjchem.8b00072.
(41) Susumu, K.; Oh, E.; Delehanty, J. B.; Pinaud, F.; Gemmill, K. B.; Walper, S.; Breger, J.; Schroeder, M. J.; Stewart, M. H.; Jain, V.; Whitaker, C. M.; Huston, A. L.; Medintz, I. L. A New Family of Pyridine-Appended Multidentate Polymers As Hydrophilic Surface Ligands for Preparing Stable Biocompatible Quantum Dots. Chem. Mater. 2014, 26 (18), 5327–5344. https://doi.org/10.1021/cm502386f.
(42) Jin, Z.; Dridi, N.; Palui, G.; Palomo, V.; Jokerst, J. V.; Dawson, P. E.; Sang, Q.-X. A.; Mattoussi, H. Quantum Dot–Peptide Conjugates as Energy Transfer Probes for Sensing the Proteolytic Activity of Matrix Metalloproteinase-14. Anal. Chem. 2023, 95 (5), 2713–2722. https://doi.org/10.1021/acs.analchem.2c03400.
(43) Danehy, J. P.; Noel, C. J. The Relative Nucleophilic Character of Several Mercaptans toward Ethylene Oxide1. J. Am. Chem. Soc. 1960, 82 (10), 2511–2515. https://doi.org/10.1021/ja01495a028.
(44) Kuznetsova, V. A.; Mates-Torres, E.; Prochukhan, N.; Marcastel, M.; Purcell-Milton, F.; O'Brien, J.; Visheratina, A. K.; Martinez-Carmona, M.; Gromova, Y.; Garcia-Melchor, M.; Gun'ko, Y. K. Effect of Chiral Ligand Concentration and Binding Mode on Chiroptical Activity of CdSe/CdS Quantum Dots. ACS Nano 2019, 13 (11), 13560–13572. https://doi.org/10.1021/acsnano.9b07513.
(45) Kurihara, T.; Noda, Y.; Takegoshi, K. Capping Structure of Ligand–Cysteine on CdSe Magic-Sized Clusters. ACS Omega 2019, 4 (2), 3476–3483. https://doi.org/10.1021/acsomega.8b02752.
(46) Fazary, A. E.; Awwad, N. S.; Ibrahium, H. A.; Shati, A. A.; Alfaifi, M. Y.; Ju, Y.-H. Protonation Equilibria of N-Acetylcysteine. ACS Omega 2020, 5 (31), 19598–19605. https://doi.org/10.1021/acsomega.0c02080.
(47) Jalilehvand, F.; Amini, Z.; Parmar, K.; Kang, E. Y. Cadmium(II) N-Acetylcysteine Complex Formation in Aqueous Solution. Dalton Trans. 2011, 40 (47), 12771–12778. https://doi.org/10.1039/C1DT11705J.
(48) Anderson, N. C.; Hendricks, M. P.; Choi, J. J.; Owen, J. S. Ligand Exchange and the Stoichiometry of Metal Chalcogenide Nanocrystals: Spectroscopic Observation of Facile Metal-Carboxylate Displacement and Binding. J. Am. Chem. Soc. 2013, 135 (49), 18536–18548. https://doi.org/10.1021/ja4086758.
(49) Ma, Q.; Liu, L.; Yang, Z.; Zheng, P. Facile Synthesis of Peptide-Conjugated Gold Nanoclusters with Different Lengths. Nanomaterials 2021, 11 (11), 2932. https://doi.org/10.3390/nano11112932.
(50) Lin, Y.; Xia, X.; Wang, M.; Wang, Q.; An, B.; Tao, H.; Xu, Q.; Omenetto, F.; Kaplan, D. L. Genetically Programmable Thermoresponsive Plasmonic Gold/Silk-Elastin Protein Core/Shell Nanoparticles. Langmuir 2014, 30 (15), 4406–4414. https://doi.org/10.1021/la403559t.
(51) Nath, N.; Chilkoti, A. Interfacial Phase Transition of an Environmentally Responsive Elastin Biopolymer Adsorbed on Functionalized Gold Nanoparticles Studied by Colloidal

Surface Plasmon Resonance. J. Am. Chem. Soc. 2001, 123 (34), 8197–8202. https://doi.org/10.1021/ja015585r.
(52) Alvarez-Rodriguez, R.; Alonso, M.; Girotti, A.; Reboto, V.; Rodriguez-Cabello, J. C. One-Pot Synthesis of pH and Temperature Sensitive Gold Clusters Mediated by a Recombinant Elastin-like Polymer. Eur. Polym. J. 2010, 46 (4), 643–650. https://doi.org/10.1016/j.eurpolymj.2009.12.022.
(53) Huang, H.-C.; Koria, P.; Parker, S. M.; Selby, L.; Megeed, Z.; Rege, K. Optically Responsive Gold Nanorod−Polypeptide Assemblies. Langmuir 2008, 24 (24), 14139–14144. https://doi.org/10.1021/la802842k.
(54) Zong, J.; Cobb, S. L.; Cameron, N. R. Short Elastin-like Peptide-Functionalized Gold Nanoparticles That Are Temperature Responsive under near-Physiological Conditions. J. Mater. Chem. B 2018, 6 (41), 6667–6674. https://doi.org/10.1039/C8TB01827H.
(55) Higashi, N.; Ochiai, T.; Kanazawa, C.; Koga, T. Site-Specific Adsorption of Gold Nanoparticles Coated with Thermo-Responsive Peptides. Polym. J. 2013, 45 (5), 523–528. https://doi.org/10.1038/pj.2012.220.
(56) Fabrication of CdSe-Nanofibers with Potential for Biomedical Applications - Fahmi - 2010 - Advanced Functional Materials - Wiley Online Library. https://onlinelibrary.wiley.com/doi/full/10.1002/adfm.200902013 (accessed 2024-05-24).
(57) Qian, Z.; Guye, K. N.; Masiello, D. J.; Ginger, D. S. Dynamic Optical Switching of Polymer/Plasmonic Nanoparticle Hybrids with Sparse Loading. J. Phys. Chem. B 2017, 121 (5), 1092–1099. https://doi.org/10.1021/acs.jpcb.7b00013.
(58) Ding, T.; Valev, V. K.; Salmon, A. R.; Forman, C. J.; Smoukov, S. K.; Scherman, O. A.; Frenkel, D.; Baumberg, J. J. Light-Induced Actuating Nanotransducers. Proc. Natl. Acad. Sci. 2016, 113 (20), 5503–5507. https://doi.org/10.1073/pnas.1524209113.
(59) Sumiyoshi, S.; Suyama, K.; Tanaka, N.; Andoh, T.; Nagata, A.; Tomohara, K.; Taniguchi, S.; Maeda, I.; Nose, T. Development of Truncated Elastin-like Peptide Analogues with Improved Temperature-Response and Self-Assembling Properties. Sci. Rep. 2022, 12 (1), 19414. https://doi.org/10.1038/s41598-022-23940-0.
(60) Brahms, S.; Brahms, J.; Spach, G.; Brack, A. Identification of Beta,Beta-Turns and Unordered Conformations in Polypeptide Chains by Vacuum Ultraviolet Circular Dichroism. Proc. Natl. Acad. Sci. U. S. A. 1977, 74 (8), 3208–3212. https://doi.org/10.1073/pnas.74.8.3208.
(61) Urry, D. W. Physical Chemistry of Biological Free Energy Transduction As Demonstrated by Elastic Protein-Based Polymers. J. Phys. Chem. B 1997, 101 (51), 11007–11028. https://doi.org/10.1021/jp972167t.
(62) Rice, S. A. Small Angle Scattering of X-Rays. A. Guinier and G. Fournet. Translated by C. B. Wilson and with a Bibliographical Appendix by K. L. Yudowitch. Wiley, New York, 1955. 268 Pp. J. Polym. Sci. 1956, 19 (93), 594–594. https://doi.org/10.1002/pol.1956.120199326.
(63) Bahniuk, M. S.; Alshememry, A. K.; Elgersma, S. V.; Unsworth, L. D. Self-Assembly/Disassembly Hysteresis of Nanoparticles Composed of Marginally Soluble, Short Elastin-like Polypeptides. J. Nanobiotechnology 2018, 16 (1), 15. https://doi.org/10.1186/s12951-018-0342-5.
(64) Hamachi, L. S.; Yang, H.; Plante, I. J.-L.; Saenz, N.; Qian, K.; Campos, M. P.; Cleveland, G. T.; Rreza, I.; Oza, A.; Walravens, W.; Chan, E. M.; Hens, Z.; Crowther, A. C.; Owen, J. S. Precursor Reaction Kinetics Control Compositional Grading and Size of

CdSe1−xSx Nanocrystal Heterostructures. Chem. Sci. 2019, 10 (26), 6539–6552. https://doi.org/10.1039/C9SC00989B.
(65) Bressler, I.; Pauw, B. R.; Thünemann, A. F. McSAS: Software for the Retrieval of Model Parameter Distributions from Scattering Patterns. J. Appl. Crystallogr. 2015, 48 (3), 962–969. https://doi.org/10.1107/S1600576715007347.

Chapter 3. CHIRAL THIOL SENSING WITH ACHIRAL CDS NRS

3.1 INTRODUCTION

In biology, cysteine (Cys) has a far more diverse set of functional roles than any other amino acid. Cys is known to participate in structural disulfides, redox regulation, nucleophilic catalysis, and metal binding.[1] Despite its diverse roles, Cys is the least abundant amino acid in human proteins, accounting for around 2%.[2,3] For healthy adults, Cys concentration is typically between 240-360 μM,[4] with concentrations outside this range signaling cell aging[5] and neurodegenerative diseases.[6] Because cysteine is a biologically prevalent thiol with well-characterized nucleophilicity and redox chemistry, it is also a useful model for probing thiol reactivity under physiologically relevant conditions.

CdE (E=S, Se, Te) nanocrystals (NCs) offer synthetically tunable chromophores with surface-sensitive absorbance and emission profiles, making them promising candidates for sensing applications.[7,8] A common approach to synthesizing high-quality, water-soluble CdE NCs involves hydrophobic synthesis followed by aqueous-phase exchange. Reports utilize high-boiling-point solvents and long alkyl-chain ligands (containing carboxylate, amine, or phosphonate binding groups) to controllably synthesize CdE NCs. Once synthesized, the CdE NCs are often phase-exchanged using hydrophilic thiol-containing capping ligands, rendering the NCs water-soluble.[9–12] Thiol binding groups have been extensively used to phase exchange CdE NCs due to their thermodynamically superior interactions when compared to carboxylate and amine binding groups.[13]

Highlighting CdE NC surface sensitivity, recent studies showed that QDs exhibit chiroptical signatures when directly interfaced with chiral molecules, including Cys.[11,14] Since the discovery that replacing hydrophobic ligands with Cys on CdSe QDs resulted in the absorbance and emission features of the QD showing a chiral response in circular dichroism (CD) and circularly polarized luminescence experiments,[14] many studies have followed up to understand how shelling,[15] chiral molecule identity,[9,16] and NC morphology[17,18] affect induced NC chirality. Notably, nanorod (NR) morphologies have been reported to be up to 10 times more chiroptically active than QDs.[12] While the mechanism is still not fully understood, these reports have demonstrated that directly interfacing CdE NCs with chiral molecules induces chiroptical properties. Adding to this emerging field, we have recently demonstrated that Cys-containing polypeptides also induce chirality in CdS QDs.[19]

The concentration of Cys during CdE NC phase exchange has also been shown to affect the induced chiroptical properties. Kuznetzova et al.[10] and Cheng et al.[18] reported that the concentration of Cys used during the biphasic ligand exchange affects the chiroptical response of CdSe/CdS QDs and CdSe/CdS NRs, respectively. In these exchanges, Cys concentrations were at least 100 equivalents per QD and 10,000 equivalents per NR, respectively. Notably, for CdSe/CdS NRs, the highest g-factors were obtained with the smallest Cys concentration (10,000 eq/NR) that still allowed NR phase exchange.[18] These reports highlight the importance of ligand coverage required for phase exchange and dictating chiroptical response.

Despite these advances, the reliance on a very large excess of chiral thiols to induce measurable chiroptical signals limits their relevance to biologically meaningful concentrations and practical sensing applications. Because circular dichroism is directly sensitive to the chiral environment at the nanocrystal surface, it presents an attractive, label-free mechanism for thiol

detection if the induced signals can be observed at physiologically relevant concentrations. Here we test that hypothesis by titrating biologically relevant chiral thiols, including Cys, glutathione (GSH), n-acetyl-L-cysteine (NAC), and L-cysteine-methylester (CysME), intro achiral glycine-capped CdS nanorods and monitoring induced CD and PL responses, comparing nanorod lengths and thiol structures to evaluate sensitivity and selectivity. By demonstrating induced chiroptical responses at physiologically relevant μM thiol concentrations [4] and linking those responses to nanorod morphology and ligand structure, we aim to establish a surface-sensitive optical approach for detecting cysteine and related thiols in biologically relevant settings.

3.2 Results and Discussion

For this study, a seeded growth synthesis was adopted to produce 2 NRs with identical {001} and {101} polar facet dimensions while varying the non-polar {100} facets (see methods).[20] The as-synthesized NRs were analyzed by transmission electron microscopy (TEM), with sizing analysis revealing 6.0 ± 0.7 nm by 22 ± 6 nm (**Figure 3.1A**) and 5.8 ± 0.8 nm by 61 ± 29 nm (**Figure 3.1B**) for the short and long NRs, respectively. The CdS NRs are rendered water-soluble with glycine following a previously reported procedure from our group.[19] Following water solubilization, the NRs etch slightly, consistent with previous observations, leading to short and long NRs with dimensions of 4.9 ± 0.6 nm by 18 ± 5 nm (**Figure 3.1C**) and 5.0 ± 0.8 nm by 61 ± 29 nm, respectively (**Figure 3.1D**). While both the width dimensions decrease by approximately 1 nm, the length dimensions remain within error after the glycine ligand exchange. Most importantly, both NRs are water-soluble, and their UV-Vis, PL, and CD spectra can be monitored (**Figure 3.2**).

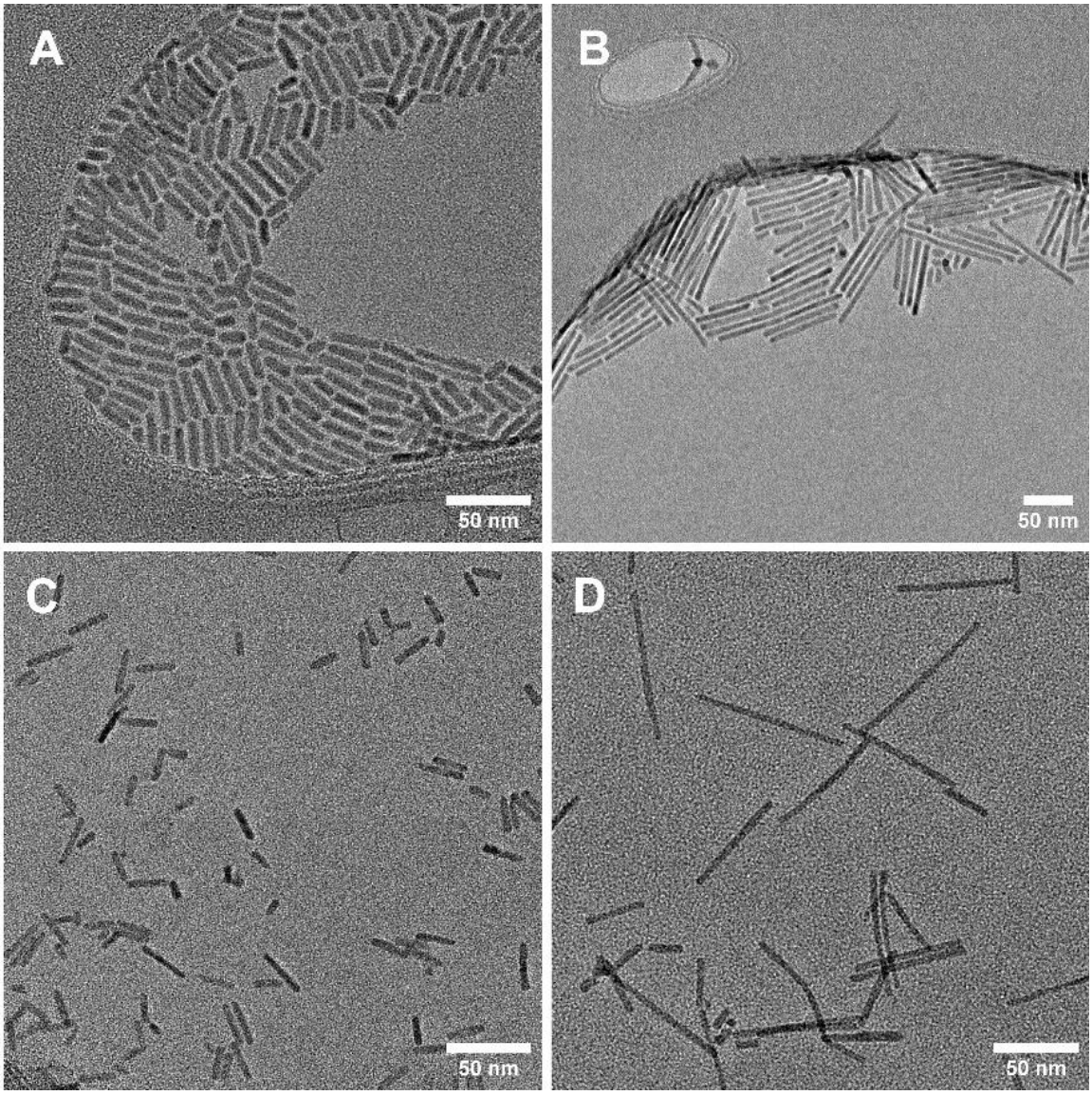

Figure 3.1 (A) TEM and sizing of shorter as-synthesized CdS NRs with an average width of 6.0 ± 0.7 nm and length of 22 ± 6 nm. (B) TEM and sizing of longer as-synthesized CdS NRs with an average width of 5.8 ± 0.8 nm and length of 65 ± 31 nm. (C) TEM and sizing of shorter glycine:CdS NRs after ligand exchange with an average width of 4.9 ± 0.6 nm and length of 18 ± 5 nm. (D) TEM and sizing of longer glycine:CdS NRs after ligand exchange with an average width of 5.0 ± 0.8 nm and length 61 ± 29 nm.

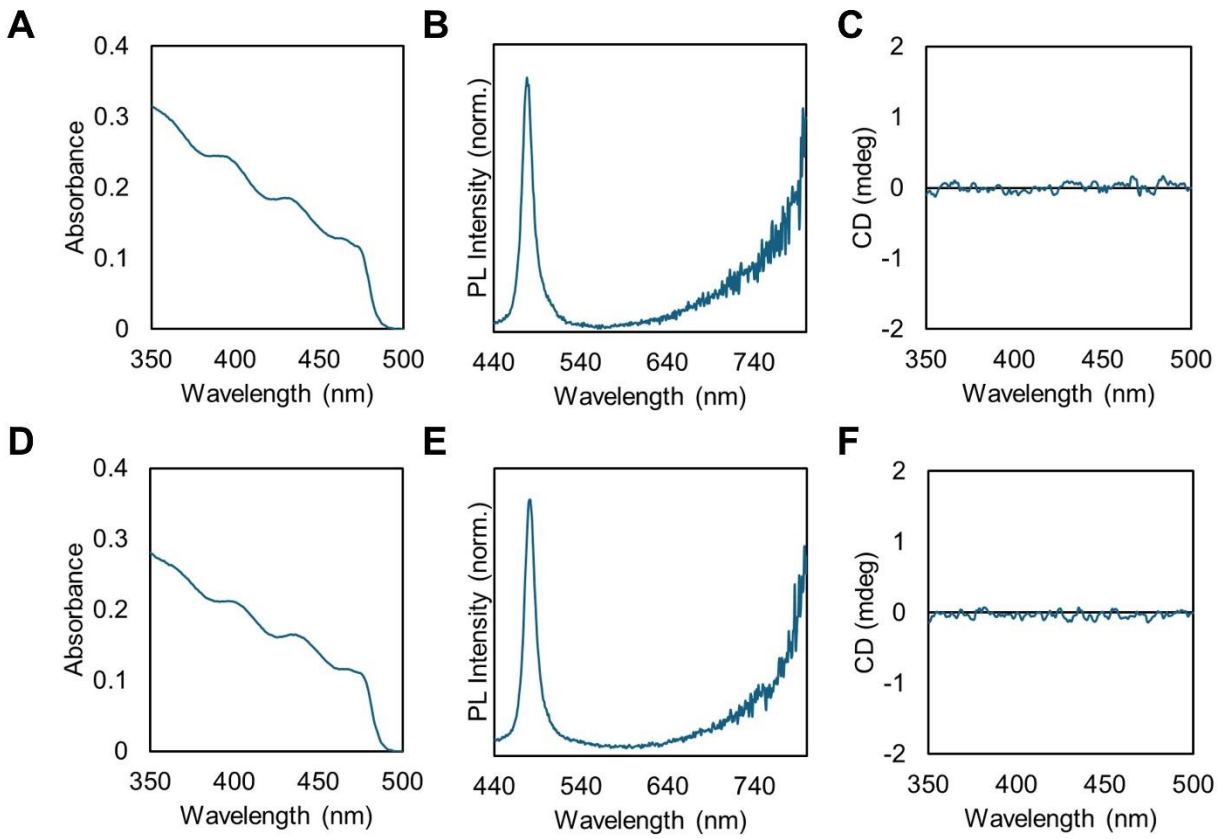

Figure 3.2 (A) UV-Vis spectrum of short glycine:CdS NRs. (B) PL spectrum of short glycine CdS NRs, excitation at 412 nm. (C) CD spectrum of short glycine CdS NRs. (D) UV-Vis spectrum of long glycine:CdS NRs. (E) PL spectrum of long glycine:CdS NR, excitation at 412 nm. (F) CD spectrum of long glycine:CdS NRs. All spectra were collected in water at pH 10.3.

Methods for quantifying biothiols have historically used organic transformations to attach fluorescent probes to the thiol group, each with inherent limitations.[21] In this work, we aim to leverage the optically sensitive surface of the NRs to probe chiral biothiol interactions. To mimic the potential interactions biothiols have on induced NR optical properties, we examine GSH (**Figure 3.3A-green**), Cys (**Figure 3.3A-black**), NAC (**Figure 3.3A-plum**), and CysME (**Figure**

3.3A-orange). GSH was selected to mimic the internal Cys protein coordination motif, while NAC and CysME were selected to mimic c and n-terminus Cys binding, respectively.

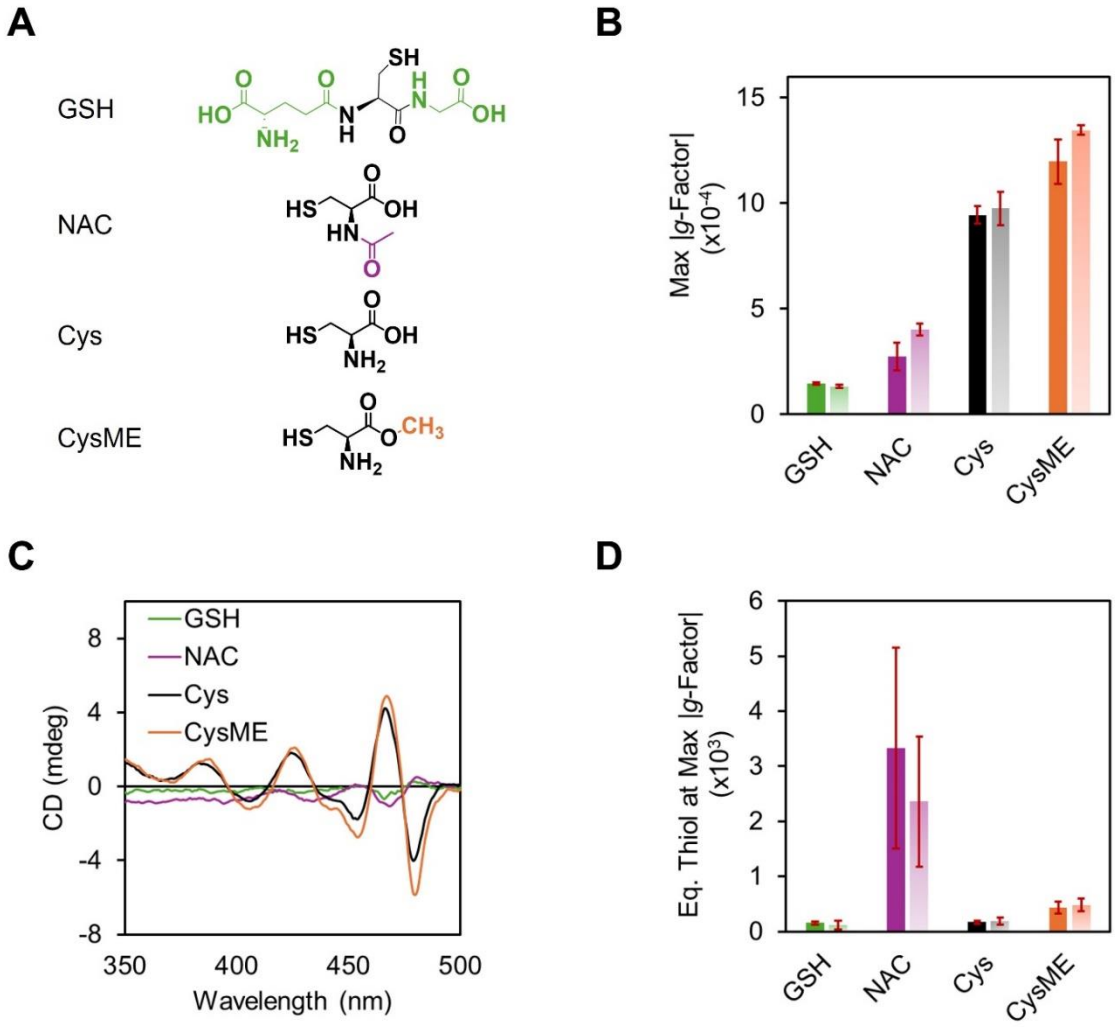

Figure 3.3 (A) Legend of chiral thiol molecules used: CysME (orange), Cys (black), NAC (plum), and GSH (green). (B) Maximum |*g*-factor| obtained for each NR (short-dark, long-faded) of GSH (green), NAC (plum), Cys (black) and CysME (orange) at pH 10.3. (C) Most intense CD spectra of long NRs with GSH (green), NAC (plum), Cys (black) and CysME (orange). (D) Average equivalents of GSH (green), NAC (plum), Cys (black) and CysME (orange) needed to obtain maximum *g*-factors. |*g*-factor| was calculated by taking the magnitude of the *g*-factor value at the

most intense CD transition. Starting concentrations: [Short CdS]: 86 nM, [Long CdS]: 77 nM, [TCEP]: 1 mM. All stock cysteine solutions were made at 20 mM in nanopure water.

To determine how Cys and its derivatives affect the induced optical properties, titrations were performed at pH 10.3 using the two different NR lengths (see Methods) and their maximum *g*-factors determined (**Figure 3.3B**). For short NRs, the *g*-factor of GSH, NAC, Cys, and CysME were $1.45(6)x10^{-4}$ (**Figure 3.3B-dark green**), $2.7(6)x10^{-4}$ (**Figure 3.3B-dark plum**), $9.4(4)x10^{-4}$ (**Figure 3.3B- black**), and $12.0(1)x10^{-4}$ (**Figure 3.3B-dark orange**), respectively. Comparing the long NRs, the *g*-Factor of GSH, NAC, Cys, and CysME were $1.33(9)x10^{-4}$ (**Figure 3.3B- light green**), $4.0(3)x10^{-4}$ (**Figure 3.3B-light plum**), $9.8(8)x10^{-4}$ (**Figure 3.3B-gray**), and $13.2(2)x10^{-4}$ (**Figure 3.3B-light orange**), respectively. Notably, for both NRs, CysME produces the highest *g*-factors, followed by Cys, NAC, and GSH, respectively. From these results, we hypothesize that the carboxylate binding groups do not significantly impact chiroptical activity, whereas acetylation of the adjacent amine group drastically decreases achievable *g*-factors. Interestingly, CysME resulted in lower *g*-factors than Cys and NAC,[9] with seldom reports of ligand exchanges with GSH. Additionally, these results demonstrate that the stoichiometric {100} facet does not significantly impact the induced chiral optical properties. This result is consistent with the results previously reported for CdSe NRs [12] and suggests the polar facet dimensions primarily dictate the chiroptical outcome with NRs.

As previously reported for QDs, a prominent factor in dictating induced chirality is the number of ligands bound to the surface.[10] We hypothesize that the steric bulk of GSH and NAC results in fewer thiol groups bound and modest *g*-factors compared to Cys and CysME. These results suggest that acetylation of the amine bound to the chiral carbon center in Cys has a significant impact in reducing the induced chirality in NRs, while methylation of the carboxyl

group does not. Overall, we propose that the number of ligands bound to the polar facets affects the induced chiroptical properties observed in NRs.

While GSH and NAC have modest *g*-factors, their CD line shapes are also inverted relative to Cys and CysME (**FIGURE 3.3C**), consistent with previous observations in QDs.[9,19] As previously hypothesized by Choi et al., NAC inverted chirality is believed to arise from L-type ligand passivation by the amide carbonyl, which could explain the CD inversion of both NAC and GSH relative to Cys and CysME.[9] Additionally, there is a large difference in the NAC concentration required to reach the maximum *g*-factor value compared to that of the other Cys derivatives (**Figure 3.3D**). Surprisingly, this was not true of GSH, which also has an acetylated amine on the adjacent carbon center. However, GSH contains an amine-binding group several atoms away from the thiol group, which could potentially explain these differences. Regardless, our results demonstrate that the presence of an amine group in the vicinity of the thiol influences the magnitude and lineshape of the chiroptical response. For short NRs, the equivalents of GSH, NAC, Cys, and CysME per NR at the maximum *g*-factor were 150(30) (**Figure 3.3D-dark green**), 3,000(1,000) (**Figure 3.3D-dark plum**), 170(30) (**Figure 3.3D-black**), and 400(100) (**Figure 3.3D-dark orange**), respectively. For Long NRs, the *g*-Factor of GSH, NAC, Cys, and CysME were 120(80) (**Figure 3.3D-light green**), 2,000(1,000) (**Figure 3.3D-light plum**), 190(60) (**Figure 3.3D-gray**), and 500(100) (**Figure 3.3D-light orange**), respectively. The lack of observed differences in thiol equivalents between the 2 length NRs also demonstrates that the non-polar 100 facet has no significant influence on induced chiroptical properties of NRs.

To further examine the role of ligand concentration on the induced chirality, equivalents of thiol per NR were plotted against *g*-factor for both short (**Figure 3.4A**) and long NRs (**Figure**

3.4B). Interestingly, we observed an increase followed by a notable drop-off in *g*-factor for CysME (**Figure 3.4A,B-orange**), Cys (**Figure 3.4A,B-black**), and GSH (**Figure 3.4A,B-orange**) regardless of NR length. These results are consistent with those of Gun'ko and coworkers, who found that the *g*-factor initially increased with increasing Cys concentration, then decreased.[10] The decrease in *g*-factor is proposed to be due to reduced denticity of Cys on the surface (as the concentration of Cys on the CdSe increases, Cys denticity decreases). Notably, the *g*-factor of NAC shows little to no chirality in the first few hundred equivalents (**Figure 3.4A,B-plum**), eventually reaching a maximum around 1000 equivalents. While it is still unclear why NAC behaves differently in these titrations compared to GSH, Cys, and CysME, this trend was observable in both NR sizes.

Finally, to corroborate the induced chiroptical data for the NRs, PL spectra were monitored during titrations of both short (**Figure 4C**) and long NRs (**Figure 4D**). These results demonstrate that as thiol concentration increases, band edge PL decreases, consistent with previous reports of thiols trapping charge carriers in NCs.[22] Comparing *g*-factor and band-edge PL trends across the different thiols, stronger chirality induction with thiols leads to greater quenching of band-edge PL. We hypothesize that the band edge PL is also a good proxy for the number of surface thiols. GSH has the greatest steric bulk and thus has the best preservation of band edge PL (**Figure XX, B-green**) of the NRs, and suggests that increasing steric bulk leads to fewer thiols on the surface of the NRs. As the steric profile is decreased in NAC, slightly less band edge PL quenching is observed (**Figure XX, B-plum**). Then moving to Cys (**Figure XX, B-black)** and CysME (**Figure XX, B-orange),** considerably more band edge PL quenching is observed, signifying more thiols are bound to the NR surface due to their considerably reduced steric bulk.

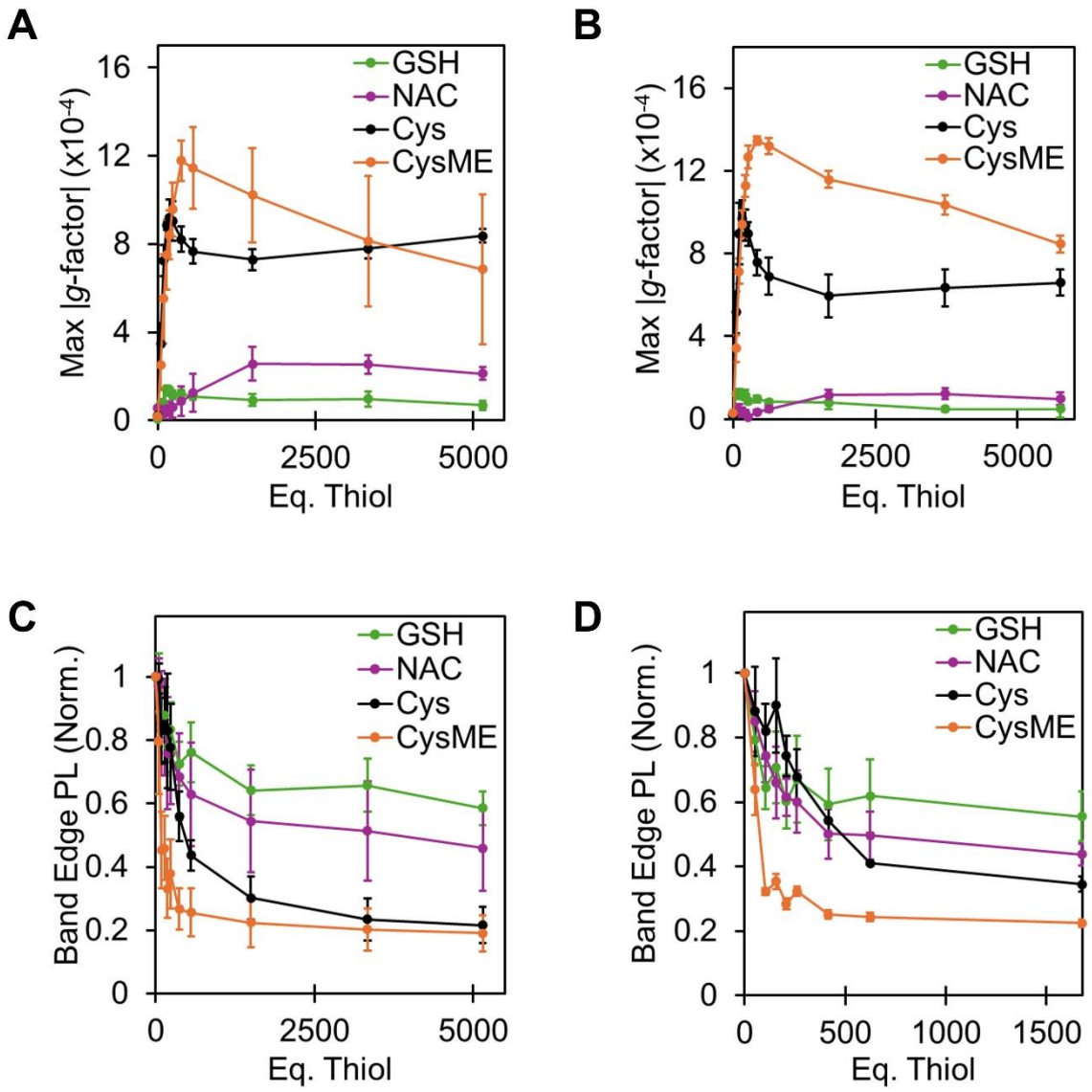

Figure 3.4 (A) Plot of short CdS NR *g*-factor vs. equivalents of GSH (green), NAC (plum), Cys (black) and CysME (orange). (B) Plot of normalized band edge emission of short CdS NR vs. equivalents of GSH (green), NAC (plum), Cys (black), and CysME (orange).

3.3 CONCLUSIONS

In summary, we have described μM sensing of chiral thiols using two different length achiral water-soluble CdS NRs using a combination of CD and PL. From our results, we found that maximum *g*-factors were achievable for CdS NRs at ~100 equivalents for GSH, Cys, and

CysME, demonstrating that significant induced chiroptical activity can occur at far lower ligand concentration than previously reported. Among the thiols tested, CysME produced the largest *g*-factor for both short and long CdS NRs ($12.0(1)x10^{-4}$ and $13.2(2)x10^{-4}$, respectively), and the NR length was not found to significantly influence *g*-factor. GSH and NAC produced inverted CD lineshapes compared with Cys and NAC, highlighting the influence of the local coordination motif of the thiols. Collectively, these results highlight the exceptional surface sensitivity of CdS NRs to biologically relevant concentrations of thiols and emphasize the importance of ligand coverage and concentration in dictating chiroptical response in these materials.

3.4 Experimental Methods

3.4.1 *Materials*

The following chemicals were used without purification. Cadmium oxide powder (CdO, 99.95%), sulfur powder (99.95%), trioctylphosphine (TOP, 90%). Tetramethylammonium hydroxide solution (TMAOH, 10% wt in water), glycine (98%), L-cysteine (Cys, 97%), L-cysteine methyl ester (CysME, ≥98%), n-acetyl-L-cysteine (NAC, ≥99%), glutathione (GSH, 98%), tris(2-carboxyethyl)phosphine hydrochloride powder (TCEP•HCl, ≥98%), methanol (≥99.9%), and toluene (≥99.8%) were purchased from MilliporeSigma. n-tetradecylphosphonic acid (TDPA, 99%) was purchased from PCI Synthesis. Trioctylphosphine oxide (TOPO) (90%) was purchased from MilliporeSigma and recrystallized following a literature procedure.[23] 18.2 MΩ water was collected from an EMD Millipore purification system. UV−vis spectra were collected on a Cary 60 spectrophotometer from Agilent. Photoluminescence spectra were collected on a Horiba Scientific FluoroMax-4 spectrofluorometer. CD spectra were collected on a Jasco J-1500 (Scan rate: 100 nm/min, data pitch 1 nm, 15 scans, path length: 1 cm).

3.4.2 *Synthesis of Shorter CdS NRs*

Synthesis of the shorter CdS NRs was adapted from the literature.[20] The day before the synthesis, sulfur (0.045 g, 1.4 mM) was prepared in TOP (5 mL) in a glovebox. In a dried 50 mL 3-neck flask, CdO (0.0575 g, 0.45 mM), TOPO (1.75 g, 4.5 mM), and TDPA (0.2075 g, 0.75 mM) were degassed at 90 °C for 90 minutes. After 90 minutes, under nitrogen, the flask was heated to 340 °C for 10 minutes. After 10 minutes, the temperature was set to 300 °C and equilibrated. Once equilibrated, 1.5 mL of the previously prepared TOP-S solution was rapidly injected into the 3-neck flask, and the solution was left to re-equilibrate at 300 °C. This solution was left at 300 °C for 90 minutes. After 90 minutes, a 5 mL syringe was loaded with the remaining TOP-S solution and injected at a rate of 2.5 mL/hr while keeping the temperature at 300 °C. After the syringe injection was finished (~60 minutes), the NRs were left at 300 °C for an additional 20 minutes. The solution was then quickly removed from heat and rapidly cooled with air. Once the temperature reached 70 °C, 5 mL of toluene was rapidly injected. Next, the reaction was transferred to centrifuge tubes in a 3:1 MeOH:TOPO/toluene ratio and centrifuged at 10,000 RPM for 10 minutes. The resulting pellet was resuspended in minimal toluene, and MeOH was added to achieve a 3:1 MeOH:toluene ratio, then centrifuged at 10,000 RPM for 10 minutes for 2 additional cycles. Finally, the pellet was dissolved in 3x10 mL toluene, sonicated for 10 minutes, and centrifuged at 10,000 RPM for 10 mins. The resulting pellet was minimally soluble in toluene and analyzed via TEM and PXRD.

3.4.3 *Synthesis of Longer CdS NRs*

Synthesis of the longer CdS NRs was similarly adapted from literature.[20] The day before the synthesis, sulfur (0.045 g, 1.4 mM) was prepared in TOP (5 mL) in a glovebox. In a dried 50

mL 3-neck flask, CdO (0.0575 g, 0.45 mM), TOPO (1.75 g, 4.5 mM), and TDPA (0.2075 g, 0.75 mM) were degassed at 90 °C for 90 minutes. After 90 minutes, under nitrogen, the flask was heated to 340 °C for 10 minutes. After 10 minutes, the temperature was set to 300 °C and equilibrated. Once equilibrated, 1.5 mL of the previously prepared TOP-S solution was rapidly injected into the 3-neck flask, and the solution was left to re-equilibrate at 300 °C. This solution was left at 300 °C for 90 minutes. After 90 minutes, a 5 mL syringe was loaded with 1.6 mL of the TOP-S solution and injected at a rate of 2.5 mL/hr while keeping the temperature at 300 °C. After the syringe injection was finished (~30 minutes), the NRs were left at 300 °C for an additional 20 minutes. The solution was then quickly removed from heat and rapidly cooled with air. Once the temperature reached 70 °C, 5 mL of toluene was rapidly injected. Next, the reaction was transferred to centrifuge tubes in a 3:1 MeOH:TOPO/toluene ratio and centrifuged at 10,000 RPM for 10 minutes. The resulting pellet was then resuspended in minimal toluene, and MeOH was added to achieve a 3:1 MeOH:toluene ratio and centrifuged at 10,000 RPM for 10 minutes for 2 additional cycles. Finally, the pellet was dissolved in 3x10 mL toluene, sonicated for 10 minutes, and centrifuged at 10,000 RPM for 10 mins.

3.4.4 *CdS NR Glycine Exchange Procedure*

Both long and short CdS NRs were made water soluble with glycine by adapting our previous literature report.[19] In short, 5-7 mg of CdS NRs were transferred into a new vial and dried. To this vial, 6 mL of 1.78 M glycine in 1 M TMAOH were added, and the solution was stirred overnight in the dark. To this solution, 6 mL of toluene was added, and stirred, followed by centrifugation at 8,000 RPM for 10 minutes, producing a colorless top layer and a yellow bottom layer with white foam separating the layers. This toluene washing process was repeated

for 3 total cycles. The aqueous layer was then transferred to a vial and allowed to sit at 4 °C in the dark for 48 hours. After 48 hours, the solution was centrifuged at 8,000 RPM for 10 minutes, and the resulting solution was stored in air at room temperature and in the dark. The concentration of the glycine:CdS NR solutions was determined via the Peng sizing curve and was typically ~1 μM.[24] Determination of the lowest energy exciton was done by using the CD absorbance bisignate feature for both NRs produced in the addition of Cys.

3.4.5 *Glycine:CdS NR Spectroscopic Titration Procedure*

All thiol and TCEP solutions were freshly prepared before each titration. The starting volume for each titration was 2.5 mL. To prepare, 0.206 M TCEP•HCl was freshly prepared and 12.1 μL was added to 2.288 mL of nanopure water in a 3 mL cuvette. Next, the CdS NR solution was added to the cuvette so that the [Short CdS NRs]: 86 nM and [Long CdS]: 77 nM (typically ~150 μL of each stock solution), followed by dilution to 2.5 mL total volume with a prepared 1.78 M glycine and 1 M TMAOH aqueous solution. The thiols were freshly weighed out and dissolved in 2 mL of nanopure water, so the thiol stock concentration was 0.020 M. UV-Vis absorbance, CD, and PL spectrum were then collected after each addition of stock thiol solution at: 0 μL, 0.5 μL, 1 μL, 1.5 μL, 2 μL, 2.5 μL, 4 μL, 6 μL, 16 μL, 36 μL and 56 μL.

3.5 REFERENCES

(1) Pace, N. J.; Weerapana, E. Diverse Functional Roles of Reactive Cysteines. ACS Chem. Biol. 2013, 8 (2), 283–296. https://doi.org/10.1021/cb3005269.

(2) Eitner, K.; Koch, U.; Gawęda, T.; Marciniak, J. Statistical Distribution of Amino Acid Sequences: A Proof of Darwinian Evolution. Bioinformatics 2010, 26 (23), 2933–2935. https://doi.org/10.1093/bioinformatics/btq571.

(3) Desai, M.; Sun, B. Positions of Cysteine Residues Reveal Local Clusters and Hidden Relationships to Sequons and Transmembrane Domains in Human Proteins. Sci Rep 2024, 14 (1), 25886. https://doi.org/10.1038/s41598-024-77056-8.
(4) Wang, N.; Chen, M.; Gao, J.; Ji, X.; He, J.; Zhang, J.; Zhao, W. A Series of BODIPY-Based Probes for the Detection of Cysteine and Homocysteine in Living Cells. Talanta 2019, 195, 281–289. https://doi.org/10.1016/j.talanta.2018.11.066.
(5) Hughes, C. E.; Coody, T. K.; Jeong, M.-Y.; Berg, J. A.; Winge, D. R.; Hughes, A. L. Cysteine Toxicity Drives Age-Related Mitochondrial Decline by Altering Iron Homeostasis. Cell 2020, 180 (2), 296-310.e18. https://doi.org/10.1016/j.cell.2019.12.035.
(6) Paul, B. D.; Sbodio, J. I.; Snyder, S. H. Cysteine Metabolism in Neuronal Redox Homeostasis. Trends in Pharmacological Sciences 2018, 39 (5), 513–524. https://doi.org/10.1016/j.tips.2018.02.007.
(7) Morales-Narváez, E.; Montón, H.; Fomicheva, A.; Merkoçi, A. Signal Enhancement in Antibody Microarrays Using Quantum Dots Nanocrystals: Application to Potential Alzheimer's Disease Biomarker Screening. Anal. Chem. 2012, 84 (15), 6821–6827. https://doi.org/10.1021/ac301369e.
(8) Quesada-González, D.; Merkoçi, A. Quantum Dots for Biosensing: Classification and Applications. Biosensors and Bioelectronics 2025, 273, 117180. https://doi.org/10.1016/j.bios.2025.117180.
(9) Choi, J. K.; Haynie, B. E.; Tohgha, U.; Pap, L.; Elliott, K. W.; Leonard, B. M.; Dzyuba, S. V.; Varga, K.; Kubelka, J.; Balaz, M. Chirality Inversion of CdSe and CdS Quantum Dots without Changing the Stereochemistry of the Capping Ligand. ACS Nano 2016, 10 (3), 3809–3815. https://doi.org/10.1021/acsnano.6b00567.
(10) Kuznetsova, V. A.; Mates-Torres, E.; Prochukhan, N.; Marcastel, M.; Purcell-Milton, F.; O'Brien, J.; Visheratina, A. K.; Martinez-Carmona, M.; Gromova, Y.; Garcia-Melchor, M.; Gun'ko, Y. K. Effect of Chiral Ligand Concentration and Binding Mode on Chiroptical Activity of CdSe/CdS Quantum Dots. ACS Nano 2019, 13 (11), 13560–13572. https://doi.org/10.1021/acsnano.9b07513.
(11) Tohgha, U.; Varga, K.; Balaz, M. Achiral CdSe Quantum Dots Exhibit Optical Activity in the Visible Region upon Post-Synthetic Ligand Exchange with D- or L-Cysteine. Chem. Commun. 2013, 49 (18), 1844–1846. https://doi.org/10.1039/C3CC37987F.
(12) Gao, X.; Zhang, X.; Deng, K.; Han, B.; Zhao, L.; Wu, M.; Shi, L.; Lv, J.; Tang, Z. Excitonic Circular Dichroism of Chiral Quantum Rods. J. Am. Chem. Soc. 2017, 139 (25), 8734–8739. https://doi.org/10.1021/jacs.7b04224.
(13) Knauf, R. R.; Lennox, J. C.; Dempsey, J. L. Quantifying Ligand Exchange Reactions at CdSe Nanocrystal Surfaces. Chem. Mater. 2016, 28 (13), 4762–4770. https://doi.org/10.1021/acs.chemmater.6b01827.
(14) Tohgha, U.; Deol, K. K.; Porter, A. G.; Bartko, S. G.; Choi, J. K.; Leonard, B. M.; Varga, K.; Kubelka, J.; Muller, G.; Balaz, M. Ligand Induced Circular Dichroism and Circularly Polarized Luminescence in CdSe Quantum Dots. ACS Nano 2013, 7 (12), 11094–11102. https://doi.org/10.1021/nn404832f.
(15) Purcell-Milton, F.; Visheratina, A. K.; Kuznetsova, V. A.; Ryan, A.; Orlova, A. O.; Gun'ko, Y. K. Impact of Shell Thickness on Photoluminescence and Optical Activity in Chiral CdSe/CdS Core/Shell Quantum Dots. ACS Nano 2017, 11 (9), 9207–9214. https://doi.org/10.1021/acsnano.7b04199.

(16) Varga, K.; Tannir, S.; Haynie, B. E.; Leonard, B. M.; Dzyuba, S. V.; Kubelka, J.; Balaz, M. CdSe Quantum Dots Functionalized with Chiral, Thiol-Free Carboxylic Acids: Unraveling Structural Requirements for Ligand-Induced Chirality. ACS Nano 2017, 11 (10), 9846–9853. https://doi.org/10.1021/acsnano.7b03555.
(17) Hao, J.; Li, Y.; Miao, J.; Liu, R.; Li, J.; Liu, H.; Wang, Q.; Liu, H.; Delville, M.-H.; He, T.; Wang, K.; Zhu, X.; Cheng, J. Ligand-Induced Chirality in Asymmetric CdSe/CdS Nanostructures: A Close Look at Chiral Tadpoles. ACS Nano 2020, 14 (8), 10346–10358. https://doi.org/10.1021/acsnano.0c03909.
(18) Cheng, J.; Hao, J.; Liu, H.; Li, J.; Li, J.; Zhu, X.; Lin, X.; Wang, K.; He, T. Optically Active CdSe-Dot/CdS-Rod Nanocrystals with Induced Chirality and Circularly Polarized Luminescence. ACS Nano 2018, 12 (6), 5341–5350. https://doi.org/10.1021/acsnano.8b00112.
(19) Lowe, C. D.; Larson, H. C.; Cai, Y.; Chiang, H. T.; Pozzo, L. D.; Baneyx, F.; Cossairt, B. M. Induced Chirality in QDs Using Thermoresponsive Elastin-like Polypeptides. Langmuir 2025, 41 (1), 1047–1056. https://doi.org/10.1021/acs.langmuir.4c04339.
(20) Saunders, A. E.; Ghezelbash, A.; Sood, P.; Korgel, B. A. Synthesis of High Aspect Ratio Quantum-Size CdS Nanorods and Their Surface-Dependent Photoluminescence. Langmuir 2008, 24 (16), 9043–9049. https://doi.org/10.1021/la800964s.
(21) Wang, W.; Rusin, O.; Xu, X.; Kim, K. K.; Escobedo, J. O.; Fakayode, S. O.; Fletcher, K. A.; Lowry, M.; Schowalter, C. M.; Lawrence, C. M.; Fronczek, F. R.; Warner, I. M.; Strongin, R. M. Detection of Homocysteine and Cysteine. J. Am. Chem. Soc. 2005, 127 (45), 15949–15958. https://doi.org/10.1021/ja054962n.
(22) Hässelbarth, A.; Eychmüller, A.; Weller, H. Detection of Shallow Electron Traps in Quantum Sized CdS by Fluorescence Quenching Experiments. Chemical Physics Letters 1993, 203 (2), 271–276. https://doi.org/10.1016/0009-2614(93)85400-I.
(23) Wang, F.; Tang, R.; Buhro, W. E. The Trouble with TOPO; Identification of Adventitious Impurities Beneficial to the Growth of Cadmium Selenide Quantum Dots, Rods, and Wires. Nano Lett. 2008, 8 (10), 3521–3524. https://doi.org/10.1021/nl801692g.
(24) Yu, W. W.; Qu, L.; Guo, W.; Peng, X. Experimental Determination of the Extinction Coefficient of CdTe, CdSe, and CdS Nanocrystals. Chem. Mater. 2003, 15 (14), 2854–2860. https://doi.org/10.1021/cm034081k.

Chapter 4. NANOMOLAR SENSITIVITY CHIRALITY TRANSFER FROM DESIGNED HELICAL REPEAT PROTEINS TO ACHIRAL CDS NANORODS

4.1 INTRODUCTION

Chiral inorganic nanocrystals (NCs) are an emerging class of materials with potential applications in imaging, sensing, enantioselective catalysis, and spintronics.[1–5] Historically, Au NCs have been the most-studied material in this class, in which chiral molecules have been shown to induce asymmetry across several length scales. At the smallest scale, molecular asymmetry of the Au NC lattice can arise during the nucleation and growth stage using chiral ligands as stabilizers, resulting in *g*-factors as high as 10^{-1}.[6–8] At the length scale of the Au NC interface, asymmetry can emerge in achiral Au NCs via chiral molecule interactions on the NC surface.[9,10] Finally, macroscale architectures or assemblies can generate Au NCs in chiral configurations.[11–15]

While chiral Au NCs have been historically the most well-studied, chiral semiconducting NCs of CdE (E=S, Se, Te) have seen exceptional progress in the last 20 years. The first example of chirality in CdE NCs was reported in 2007 by Malony et.al., who used penicillamine as a ligand to synthesize aqueous CdS NCs.[16] While this report is fundamental in building our understanding of chiral NCs, ultimately controlling the morphology and optical properties of NCs in polar solvents has remained an outstanding challenge. Expanding on this observation of interfacial asymmetry, in 2013 Balaz and coworkers demonstrated that achiral, hydrophobic CdSe NCs could be made chiral via aqueous ligand exchange with cysteine (Cys), yielding *g*-

factors of 10^{-4}.[17,18] While the mechanism of interfacial chirality remains unclear, it has since been shown that this ligand exchange method can produce *g*-factors of up to 10^{-3} for CdE nanorods (NRs).[19] At the largest length scale, Kotov and coworkers have demonstrated micron-length helical assemblies of chiral CdTe NCs with *g*-factors of 10^{-2} using interfacial Cys.[20–22]

There are many examples of using chiral small molecules to create asymmetry in CdE across these length scales; however, there are far fewer studies that have incorporated proteins. Proteins offer chiral architectures comprised of chiral amino acid building blocks; however, much less is known about their ability to induce chirality in CdE NCs. Recently, Spangler and coworkers used designed proteins to template the growth of chiral CdS NCs; however, their *g*-factor was not reported.[23,24] In 2024, we reported the first example of inducing chirality in CdS quantum dots (QDs) using polypeptides with g-factors approaching 10^{-4}; however, the polypeptides lacked macromolecular order.[25] Chiral assemblies of CdE NCs with biomolecules (proteins, polypeptides, or DNA) are scarce.[14] This lack of examples highlights the difficulties of incorporating biomolecules that are highly sensitive to their environments (pH, temperature, ionic strength, etc.) and CdE NCs with charged surfaces that require passivation for colloidal stability.

Additionally, in the biomolecule:CdE examples, the systems are limited by accessible biomolecule concentration (10-450 μM),[14,23–25] likely due to synthetic and solubility limitations. In contrast, to the best of our knowledge, when performing biphasic aqueous ligand exchanges to achieve interfacial asymmetry in CdE NCs, the lowest concentration of Cys used is 1 mM[26] (typically 10-100 mM).[17–19,27–31] The large discrepancy in concentration and the high pH conditions used in these ligand exchanges are not feasible for incorporating biomolecules. While there are established methods for the direct covalent attachment of NCs to biomolecules, these

methods use small molecules on the NC surface to bind to targeted amino acids, with no reported chirality. An ideal system would exploit the protein's intrinsic chirality by enabling direct interfacial interactions between its amino acid side chains and the NC. To design such a direct bio-inorganic interface, achiral and water-soluble NCs are ideal.

To minimize biomolecule concentrations for observable chiroptical response, we aim to incorporate CdS NRs, as NRs have been shown to exhibit an order-of-magnitude increase in *g*-factor compared to QDs. Additionally, while we reported the first example of induced chirality in CdS QDs with polypeptides, the polypeptides used were intrinsically disordered with low complexity,[32] which made them ideal for simple surface chelation of CdS. To our knowledge, no prior report has demonstrated proteins with well-defined tertiary structure can transfer chirality to CdS NCs. Previous reports have been limited to small molecules, disordered polypeptides, or biomolecule templated growth, none of which address whether a folded protein can impose asymmetry at an inorganic interface. In this study, we aim to introduce complexity and order into biomolecules and determine whether establishing a protein:CdS interface induces asymmetry, and whether it does so while maintaining the protein structure. To do this, a designed helical repeat (DHR) protein containing eight α-helices and four Cys residues (DHR-4Cys) was prepared. Importantly, this protein is highly ordered and contains amino acids with additional chelating side chains, including aspartic acid (Asp), glutamic acid (Glu), histidine (His), and lysine (Lys), in addition to the four Cys residues. Moreover, all four Cys residues are located on one side of the protein's plate-like structure, which we hypothesized would be ideal for binding to the CdS surface with minimal interparticle aggregation. Such a CdS:DHR complex could be considered as a monomer in the deterministic construction of chiral structures across larger

length scales, given the precedent for the assembly of such designed proteins into macromolecular chiral motifs like helices.[33,34]

Here, we employ a robust aqueous ligand exchange method to directly establish a protein:CdS interface using NRs. To understand the role of CdS NR length on induced chirality, we synthesized two different NR lengths. Next, we used CD absorbance spectroscopy to probe interactions between CdS and DHR-4Cys by monitoring the NR electronic transitions. Additionally, we examined the protein structure on the CdS surface using far-UV CD absorbance spectroscopy and transmission electron microscopy (TEM), and measured the thermal stability of DHR-4Cys on the surface of CdS NRs with variable temperature CD absorbance. Finally, we tested the sensitivity of our exchange method using nanomolar concentrations of DHR-4Cys (~2.3 eq). For the first time, we report induced chirality in CdS NRs using a highly ordered DHR protein, with detection using CD down to the nanomolar concentration regime.

4.2 Results and Discussion

As previously mentioned, chiral CdSe NRs have been reported as more chiroptically active than chiral CdSe QDs.[31] This is proposed to be caused by a crossover of the highest occupied molecular orbitals (HOMO) from Se $4p_x$ and $4p_y$ frontier orbitals in NCs to Se $4p_z$ orbitals in NRs with aspect ratios greater than ~1.2.[35,36] This crossover results in an increase in linear polarization within CdSe NRs, which is hypothesized to couple strongly to molecular orbitals of chiral molecules on their surface.[31] Motivated by this previous report, we aim to test weather increasing the available surface area for DHR-4Cys to bind to CdS NRs would impact the induced optical properties. To do this, two different length CdS NRs were synthesized with

the same width dimensions in hydrophobic conditions, adapting a literature procedure[37] (**see Methods**). The resulting hydrophobic NRs were dispersible in non-polar solvents and analyzed via TEM and powder X-ray diffraction (PXRD). TEM sizing analysis reveals that the longer NRs have dimensions of 5.8 ± 0.8 nm by 61 ± 29 nm (**Figure 4.1A**), and the dimensions for the shorter NRs are 6.0 ± 0.7 nm by 22 ± 6 nm (**Figure 4.2**), while PXRD confirms their wurtzite structures (**Figure 4.3**).

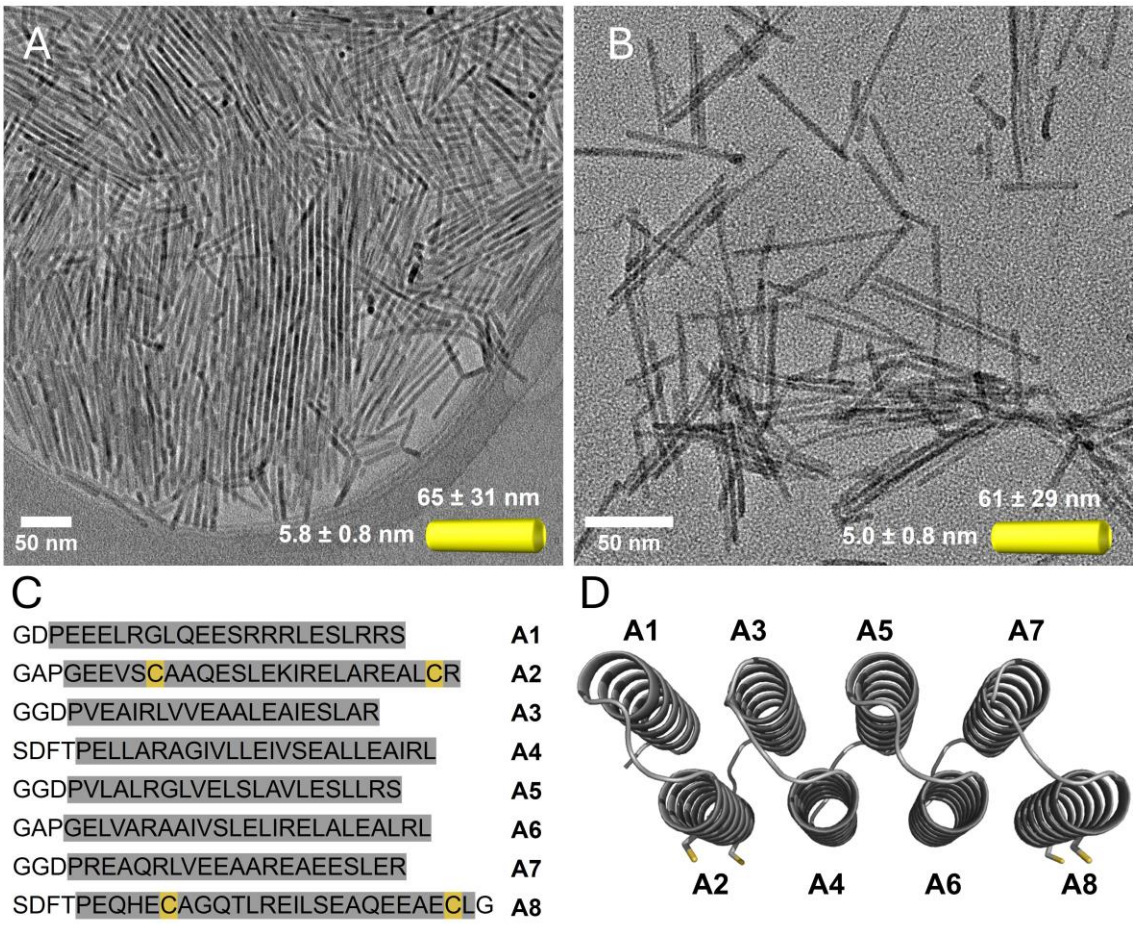

Figure 4.1 (A) TEM and sizing of longer hydrophobic CdS NRs with an average width of 5.8 ± 0.8 nm and length of 65 ± 31 nm, drop cast from toluene. (B) TEM and sizing of longer glycine:CdS NRs after ligand exchange with an average width of 5.0 ± 0.8 nm and length 61 ± 29 nm, drop cast from water. (C) DHR protein sequence containing 8 α-helices (gray) and 4 Cys residues (yellow), 2 in the A2 and 2 in the A8 helical segments. (D) Idealized surface interaction

of DHR-4Cys on CdS directed through Cys residues in A2 and A8 α-helices. The side chains of the four cysteine residues are displayed, while the remaining residues are hidden for clarity.

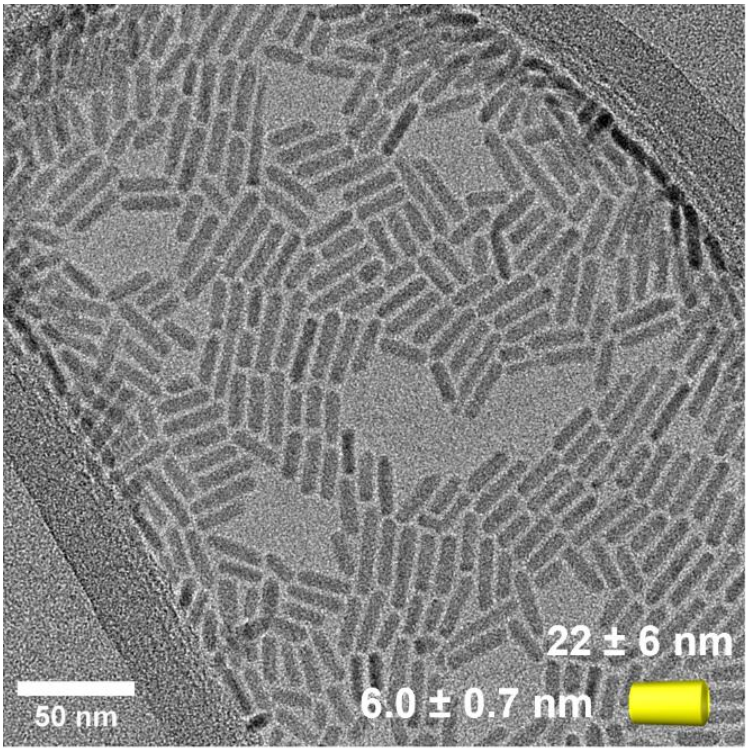

Figure 4.2 TEM and size of short TDPA:CdS NR with an average width of 6.0 ± 0.7 nm and length of 22 ± 6 nm drop cast in toluene.

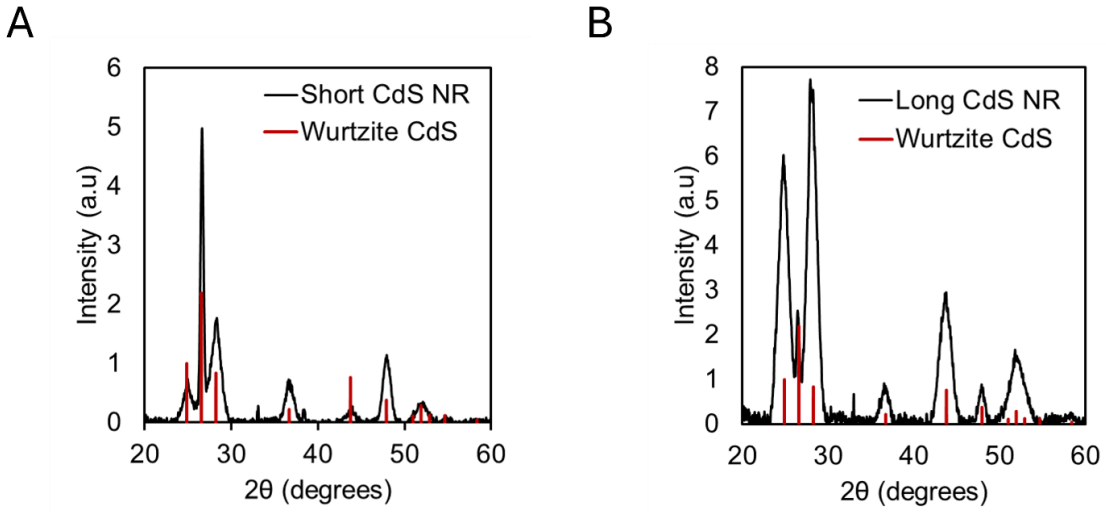

Figure 4.3 (A) PXRD Spectra of short CdS NRs (black) overlaid with wurtzite CdS (red). (B) PXRD Spectra of long CdS NRs (black) overlaid with wurtzite CdS (red).

Recognizing the lack of examples of chirality transfer between proteins and CdE in the literature, we propose that establishing chirality at the NC interface through localized binding of amino acids within an ordered protein structure is an important step in bridging length scales of chirality from the protein:CdE NC interface to protein-directed chiral assemblies of NCs. Inspired by the thiophilicity of cadmium demonstrated in Cys-containing zinc-finger domains,[38–40] we have previously leveraged the thermodynamic favorability of thiolate-Cd interactions by first exchanging hydrophobic NCs with achiral and water-soluble glycine. Following solubilization of the NCs, glycine is readily displaced by Cys-containing polypeptides as indicated by induced CD absorbance corresponding to the electronic excitations of the NCs.[25] For context, there are few literature examples of inducing interfacial chirality in achiral Au NCs with biomolecules.[41,42]

Due to the basic pH and high ligand concentrations required for exchanging hydrophobic CdE NCs into aqueous media,[17,18,26,28,30,31,43,44] we have developed a robust ligand exchange that solubilizes CdS NCs with glycine, which preserves the achiral structure of the CdS NCs.[25] Adapting this procedure, we found that the CdS NRs are readily exchanged into water (**see Methods**). After aqueous exchange, the longer NRs have dimensions of 5.0 ± 0.8 nm by 61 ± 29 nm (**Figure 4.1B**), and the shorter NRs become 4.9 ± 0.6 nm by 18 ± 5 nm (**Figure 4.4**). While both the width dimensions decrease by approximately 1 nm, the length dimensions remain unchanged after the glycine ligand exchange. Once exchanged, the achiral glycine:CdS NRs are indefinitely stable in solutions containing 1.78 M glycine in 1 M tetramethylammonium hydroxide (TMAOH) at pH 10.3. While we have found this glycine exchange to be robust for CdS NRs and QDs, isolating these NRs for NMR and IR surface-chemistry studies has remained

an outstanding challenge due to the high ionic strength required to keep the glycine-capped NCs colloidally stable.

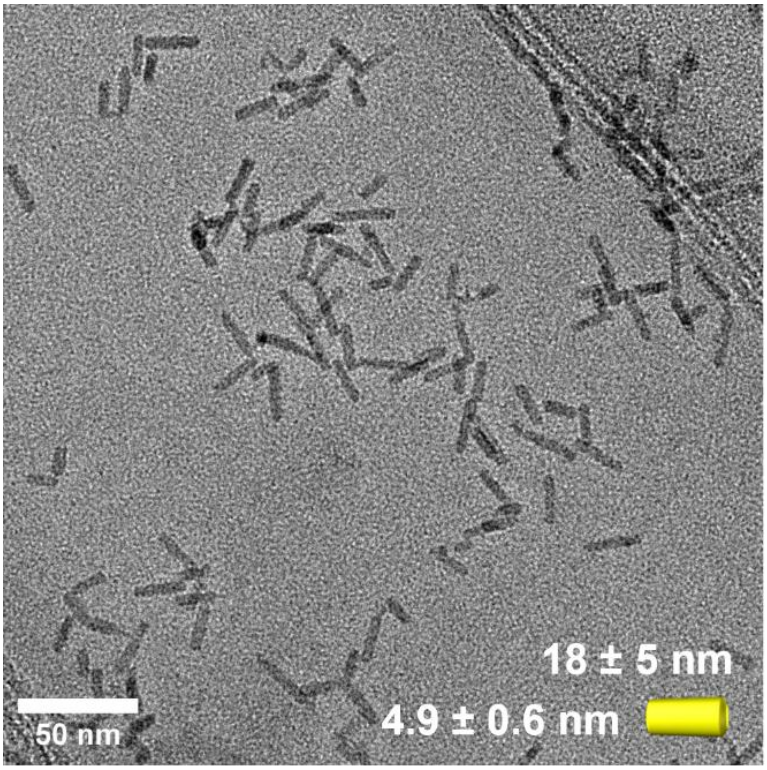

Figure 4.4 TEM and sizing of short glycine:CdS NRs after ligand exchange with an average width of 5.0 ± 0.8 nm and length 61 ± 29 nm drop cast in water.

Glycine, the only achiral amino acid, contains carboxylate and amine binding groups to passivate the surface cadmium of the NRs. After ligand exchange with glycine, we temporarily chelate the surface cadmium, making the NRs water-soluble, followed by displacement with the more thermodynamically favorable thiol of Cys.[45] Previously, we demonstrated that the achiral interface of glycine:CdS NCs could be made asymmetric via displacement of glycine by low complexity polypeptides containing a single Cys residue at the c-terminus. In this study, we aimed to extend these findings to highly ordered DHR-4Cys to determine if the asymmetry of CdS NRs can be observed. DHR-4Cys contains eight α-helices and four Cys residues with other

carboxylate side chain amino acids in their vicinity (**Figure 4.1C**). By design, DHR-4Cys has four Cys residues spaced approximately 3 nm apart on the same face of a roughly 4x4 nm plate-like protein structure (**Figure 4.1D**).

A challenge in displacing glycine from CdS NRs with a structured protein is the high equivalents of glycine (10^6/NR) required to solubilize the CdS NRs. To obtain reasonable optical densities, we used a working concentration of 75 nM of CdS with ~100 mM of glycine. Additionally, use of PBS buffer in these systems caused precipitation of the NRs out of solution, presumably due to the high salt concentrations. To preserve the DHR-4Cys structure and colloidal stability of the glycine:CdS NRs, solutions were buffered with tris(hydroxymethyl)aminomethane (tris) at pH 8.6 before the addition of DHR-4Cys (**see Methods**), where the achiral NRs maintain their optical properties (**Figure 4.5, Figure 4.6**). Once the achiral CdS NRs are incubated with DHR-4Cys, CD absorbance is observed corresponding to the electronic transitions of the long and short CdS NRs (**Figure 4.7A, Figure 4.7E)**, demonstrating CdS surface asymmetry upon the introduction of the protein without changes in the NR absorbance spectra (**Figure 4.8**). The similarities in the CD spectra between the long and short NRs (**Figure 4.9A**) can be rationalized by the similarities in their respective absorbance spectra (**Figure 4.9B**), signifying 2D NR confinement as a dominant contributor to induced chirality in these systems.

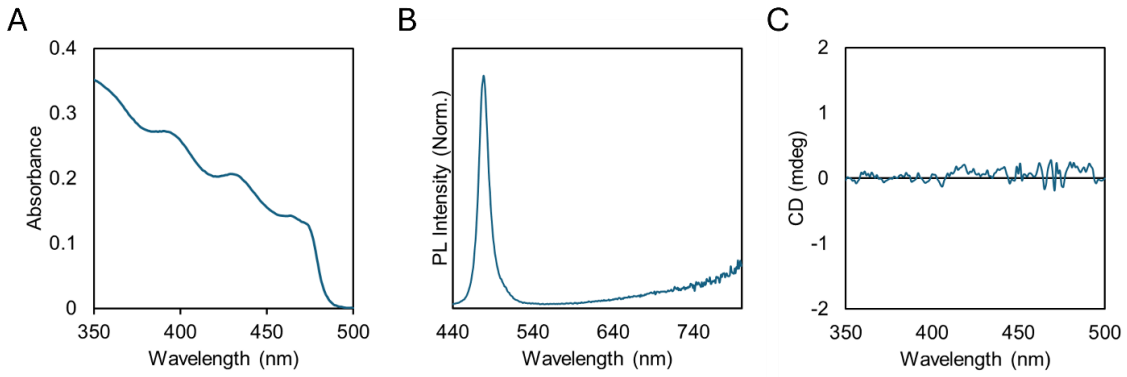

Figure 4.5 (A) Absorbance spectrum of short glycine:CdS in nanopure water. (B) Normalized PL spectrum of short glycine:CdS NRs in nanopure water. Excitation wavelength at 412 nm and normalized by the absorbance at 412 nm. (C) CD spectrum of short glycine:CdS NRs in nanopure water. All solutions contained 0.183 M tris, 0.118 M glycine, 0.066 M TMAOH, and 0.001 M TCEP HCl in nanopure water.

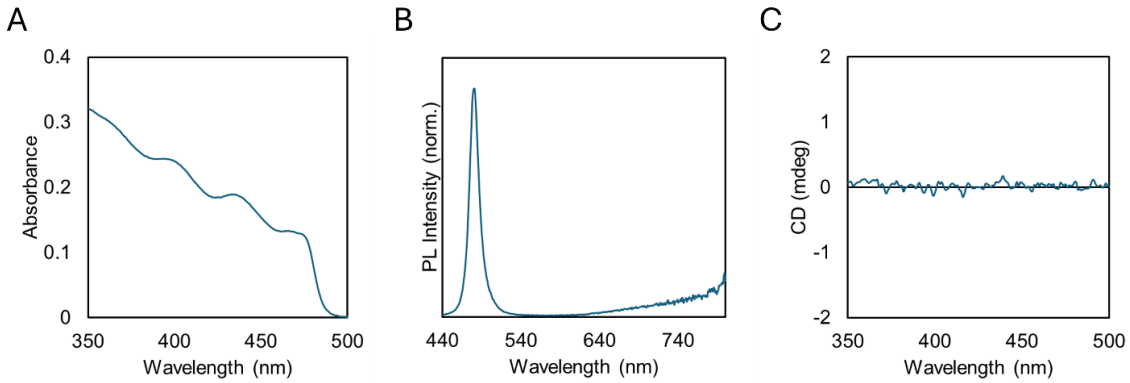

Figure 4.6 (A) Absorbance spectrum of long glycine:CdS in nanopure water. (B) Normalized PL spectrum of long glycine:CdS NRs in nanopure water. Excitation wavelength at 412 nm and normalized by the absorbance at 412 nm. (C) CD spectrum of long glycine:CdS NRs in nanopure water. All solutions contained 0.183 M tris, 0.118 M glycine, 0.066 M TMAOH, and 0.001 M TCEP HCl in nanopure water.

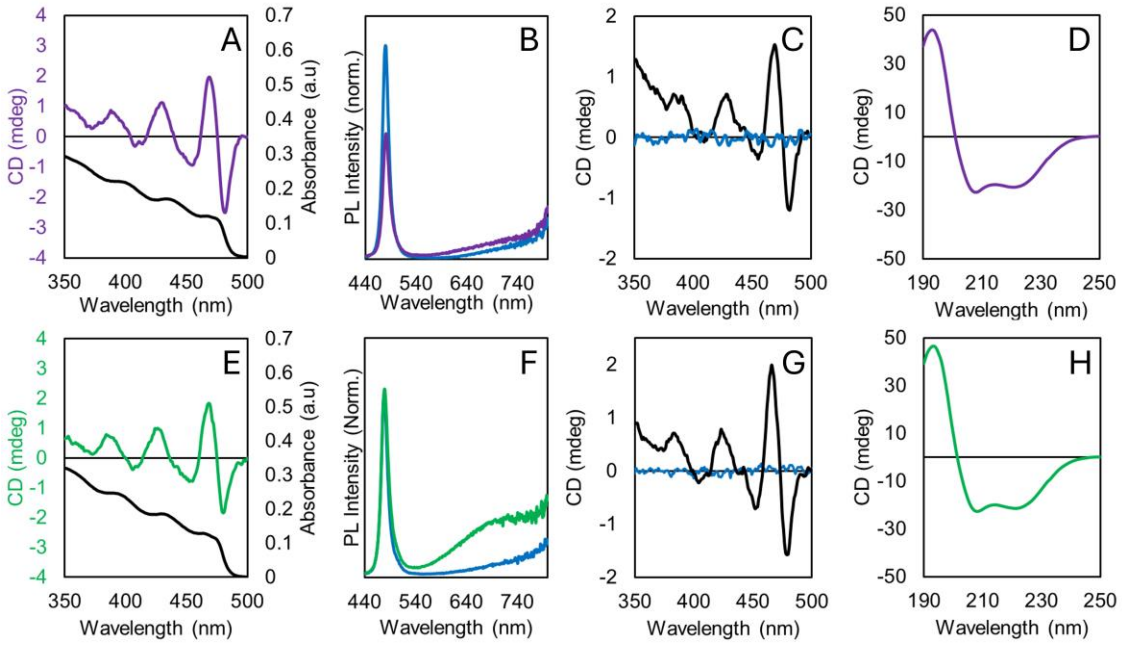

Figure 4.7 (A-D) Spectroscopic data of long CdS NRs incubated with DHR-4Cys (A) CD and absorbance spectra of 75 nM long CdS NRs (5.0 ± 0.8 nm by 61 ± 29 nm) incubated with 13.5 µM of DHR-4Cys in tris at pH 8.6. (B) Normalized PL spectra of long CdS NRs (5.0 ± 0.8 nm by 61 ± 29 nm) before (blue) and after (purple) incubation with 13.5 µM of DHR-4Cys in tris buffer at pH 8.6 (412 nm excitation wavelength). PL spectra were normalized by absorbance at 412 nm. (C) CD spectra of 75 nM long CdS NRs incubated with: 54 µM Cys (black) and 81 µM Asp, 540 µM Glu, 13.5 µM Lys and 13.5 µM His (blue) in tris buffer at pH 8.6. (D) UV CD spectrum of long DHR-4Cys:CdS NRs after dialysis against nanopure water, [DHR-4Cys:CdS NR]: 2 nM. (E-H) Spectroscopic data of short CdS NRs incubated with DHR-4Cys. (E) CD and absorbance spectra of 75 nM short CdS NRs (4.9 ± 0.6 nm by 18 ± 5 nm) incubated with 13.5 µM of DHR-4Cys in tris at pH 8.6. (F) Normalized PL spectra of short CdS NRs (4.9 ± 0.6 nm by 18 ± 5 nm) before (blue) and after (green) incubation with 13.5 µM of DHR-4Cys in tris buffer at pH 8.6 (412 nm excitation wavelength). PL spectra were normalized by absorbance at 412 nm. (G) CD spectra of 75 nM short CdS NRs incubated with: 54 µM Cys (black) and 81 µM Asp, 540 µM Glu, 13.5 µM Lys and 13.5 µM His (blue) in tris buffer at pH 8.6. (H) UV CD

spectrum of short DHR-4Cys:CdS NRs after dialysis against nanopure water, [DHR-4Cys:CdS NR]: 2 nM.

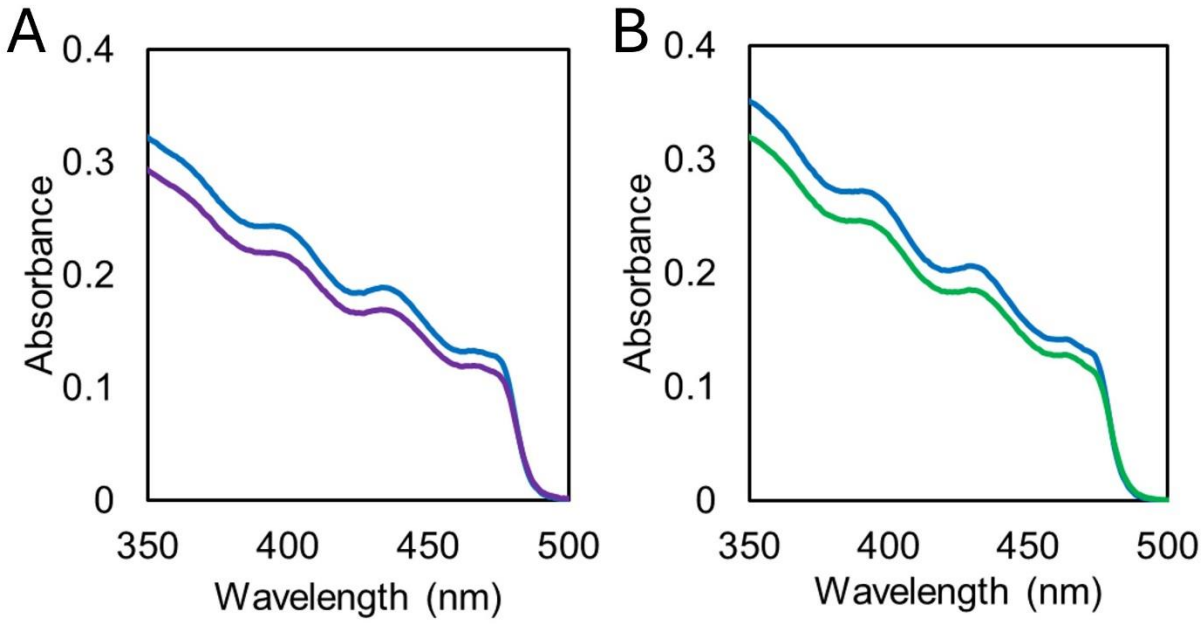

Figure 4.8 (A) UV-Vis absorbance spectra of long glycine:CdS NRs (blue) followed by the addition of 281 µL of 120 µM DHR-4Cys (purple). (B) UV-Vis absorbance spectra of short glycine:CdS NRs (blue) followed by the addition of 281 µL of 120 µM DHR-4Cys.

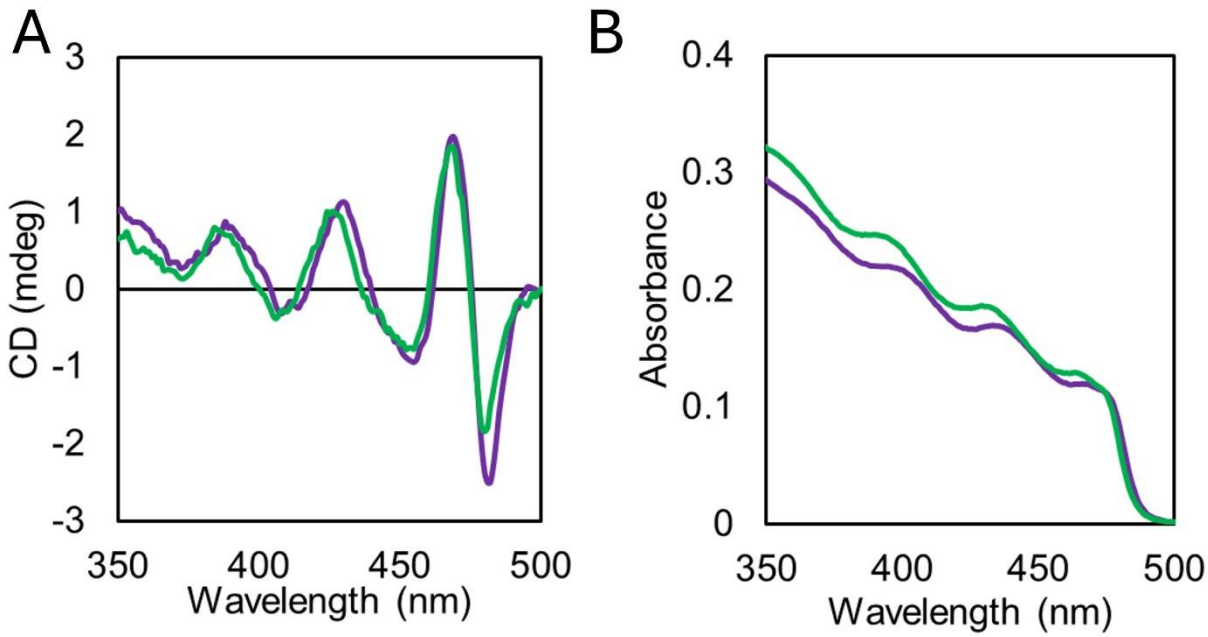

Figure 4.9 (A) CD absorbance overlays of long DHR-4Cys:CdS NRs (purple) and short DHR-4Cys:CdS NRs (green). (B) Absorbance overlays of long DHR-4Cys:CdS NRs (purple) and short DHR-4Cys:CdS NRs (green).

Accompanying the appearance of CD absorbance, changes in the photoluminescence (PL) spectrum are also observed (**Figure 4.7B, Figure 4.7F**). Comparison of the glycine:CdS NRs (**Figure 4.7B-Blue, Figure 4.7F-Blue**) and DHR-4Cys:CdS NRs (**Figure 4.7B-Purple, Figure 4.7F-Green)** shows a decrease in intensity at the band edge feature (481 nm) and increased trap state emission (600-800 nm) in the normalized PL spectra, consistent with thiol coordination of CdS NCs.[46,47] Circularly polarized luminescence measurements were attempted; however irreversible photoluminescence instability under the required excitation conditions prevented reliable quantification luminescence. Using CD absorbance and PL spectroscopies, we conclude that the protein is successfully bound to the CdS NRs, demonstrating the first example of asymmetry in CdS arising from protein conjugation at its interface.

The appearance of CD absorbance corresponding to the CdS NR electronic transitions and quenching of the band edge PL feature in the presence of DHR-4Cys suggests that the thiophilicity of surface cadmium is a strong enough thermodynamic driving force to bind DHR-4Cys on the surface of the NRs even in the presence of 10^5 equivalents of glycine per NR. To confirm the Cys residues were responsible for the induced chirality, CdS NRs were incubated with Cys (54 μM), resulting in CD absorbance that matches the DHR-4Cys:CdS NR systems (**Figure 4.7C-Black, Figure 4.7G-Black)**. To determine the influence of amino acids in the protein containing carboxylate and imidazole side chains, CdS NRs were incubated with a mixture of aspartic acid (Asp, 81 μM), glutamic acid (Glu, 540 μM), lysine (Lys, 13.5 μM), and histidine (His, 13.5 μM), and no visible CD response was observed (**Figure 4.7C-Blue**, **Figure 4.7G-Blue**). These results highlight the high affinity for Cys on the surface of the glycine:CdS NRs and are consistent with the irreversible binding of thiols on CdSe QDs reported by Dempsey et. al.[45] From this report and the results reported here, we propose at μM concentrations, ligand competition could only arise from other thiol or phosphonate binding groups. To confirm DHR-4Cys maintains its structure once bound to the NRs, DHR-4Cys:CdS NRs were dialyzed against nanopure water to remove unbound DHR-4Cys and monitored via deep UV CD spectroscopy **(Figure 4.7D, Figure 4.7H**) which matched the lineshape of unbound DHR-4Cys (**Figure 4.10**), confirming the preservation of the proteins' α-helicity on the NR surface. Additionally, after dialysis and dilution the DHR-4Cys:CdS NRs maintain their chiroptical response corresponding to the electronic transitions of the CdS NRs (**Figure 4.11, Figure 4.12**).

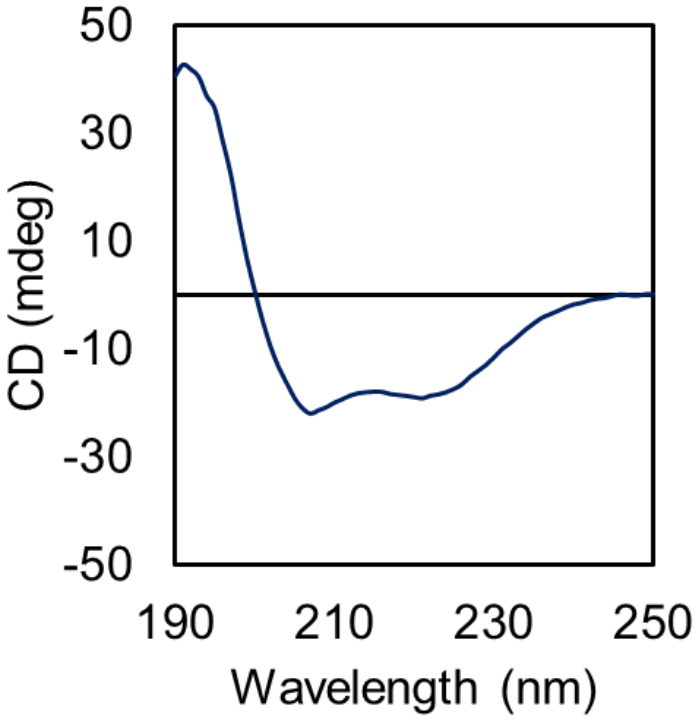

Figure 4.10 CD absorbance spectrum of DHR-4Cys in nanopure water.

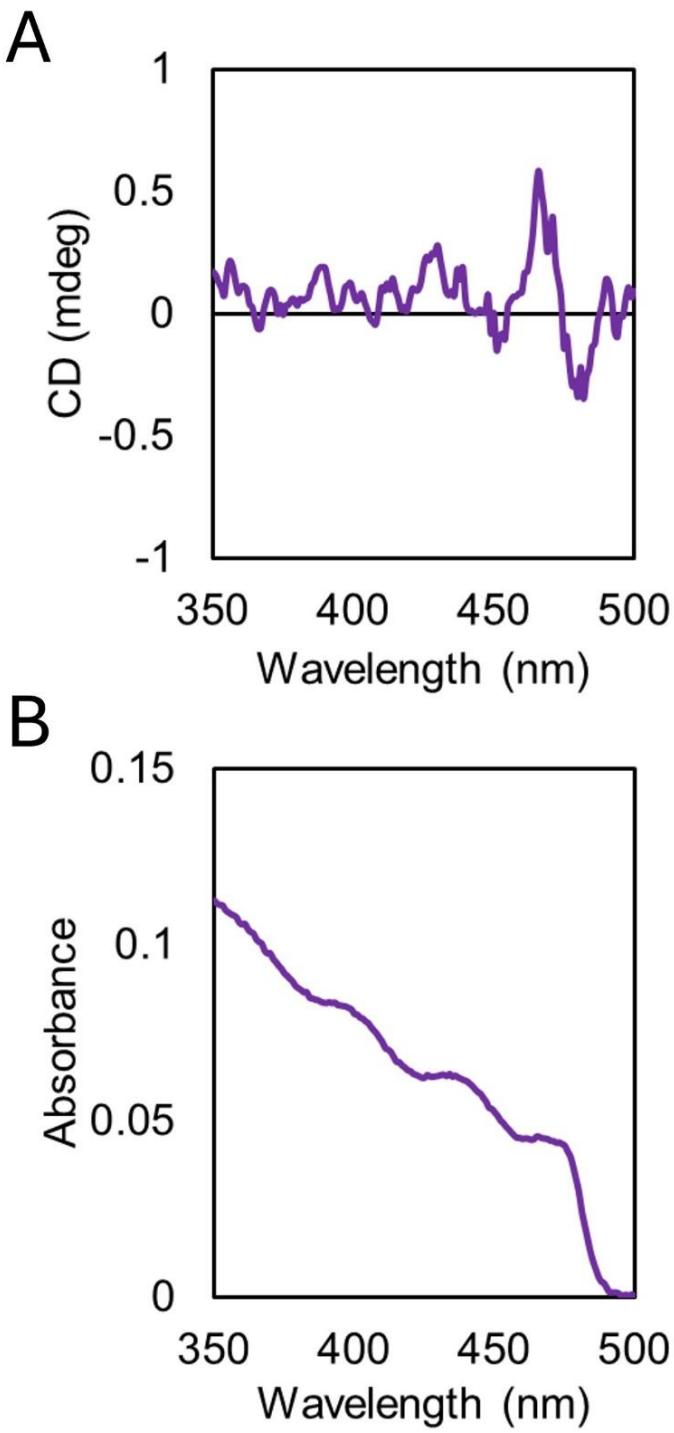

Figure 4.11 (A) CD absorbance spectrum of long DHR-4Cys:CdS NRs (2 nM) dialyzed against nanopure water. (B) Corresponding UV-Vis spectrum of long DHR-4Cys:CdS NRs dialyzed against nanopure water [CdS]: 30 nM

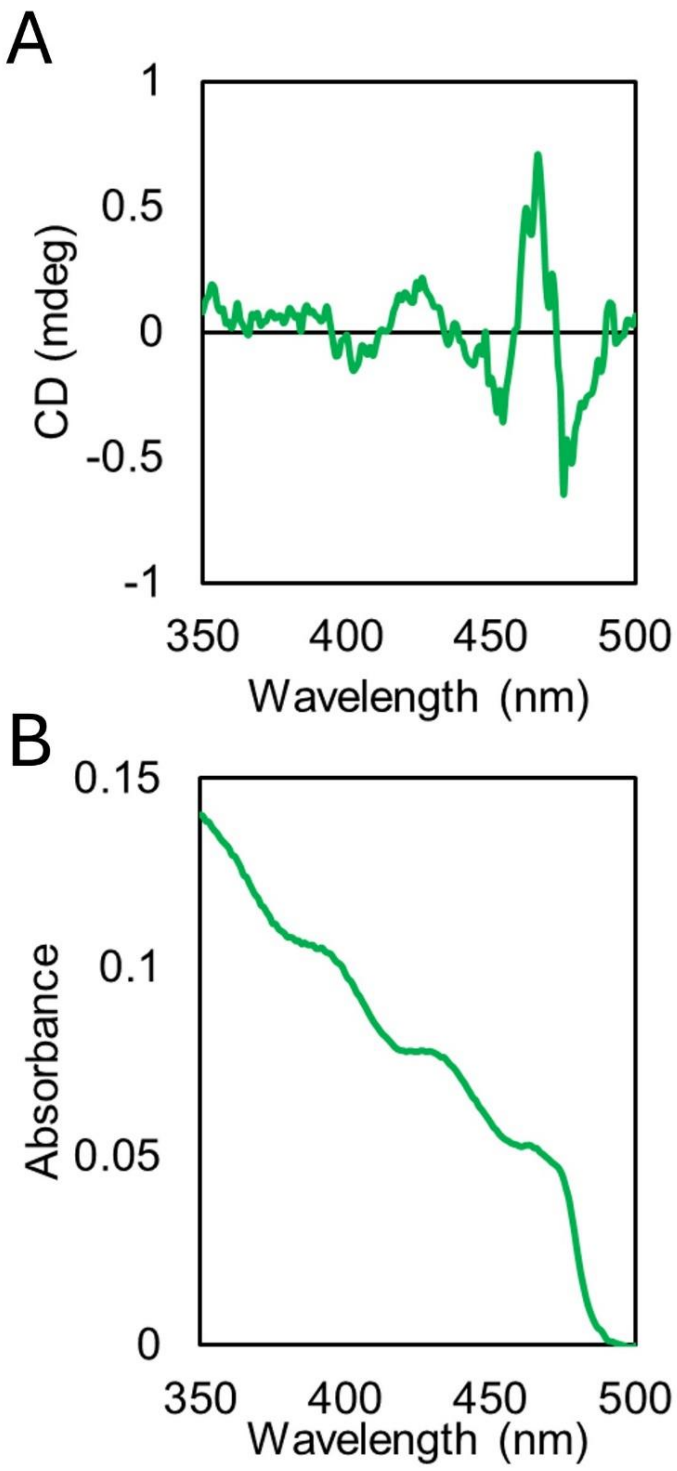

Figure 4.12 (A) CD absorbance spectrum of short DHR-4Cys:CdS NRs (2 nM) dialyzed against nanopure water. (B) Corresponding UV-Vis spectrum of short DHR-4Cys:CdS NRs dialyzed against nanopure water [CdS]: 30 nM

For normalized chirality, *g*-factors of DHR-4Cys:CdS NRs, Cys:CdS NRs, Cys:CdS QDs and polypeptide:CdS QDs were compared (**Table 4.1**). We found comparable *g*-factors for short DHR-4Cys:CdS NRs ($4.5x10^{-4}$ at 468 nm) and long DHR-4Cys:CdS ($5.0x10^{-4}$ at 469 nm) (**Figure 4.13**) indicating that increased surface area along the length facets did not significantly impact optical activity. While the mechanism of induced chirality is not fully understood, these results are consistent with previous reports on Cys:CdSe NRs by Tang and coworkers who observed NRs with aspect ratios ≥3 did not exhibit significant differences in induced chirality when ligand exchanged with Cys[31] which supports our findings with CdS NRs with varying aspect ratios (short ~4 and long ~12 aspect ratio, respectively). This previous report and our work suggest that chiroptical outcomes of NRs above aspect ratios of ~1.2 are primarily dictated by the 2D confinement dimensions.

Table 4.1 *g*-factor comparisons of short and long DHR-4Cys:CdS NRs with Cys:CdS NRs, Cys:CdS QDs, and $(VPGVG)_{54}$-Cys:CdS QDs used in our previous study.[25]

	***g*-factor ($x10^{-4}$)**
Short DHR-4Cys:CdS NR	4.5[a]
Short Cys:CdS NR	4.8[a]
Long DHR-4Cys:CdS NR	5.0[a]
Long Cys:CdS NR	4.0[a]
Cys:CdS QD	1.2[25]

$(VPGVG)_{54}$-Cys:CdS QD	0.7[25]

a-this work

To understand the impact of the chiral secondary structure of DHR-4Cys on induced chirality, we compared the *g*-factors obtained when incubating the short and long CdS NRs with 13.5 μM DHR-4Cys and 54 μM free Cys (**Figure 4.14**). Comparing *g*-factors of short DHR-4Cys:CdS NRs ($4.5x10^{-4}$ at 466 nm) with short Cys:CdS NRs ($4.8x10^{-4}$ at 466 nm) (**Figure 4.14A**), and long DHR-4Cys:CdS NRs ($5.0x10^{-4}$ at 469 nm) with long Cys:CdS NRs ($4.0x10^{-4}$ at 469 nm) (**Figure 4.14B**) do not show significant differences in *g*-factor. The close match in both magnitude and lineshape between the DHR-4Cys:CdS and Cys:CdS CD responses indicates that chiral induction arises predominantly from local thiolate-Cd interactions, with no detectable additional contribution from the higher-order protein structure under these conditions. Examination of the short and long Cys:CdS NRs vs the Cys:CdS QDs ($1.2x10^{-4}$) shows a 3-fold increase in *g*-factor consistent with higher *g*-factors of NRs vs QDs.[31] Comparison of our previous polypetide:QD system, (valine (V)-proline (P)-glycine (G)-V-G)$_{54}$-Cys:CdS QDs ($0.7x10^{-4}$) to the CdS NRs shows over a 6-fold increase in *g*-factor of the DHR-4Cys:CdS NRs compared to the polypeptide:QDs. These results suggest that *g*-factors of protein:CdS NCs are not significantly impacted by the chiral protein backbone.

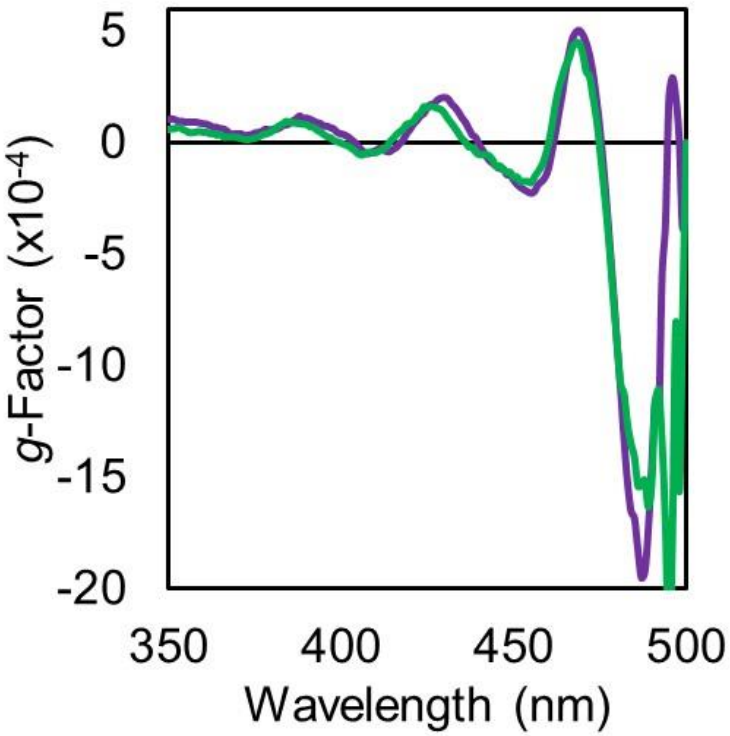

Figure 4.13 *g*-factor plots of short (green) and long (purple) DHR-4Cys:CdS NRs. *g*-factors were reported at 468 nm and 469 nm for the short and long NRs, respectively.

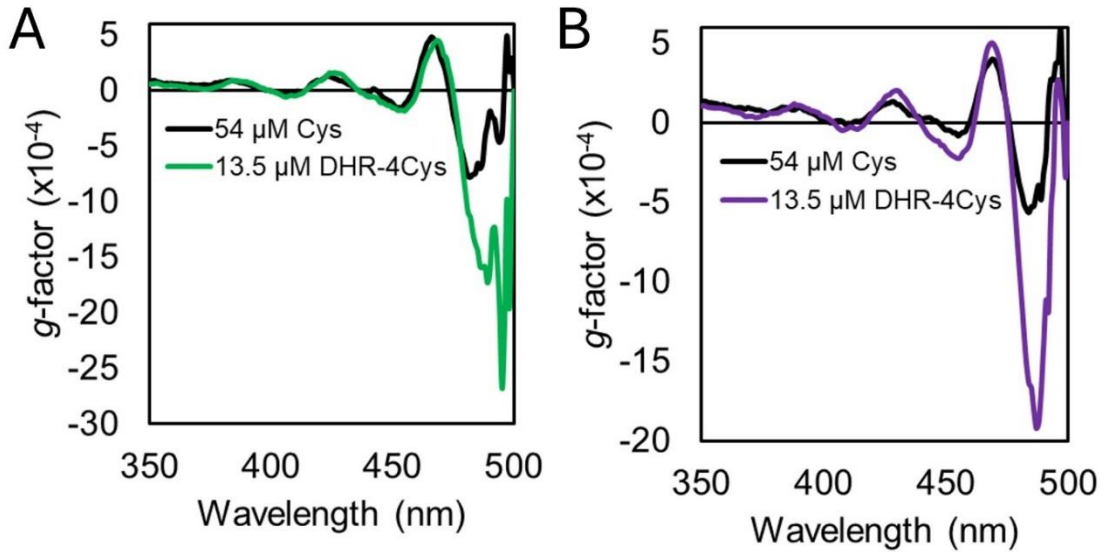

Figure 4.14 (A) *g*-factor plots of short Cys:CdS NRs (black) and short DHR-4Cys:CdS NRs (green). *g*-factor was reported at 466 nm for Cys and 468 nm for DHR-4Cys (B) *g*-factor overlay

plots of long Cys:CdS NRs (black) and DHR-4Cys:CdS NRs (purple). *g*-factor was reported at 469 nm for both Cys and DHR-4Cys.

To visualize the CdS NRs with glycine on their surface compared to DHR-4Cys, negative-stained TEM and 2D class averaging reveal significant differences in ligand shell density between protein-bound and glycine-bound NRs (**Figure 4.15**). The negative-stained TEM and class averaging of the short glycine:CdS NRs (**Figure 4.15A**) and long glycine:CdS NRs (**Figure 4.15B**) reveal NRs with no observable ligand density. This is expected due to the size of glycine (Å-scale) compared to the size of the CdS NRs (nm-scale) (**Figure 4.15C**). Through negative-stained TEM and 2D class averaging, a protein shell thickness of 2-3 nm is found on the surface of short DHR-4Cys:CdS (**Figure 4.15D**) and long DHR-4Cys:CdS NRs (**Figure 4.15E)**. These results confirm that the protein is bound to the NR surface DHR-4Cys, and the protein still maintains its helical structure (**Figure 4.15F)**. Comparison of the unbound and bound protein TEM also shows much less inter-particle aggregation in the protein-bound system, which suggests an increase in NR colloidal stability with the DHR protein on its surface.

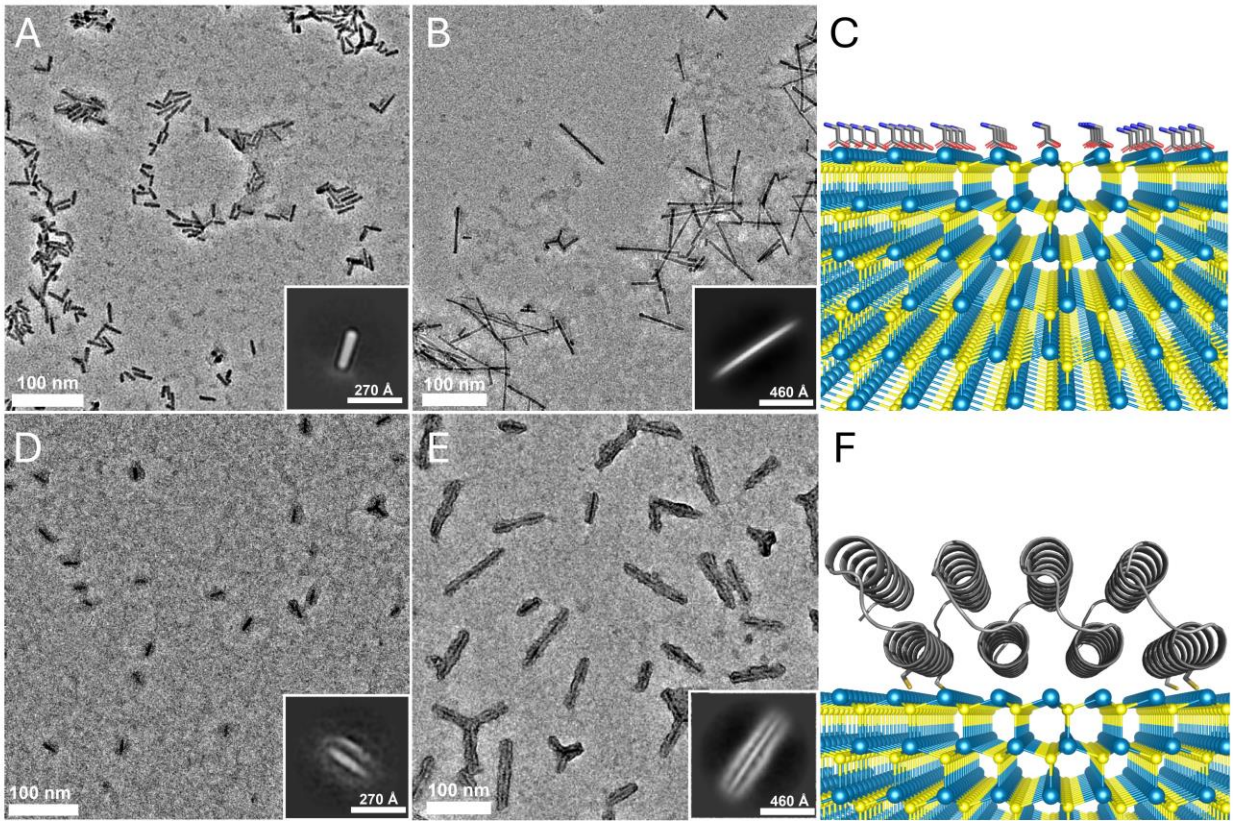

Figure 4.15 (A) Negative stain TEM of short glycine:CdS NRs and 2D class averaging of glycine ligand shell (inset). (B) Negative stain TEM of long glycine:CdS NRs and 2D class averaging of glycine ligand shell (inset). (C) Idealized CdS NR surface interaction with glycine carboxylate group at pH 8.6. Cadmium (teal), sulfur (yellow), carbon (gray), nitrogen (blue). (D) Negative stain TEM of short DHR-4Cys:CdS NRs and 2D class averaging of protein ligand shell around NRs (inset). (E) Negative stain TEM of long DHR-4Cys:CdS NRs and 2D class averaging of protein ligand shell around NRs (inset). (F) Idealized surface interaction of DHR-4Cys on CdS directed through Cys residues in A2 and A8 α-helices.

To test the stability of the plate-like structure of the DHR-4Cys on the NR surface, we monitored its α-helical structure using variable-temperature CD (**Figure 4.16A, B**). Moderate changes were observed in the CD spectra of the α-helical structures in the DHR-4Cys:CdS NRs

(**Figure 4.16A, Figure 4.17**). When monitoring the collapse of the α-helical structures of the DHR-4Cys:CdS NRs vs. the DHR-4Cys, we see no significant differences in stability of the protein on the surface of the NR vs unbound (**Figure 4.16B**). These results demonstrate that CdS NRs can be directly bound to highly ordered proteins without degradation of their structures, making them viable candidates for NCs in chiral hybrid inorganic-organic materials in which chirality spans the NC-protein interface and facilitates the hierarchical assembly of the NCs within a protein scaffold.

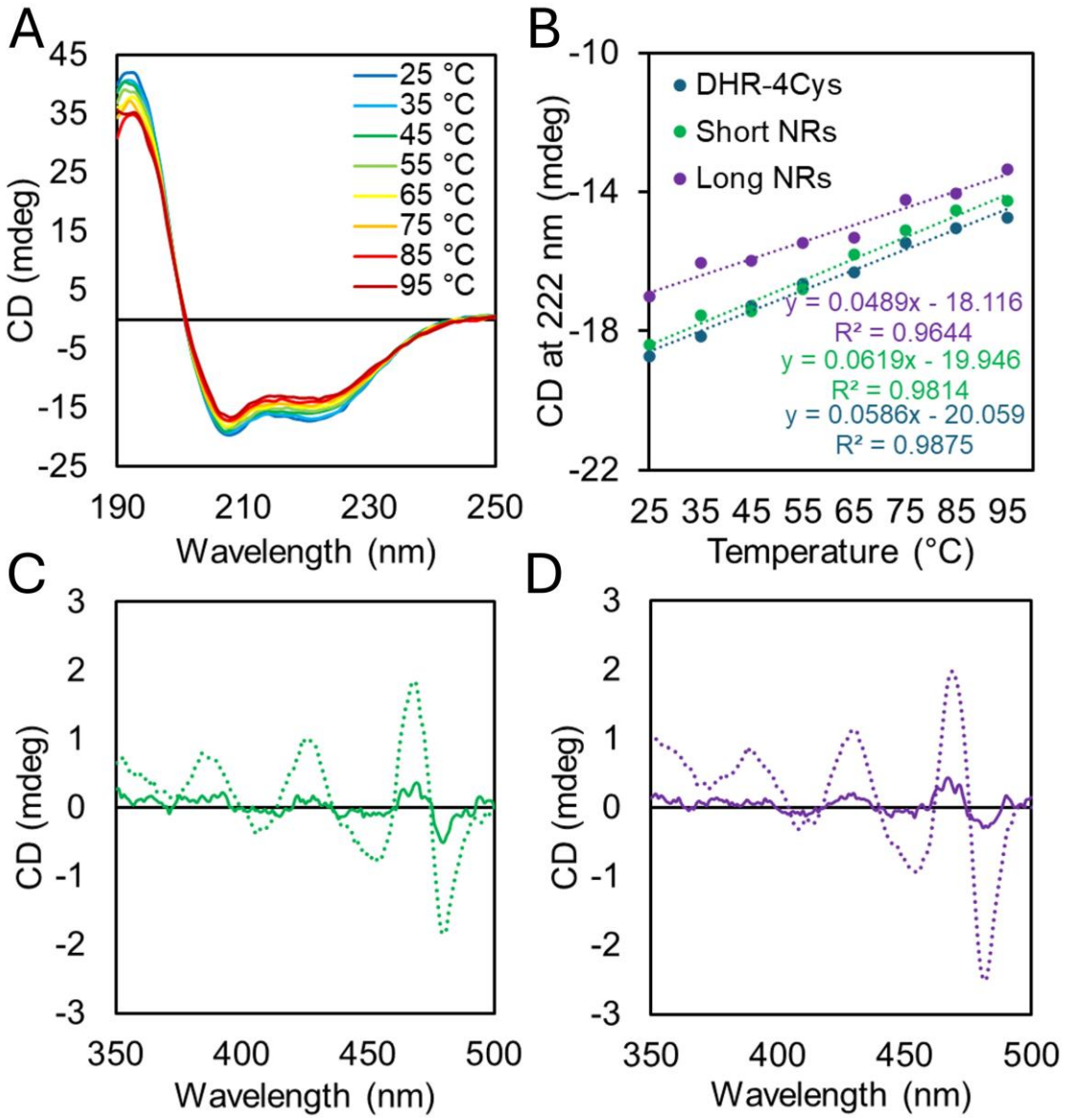

Figure 4.16 (A) Variable temperature CD spectra of long DHR-4Cys:CdS NRs (2 nM) in the UV. (B) Plot of CD absorbance of DHR-4Cys (~59 nM) unbound (blue), short DHR-4Cys:CdS NR (3 nM) (green), and long DHR-4Cys:CdS NRs (2 nM) (purple). CD absorbance values were monitored at 222 nm. (C) CD absorbance overlay of 75 nM Short CdS NRs with 170 nM (solid green) and 13.5 µM DHR-4Cys (dashed green) in tris buffer pH 8.6. (D) CD absorbance overlay of 75 nM long CdS NRs with: 170 nM (solid purple) and 13.5 µM DHR-4Cys (dashed purple) in tris buffer pH 8.6.

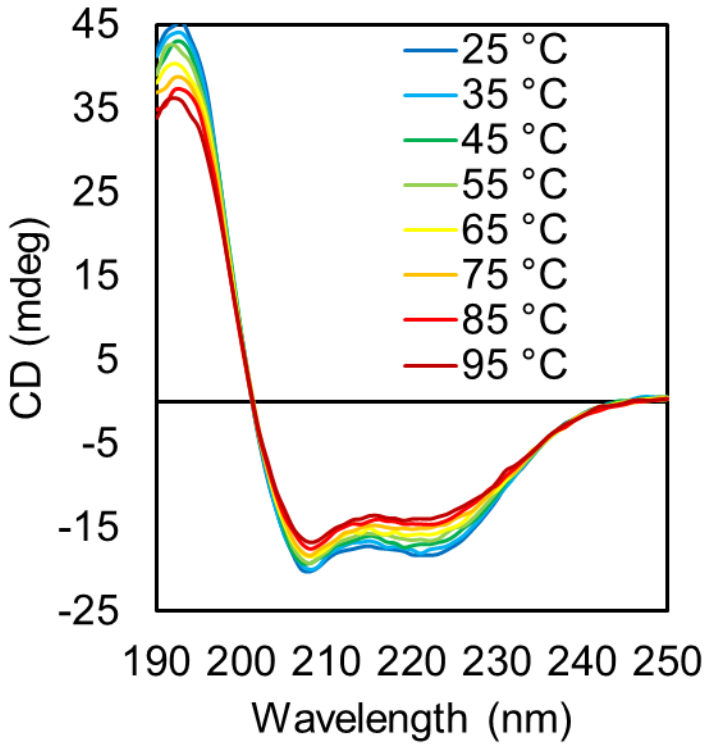

Figure 4.17 Variable temperature CD spectra of short DHR-4Cys:CdS NRs in the UV.

We hypothesized that minimal equivalents of protein to NC will be ideal for bridging chirality from protein:NC interfaces to protein:NC assemblies to maximize through-space charge transport of NCs, as Kotov and coworkers have previously described.[48] To highlight the sensitivity of the achiral interface of glycine:CdS NRs towards chiral DHR-4Cys, CD absorbance spectra of 75 nM of short CdS NRs incubated with 170 nM DHR 4-Cys (**Figure 4.16C-solid green**) and 13.5 µM DHR-4Cys (**Figure 4.16C, dashed green trace**) show a weak optical response consistent with the CD lineshape found in the higher protein concentration samples. Additionally, CD absorbance of 75 nM long CdS NRs with 170 nM DHR 4-Cys (**Figure 4.16D-solid purple**) and 13.5 µM DHR-4Cys (**Figure 4.16D-solid purple**) shows optical response of the NCs at nM concentration of protein. To demonstrate the impact morphology has on chiroptical response in these systems, we incubated the same concentration of CdS QDs and DHR-4Cys and observed no optical CD absorbance arising from the QD

electronic transitions (**see Methods**) (**Figure 4.18**). These results emphasize the advantage of using CdS NRs to bridge chirality from the surface to protein assembly length scales in inorganic-organic hybrid materials, as the CdS NR surface is sensitive enough to detect just nM concentrations of protein.

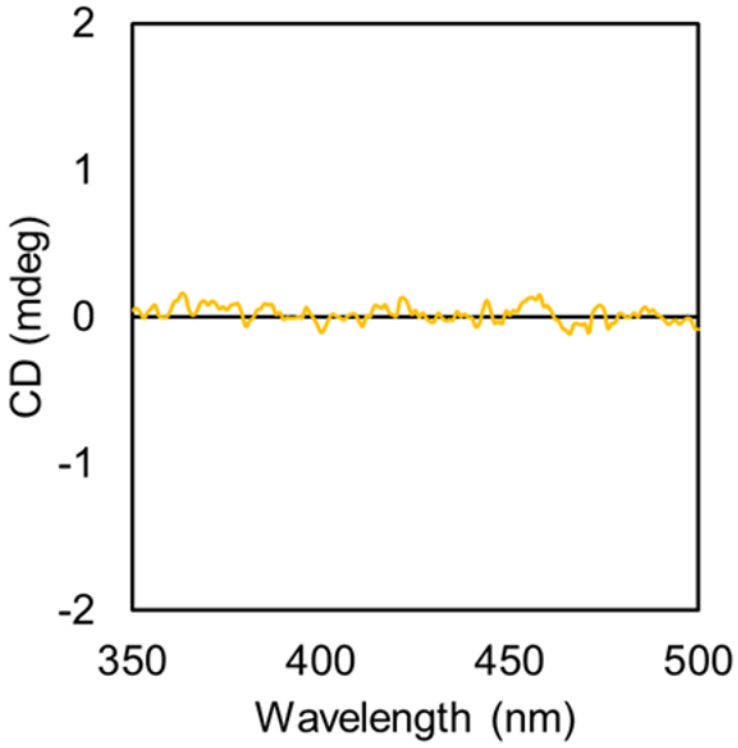

Figure 4.18 CD absorbance spectrum of 75 nM CdS QDs incubated with 13.5 μM DHR-4Cys in tris buffer pH 8.6

4.3 Conclusions

NC chirality has been demonstrated to arise across molecular, interfacial, and macromolecular length scales. While there have been several successful efforts across these length scales using small molecules, there have been limited examples of using proteins to induce asymmetry in NCs. For the first time, we have demonstrated that chirality can be induced in CdS NRs using a plate-like DHR-4Cys protein with an ordered structure. We demonstrate that

this phenomenon arises from CdS NR surface asymmetry introduced by chelating Cys residues in the protein. We were able to show that the α-helical and plate-like tertiary structure of the protein is preserved when a protein is bound to a CdS NR surface. Additionally, we report the *g*-factors of $4.5x10^{-4}$ for 4.9 ± 0.6 nm by 18 ± 5 nm NRs and $5.0x10^{-4}$ 5.0 ± 0.8 nm by 61 ± 29 nm DHR-4Cys:CdS NRs, demonstrating that NR length does not significantly impact *g*-factor. Excitingly, we have also demonstrated that the surface of the glycine:CdS NRs is sensitive enough to detect just nM concentrations of DHR-4Cys while no CD response is observed in spherical CdS NCs for μM concentrations of DHR-4Cys. Moving forward, we believe these results can inform the design of chiral biomolecule:NC interfaces and serve as a starting point for deterministic construction of protein:NC assemblies with chirality across length scales.

4.4 Experimental Methods.

4.4.1 *Materials*

The following chemicals were used without purification. Cadmium oxide powder (CdO, 99.95%), sulfur powder (99.95%), trioctylphosphine (TOP, 90%), oleic acid (90%). tetramethylthiourea (98%), tetramethylammonium hydroxide solution (TMAOH, 10% wt in water), glycine (98%), L-cysteine (Cys, 97%), L-aspartic acid (Asp, ≥98%), L-glutamic acid (Glu, ≥99%), L-lysine (Lys, 98%), L-histidine (His) tris(2-carboxyethyl)phosphine hydrochloride powder (TCEP•HCl, ≥98%), tris(hydroxymethyl)aminoethane base (Tris, ≥99.8%), hydrochloric acid (HCl, 37%), methanol (≥99.9%), and toluene (≥99.8%) were purchased from MilliporeSigma. n-tetradecylphosphonic acid (TDPA, 99%) was purchased from PCI Synthesis. Dowtherm was purchased from Dow Inc. Float-A-Lizer® dialysis devices (1 mL, 50 kDa cutoff) were purchased from Repligen. PD-10 desalting columns packed with Sephadex™ G-25 M resin were purchased from Cytiva. Trioctylphosphine oxide (TOPO) (90%)

was purchased from MilliporeSigma and recrystallized following a literature procedure.[49] Cadmium oleate was synthesized following previous literature.[50] Uranium formate (2 wt%) was purchased from SPI-Chem. 18.2 MΩ water was collected from an EMD Millipore purification system. UV−vis spectra were collected on a Cary 60 spectrophotometer from Agilent. Photoluminescence spectra were collected on a Horiba Scientific FluoroMax-4 spectrofluorometer. CD spectra were collected on a Jasco J-1500 (Scan rate: 100 nm/min, data pitch 1 nm, 15 scans, path length: 1 cm). Negative stained TEM data were collected on a FEI Talos L120C TEM, 120 kV (FEI Thermo Scientific, Hillsboro, OR) equipped with a Ceta 4K CCD camera. Micrographs collection was automated using the EPU software (FEI Thermo Scientific). Non-stained TEM images were collected on a FEI Tecnai G2 F20 SuperTwin microscope operated at 200 keV for bright field. All TEM samples were prepared on ultrathin lacey carbon support film, 400 mesh, copper grids (TED Pella Inc.)

4.4.2 *Synthesis of Shorter CdS NRs*

Synthesis of the shorter CdS NRs was adapted from literature.[37] The day before the synthesis, sulfur (0.045 g, 1.4 mM) was prepared in TOP (5 mL) in a glovebox. In a dried 50 mL 3-neck flask, CdO (0.0575 g, 0.45 mM), TOPO (1.75 g, 4.5 mM), and TDPA (0.2075 g, 0.75 mM) were degassed at 90 °C for 90 minutes. After 90 minutes, under nitrogen, the flask was heated to 340 °C for 10 minutes. After 10 minutes, the temperature was set to 300 °C and equilibrated. Once equilibrated, 1.5 mL of the previously prepared TOP-S solution was rapidly injected into the 3-neck flask and the solution was left to re-equilibrate at 300 °C. This solution was left at 300 °C for 90 minutes. After 90 minutes, a 5 mL syringe was loaded with the remaining TOP-S solution and injected at a rate of 2.5 mL/hr while keeping the temperature at

300 °C. After the syringe injection was finished (~60 minutes) the NRs were left at 300 °C for an additional 20 minutes. The solution was then quickly removed from heat and rapidly cooled with air. Once the temperature reached 70 °C, 5 mL of toluene was rapidly injected. Next, the reaction was transferred to centrifuge tubes in a 3:1 MeOH:TOPO/toluene ratio and centrifuged at 10,000 RPM for 10 minutes. The resulting pellet was then resuspended in minimal toluene and MeOH was added to achieve a 3:1 MeOH:toluene ratio and centrifuged at 10,000 RPM for 10 minutes for 2 additional cycles. Finally, the pellet was dissolved in 3x10 mL toluene, sonicated for 10 minutes and centrifuged at 10,000 RPM for 10 mins. The resulting pellet was minimally soluble in toluene and analyzed via TEM and PXRD.

4.4.3 *Synthesis of Longer CdS NRs*

Synthesis of the shorter CdS NRs was adapted from literature.[37] The day before the synthesis, sulfur (0.045 g, 1.4 mM) was prepared in TOP (5 mL) in a glovebox. In a dried 50 mL 3-neck flask, CdO (0.0575 g, 0.45 mM), TOPO (1.75 g, 4.5 mM), and TDPA (0.2075 g, 0.75 mM) were degassed at 90 °C for 90 minutes. After 90 minutes, under nitrogen, the flask was heated to 340 °C for 10 minutes. After 10 minutes, the temperature was set to 300 °C and equilibrated. Once equilibrated, 1.5 mL of the previously prepared TOP-S solution was rapidly injected into the 3-neck flask, and the solution was left to re-equilibrate at 300 °C. This solution was left at 300 °C for 90 minutes. After 90 minutes, a 5 mL syringe was loaded with 1.6 mL of the TOP-S solution and injected at a rate of 2.5 mL/hr while keeping the temperature at 300 °C. After the syringe injection was finished (~30 minutes) the NRs were left at 300 °C for an additional 20 minutes. The solution was then quickly removed from heat and rapidly cooled with air. Once the temperature reached 70 °C, 5 mL of toluene was rapidly injected. Next, the reaction

was transferred to centrifuge tubes in a 3:1 MeOH:TOPO/toluene ratio and centrifuged at 10,000 RPM for 10 minutes. The resulting pellet was then resuspended in minimal toluene and MeOH was added to achieve a 3:1 MeOH:toluene ratio and centrifuged at 10,000 RPM for 10 minutes for 2 additional cycles. Finally, the pellet was dissolved in 3x10 mL toluene, sonicated for 10 minutes and centrifuged at 10,000 RPM for 10 mins. The resulting pellet was minimally soluble in toluene and analyzed via TEM and PXRD.

4.4.4 *Synthesis of CdS QDs*

The synthesis of CdS QDs was adapted from Hamachi et al.[50] Cadmium oleate (1.287g, 1.9 mmol), oleic acid (1.3 mL, 4.1 mmol), and hexadecane (60 mL) were added to a dried three-necked 250 mL round-bottomed flask equipped with a stir bar, thermowell, reflux condenser, and rubber septum. The flask was evacuated at 90 °C for 1 h. Next, the flask was put under dynamic nitrogen and heated to 230 °C. Under a nitrogen atmosphere, tetramethylthiourea (TMTU, 0.2075 g, 1.6 mmol) was dissolved in Dowtherm (3.0 mL). The TMTU solution was rapidly injected into the cadmium oleate solution and allowed to react for 3 h until there were no UV−vis absorbance changes. The temperature was then lowered to 120 °C, the condenser was quickly replaced with a distillation arm equipped with a 250 mL round-bottomed flask, and the solvent was removed via vacuum distillation. Once cooled to room temperature, in air, minimal toluene was added, and the solution was transferred to centrifuge tubes followed by precipitation with methanol (3:1 methanol:toluene) and centrifugation at 8,000 rpm for 10 min. The supernatant was discarded, and the yellow pellet was redissolved in minimal toluene. This process was repeated for 3 precipitation and centrifugation cycles. The pellet was then suspended in 10 mL of toluene and centrifuged at 8,000 rpm for 10 min. The yellow supernatant was then decanted

away and stored in a vial in air. QD size was determined to be 5.6 nm via the Peng sizing curve.[51]

4.4.5 *CdS NR Glycine Exchange Procedure*

This procedure was adapted from our previous work.[25] In short, 5-7 mg of CdS NRs were transferred into a new vial and dried. To this vial, 6 mL of 1.78 M glycine in 1 M TMAOH were added and the solution was stirred overnight in the dark. To this solution 6 mL of toluene was added and stirred followed by centrifugation at 8,000 RPM for 10 minutes, producing a colorless top layer and a yellow bottom layer with white foam separating the layers. This toluene washing process was repeated for 3 total cycles. The aqueous layer was then transferred to a vial and allowed to sit at 4 °C in the dark for 48 hours. After 48 hours, the solution was centrifuged at 8,000 RPM for 10 minutes and the resulting solution was stored in air at room temperature and in the dark. Concentration of the glycine:CdS NR solutions were determined via the Peng sizing curve[51] and were typically ~1 μM.

4.4.6 *CdS QD Glycine Exchange Procedure*

This procedure was adapted from our previous work.[25] To a vial, oleate:CdS QDs (10 nmol) were added and dried. To this vial, 3 mL of 1.78 M glycine in 1 M TMAOH was added and stirred in the dark overnight. To this solution, 6 mL of toluene was added, and the mixture was vigorously stirred. This solution was centrifuged at 8,000 rpm for 10 min, producing a slightly yellow organic layer and a dark-yellow bottom layer. The top layer was removed, and 3 mL of toluene was added, followed by vortex mixing. This washing and centrifugation process

was repeated for 3 total cycles. The resulting solution was then stored in the dark at 4 °C for 48 hours. After 48 hours, solution was centrifuged at 8,000 RPM for 10 minutes and stored in air in the dark. QD size was determined to be 5.4 nm via the Peng sizing curve.[51]

4.4.7 *DHR-4Cys Expression and Purification*

Proteins were expressed in E. coli BL21(DE3) using 50 mL autoinduction media (Terrific Broth Base with Trace Elements, Formedium) supplemented with kanamycin. Cultures were grown at 37 °C for 6 h and then shifted to 18 °C for an additional 18 h before harvesting by centrifugation at 4,000 × g for 15 min. Cell pellets were resuspended in lysis buffer (25 mM Tris-HCl, 300 mM NaCl, 30 mM imidazole, pH 8.0, Pierce protease inhibitor tablets) and lysed by sonication. Lysates were clarified by centrifugation at 14,000 × g for 30 min, and the resulting supernatant was collected and purified by immobilized metal affinity chromatography (IMAC). Eluted samples were filtered and further purified by size-exclusion chromatography (SEC) on a fast protein liquid chromatography (FPLC) system equipped with a Superdex 75 Increase 10/300 GL column in Tris-buffered saline (25 mM Tris, 100 mM NaCl, 1mM TCEP) at room temperature. Final proteins were buffer-exchanged and concentrated into 200 mM Tris buffer using 3 kDa MWCO centrifugal spin filters and stored at 4 °C prior to downstream characterization. Final protein concentrations were determined using a Bradford assay with Coomassie Brilliant Blue G-250.

4.4.8 *Short DHR-4Cys:CdS NR Exchange*

The working volume for DHR-4Cys:CdS NR samples was 2.5 mL. In a cuvette, 457 µL of 1 M tris pH 8.6 buffered solution was added to 1.603 mL of nanopure water followed by the addition 12.1 µL of a freshly prepared 0.206 M TCEP•HCl in nanopure water solution. To this buffered solution 147 µL of 1.27 µM short glycine:CdS NRs in 1.78 M glycine and 1 M TMAOH was added to the cuvette. Finally, 281 µL of 120 µM DHR-4Cys was added to the solution and allowed to incubate at 4 °C for 30 minutes before taking optical measurements. The following are the working concentrations of prepared solutions: [CdS]: 75 nM, [Tris]: 190 mM, [TCEP•HCl]: 1 mM, [DHR-4Cys]: 13.5 µM, [glycine]: 105 mM, and [TMAOH]: 59 mM. For dialyzed samples, 1 mL of solution was added to 1 mL Floatalizer filter and dialyzed against nanopure water followed by dilution of 2.1 times before CD and absorbance measurements.

4.4.9 *Long DHR 4Cys:CdS NR Exchange*

The working volume for DHR-4Cys:CdS NR samples was 2.5 mL. In a cuvette, 457 µL of 1 M tris pH 8.6 buffered solution was added to 1.601 mL of nanopure water followed by the addition 12.1 µL of a freshly prepared 0.206 M TCEP•HCl in nanopure water solution. To this buffered solution 149 µL of 1.26 µM long glycine:CdS NRs in 1.78 M glycine and 1 M TMAOH was added to the cuvette. Finally, 281 µL of 120 µM DHR-4Cys was added to the solution and allowed to incubate at 4 °C for 30 minutes before taking optical measurements. The following are the working concentrations of prepared solutions: [CdS]: 75 nM, [Tris]: 190 mM, [TCEP•HCl]: 1 mM, [DHR-4Cys]: 13.5 µM, [glycine]: 106 mM, and [TMAOH]: 60 mM. For dialyzed samples, 1 mL of solution was added to 1 mL Floatalizer filter and dialyzed against nanopure water followed by dilution of 2.1 times before CD and absorbance measurements.

4.4.10 *Short Cys:CdS NR Exchange*

The working volume for Cys:CdS NR samples was 2.5 mL. In a cuvette, 457 µL of 1 M tris pH 8.6 buffered solution was added to 1.877 mL of nanopure water followed by the addition 12.1 µL of a freshly prepared 0.206 M TCEP•HCl in nanopure water solution. To this buffered solution 147 µL of 1.27 µM short glycine:CdS NRs in 1.78 M glycine and 1 M TMAOH was added to the cuvette. Finally, 6.4 µL of freshly prepared 20.6 mM Cys in nanopure water solution was added to the NRs and allowed to incubate at 4 °C for 30 minutes before taking optical measurements. The following are the working concentrations of prepared solutions: [CdS]: 75 nM, [Tris]: 184 mM, [TCEP•HCl]: 1 mM, [Cys]: 54 µM, [glycine]: 105 mM, and [TMAOH]: 59 mM.

4.4.11 *Long Cys:CdS NR Exchange*

The working volume for Cys:CdS NR samples was 2.5 mL. In a cuvette, 457 µL of 1 M tris pH 8.6 buffered solution was added to 1.876 mL of nanopure water followed by the addition 12.1 µL of a freshly prepared 0.206 M TCEP•HCl in nanopure water solution. To this buffered solution 149 µL of 1.26 µM long glycine:CdS NRs in 1.78 M glycine and 1 M TMAOH was added to the cuvette. Finally, 6.4 µL of freshly prepared 20.6 mM Cys in nanopure water solution was added to the NRs and allowed to incubate at 4 °C for 30 minutes before taking optical measurements. The following are the working concentrations of prepared solutions: [CdS]: 75 nM, [Tris]: 184 µM, [TCEP•HCl]: 1 mM, [Cys]: 54 µM, [glycine]: 105 mM, and [TMAOH]: 59 mM.

4.4.12 *Short Glycine:CdS NRs+ Asp, Glu, His, and Lys*

The working volume for Cys:CdS NR samples was 2.5 mL. In a cuvette, 457 µL of 1 M tris pH 8.6 buffered solution was added to 1.775 mL of nanopure water followed by the addition 12.1 µL of a freshly prepared 0.206 M TCEP•HCl in nanopure water solution. To this buffered solution 147 µL of 1.27 µM short glycine:CdS NRs in 1.78 M glycine and 1 M TMAOH was added to the cuvette. Stock solutions of Asp (4.1 mM, 49.4 µL), Glu (33 mM, 40.9 µL), His (4.1 mM, 8.2 µL), and Lys (3.6 mM, 9.4 µL) in nanopure water were added to the NR solution incubate at 4 °C for 30 minutes before taking optical measurements. The following are the working concentrations of prepared solutions: [CdS]: 75 nM, [Tris]: 184 mM, [TCEP•HCl]: 1 mM, [Asp]: 81 µM, [Glu]: 540 µM, [His]: 13.5 µM, [Lys]: Lys 13.5 µM [glycine]: 105 mM, and [TMAOH]: 59 mM.

4.4.13 *Long Glycine:CdS NRs+ Asp, Glu, His, and Lys*

The working volume for Cys:CdS NR samples was 2.5 mL. In a cuvette, 457 µL of 1 M tris pH 8.6 buffered solution was added to 1.773 mL of nanopure water followed by the addition 12.1 µL of a freshly prepared 0.206 M TCEP•HCl in nanopure water solution. To this buffered solution 149 µL of 1.26 µM long glycine:CdS NRs in 1.78 M glycine and 1 M TMAOH was added to the cuvette. Stock solutions of Asp (4.1 mM, 49.4 µL), Glu (33 mM, 40.9 µL), His (4.1 mM, 8.2 µL), and Lys (3.6 mM, 9.4 µL) in nanopure water were added to the NR solution incubate at 4 °C for 30 minutes before taking optical measurements. The following are the working concentrations of prepared solutions: [CdS]: 75 nM, [Tris]: 184 mM, [TCEP•HCl]: 1 mM, [Asp]: 81 µM, [Glu]: 540 µM, [His]: 13.5 µM, [Lys]: Lys 13.5 µM [glycine]: 105 mM, and [TMAOH]: 59 mM.

4.4.14 *Deep UV CD*

DHR-4Cys:CdS NR samples were dialyzed against nanopure water using a 50 kDa Float-A-Lizer dialysis device. This solution was diluted 23 times. For DHR-4Cys samples, 2.5 mL of a 59 nM protein solution was de-salted using a PD-10 column prior to DeepUVCD. Scan rate 100 nm/min, data pitch 1 nm. For variable temp CD, the holder was set to take 2 scans at 25 °C, 35 °C, 45 °C, 55 °C, 65 °C, 75 °C, 85 °C and 95 °C with a temperature ramp rate of 1 °C/min and 30 sec equilibration time.

4.4.15 *Negative-Stained TEM*

Glycine:CdS NR (75 nM) samples were eluted through a PD-10 column and diluted 2 times. After dilution, 5 μL of this solution was dropcast on a lacy carbon grid and allowed to sit for 10 minutes. Next, the grid was negatively stained with 2 wt% uranium formate (SPI-Chem, CAS #16984-59-1) in nanopure water by adding 3 μL of stain to the grid for 30 seconds followed by wicking off with a kimtech wipe. This staining process was repeated for a total of 3 cycles. DHR-4Cys:CdS NR (75 nM) samples were dialyzed against nanopure water and diluted 2 times. Following dilution 5 μL of this solution was dropcast onto a lacey carbon grid for 10 minutes. The grids were then stained using the same procedure described for the glycine:CdS NR samples.

4.4.16 *Negative-Stained EM Data Processing*

Micrographs were imported into cryoSPARC and processed by patch CTF estimation followed by manual particle picking. Approximately 100 particles were manually picked and subjected to 2D classification; selected classes were used to generate templates for template-based picking with an estimated particle diameter of 700 Å. Using these templates, ~15,000

particles were picked for downstream 2D classification, from which ~7,000 particles displaying uniform rod-like shapes coated with protein layers were retained.

4.5 REFERENCES

(1) Martynenko, I. V.; Litvin, A. P.; Purcell-Milton, F.; Baranov, A. V.; Fedorov, A. V.; Gun'ko, Y. K. Application of Semiconductor Quantum Dots in Bioimaging and Biosensing. J. Mater. Chem. B 2017, 5 (33), 6701–6727. https://doi.org/10.1039/C7TB01425B.

(2) Zhang, N.-N.; Mychinko, M.; Gao, S.-Y.; Yu, L.; Shen, Z.-L.; Wang, L.; Peng, F.; Wei, Z.; Wang, Z.; Zhang, W.; Zhu, S.; Yang, Y.; Sun, T.; Liz-Marzán, L. M.; Bals, S.; Liu, K. Self-Matching Assembly of Chiral Gold Nanoparticles Leads to High Optical Asymmetry and Sensitive Detection of Adenosine Triphosphate. Nano Lett. 2024, 24 (41), 13027–13036. https://doi.org/10.1021/acs.nanolett.4c03782.

(3) Quesada-González, D.; Merkoçi, A. Quantum Dots for Biosensing: Classification and Applications. Biosens. Bioelectron. 2025, 273, 117180. https://doi.org/10.1016/j.bios.2025.117180.

(4) Li, S.; Xu, X.; Xu, L.; Lin, H.; Kuang, H.; Xu, C. Emerging Trends in Chiral Inorganic Nanomaterials for Enantioselective Catalysis. Nat. Commun. 2024, 15 (1), 3506. https://doi.org/10.1038/s41467-024-47657-y.

(5) Bloom, B. P.; Kiran, V.; Varade, V.; Naaman, R.; Waldeck, David. H. Spin Selective Charge Transport through Cysteine Capped CdSe Quantum Dots. Nano Lett. 2016, 16 (7), 4583–4589. https://doi.org/10.1021/acs.nanolett.6b01880.

(6) Cho, N. H.; Byun, G. H.; Lim, Y.-C.; Im, S. W.; Kim, H.; Lee, H.-E.; Ahn, H.-Y.; Nam, K. T. Uniform Chiral Gap Synthesis for High Dissymmetry Factor in Single Plasmonic Gold Nanoparticle. ACS Nano 2020, 14 (3), 3595–3602. https://doi.org/10.1021/acsnano.9b10094.

(7) Im, S. W.; Kim, R. M.; Han, J. H.; Ha, I. H.; Lee, H.-E.; Ahn, H.-Y.; Jo, E.; Nam, K. T. Synthesis of Chiral Gold Helicoid Nanoparticles Using Glutathione. Nat. Protoc. 2025, 20 (4), 1082–1096. https://doi.org/10.1038/s41596-024-01083-y.

(8) Ha, I. H.; Van Gordon, K.; Girod, R.; Han, J. H.; Vlasov, E.; Baúlde, S.; Mosquera, J.; Nam, K. T.; Bals, S.; Liz-Marzán, L. M. Chiroptical Control of Gold Nanoparticle Growth through Combination of a Multimodal Chirality Inducer and Surfactant Counterion. ACS Nano 2025, 19 (31), 28530–28539. https://doi.org/10.1021/acsnano.5c07744.

(9) Li, T.; Park, H. G.; Lee, H.-S.; Choi, S.-H. Circular Dichroism Study of Chiral Biomolecules Conjugated with Silver Nanoparticles. Nanotechnology 2004, 15 (10), S660. https://doi.org/10.1088/0957-4484/15/10/026.

(10) López-Olivos, J. C.; Álvarez-García, A.; Ramos, G. G.; Huerta, L.; Molina, P.; Heredia-Barbero, A.; Garzón, I. L.; Rodríguez-Zamora, P. Metal–Ligand Interface Effect in the

Chirality Transfer from L- and D-Glutathione to Gold, Silver and Copper Nanoparticles. Nanoscale Adv. 2025, 7 (9), 2648–2662. https://doi.org/10.1039/D5NA00208G.
(11) Sharma, J.; Chhabra, R.; Cheng, A.; Brownell, J.; Liu, Y.; Yan, H. Control of Self-Assembly of DNA Tubules Through Integration of Gold Nanoparticles. Science 2009, 323 (5910), 112–116. https://doi.org/10.1126/science.1165831.
(12) Shen, X.; Song, C.; Wang, J.; Shi, D.; Wang, Z.; Liu, N.; Ding, B. Rolling Up Gold Nanoparticle-Dressed DNA Origami into Three-Dimensional Plasmonic Chiral Nanostructures. J. Am. Chem. Soc. 2012, 134 (1), 146–149. https://doi.org/10.1021/ja209861x.
(13) Kuzyk, A.; Schreiber, R.; Fan, Z.; Pardatscher, G.; Roller, E.-M.; Högele, A.; Simmel, F. C.; Govorov, A. O.; Liedl, T. DNA-Based Self-Assembly of Chiral Plasmonic Nanostructures with Tailored Optical Response. Nature 2012, 483 (7389), 311–314. https://doi.org/10.1038/nature10889.
(14) Yan, W.; Xu, L.; Xu, C.; Ma, W.; Kuang, H.; Wang, L.; Kotov, N. A. Self-Assembly of Chiral Nanoparticle Pyramids with Strong R/S Optical Activity. J. Am. Chem. Soc. 2012, 134 (36), 15114–15121. https://doi.org/10.1021/ja3066336.
(15) Li, Z.; Zhu, Z.; Liu, W.; Zhou, Y.; Han, B.; Gao, Y.; Tang, Z. Reversible Plasmonic Circular Dichroism of Au Nanorod and DNA Assemblies. J. Am. Chem. Soc. 2012, 134 (7), 3322–3325. https://doi.org/10.1021/ja209981n.
(16) Moloney, M. P.; Gun'ko, Y. K.; Kelly, J. M. Chiral Highly Luminescent CdS Quantum Dots. Chem. Commun. 2007, No. 38, 3900–3902. https://doi.org/10.1039/B704636G.
(17) Tohgha, U.; Deol, K. K.; Porter, A. G.; Bartko, S. G.; Choi, J. K.; Leonard, B. M.; Varga, K.; Kubelka, J.; Muller, G.; Balaz, M. Ligand Induced Circular Dichroism and Circularly Polarized Luminescence in CdSe Quantum Dots. ACS Nano 2013, 7 (12), 11094–11102. https://doi.org/10.1021/nn404832f.
(18) Tohgha, U.; Varga, K.; Balaz, M. Achiral CdSe Quantum Dots Exhibit Optical Activity in the Visible Region upon Post-Synthetic Ligand Exchange with D- or L-Cysteine. Chem. Commun. 2013, 49 (18), 1844–1846. https://doi.org/10.1039/C3CC37987F.
(19) Liu, M.; Li, G.; Wei, S.; Liu, H.; Yang, G. Ligand-Induced Chiroptical Properties in Nanocrystals with Different Core–Shell Band Structures. ACS Appl. Nano Mater. 2025, 8 (4), 1843–1851. https://doi.org/10.1021/acsanm.4c06205.
(20) Zhou, Y.; Marson, R. L.; van Anders, G.; Zhu, J.; Ma, G.; Ercius, P.; Sun, K.; Yeom, B.; Glotzer, S. C.; Kotov, N. A. Biomimetic Hierarchical Assembly of Helical Supraparticles from Chiral Nanoparticles. ACS Nano 2016, 10 (3), 3248–3256. https://doi.org/10.1021/acsnano.5b05983.
(21) Feng, W.; Kim, J.-Y.; Wang, X.; Calcaterra, H. A.; Qu, Z.; Meshi, L.; Kotov, N. A. Assembly of Mesoscale Helices with Near-Unity Enantiomeric Excess and Light-Matter Interactions for Chiral Semiconductors. Sci. Adv. 2017, 3 (3), e1601159. https://doi.org/10.1126/sciadv.1601159.
(22) Yan, J.; Feng, W.; Kim, J.-Y.; Lu, J.; Kumar, P.; Mu, Z.; Wu, X.; Mao, X.; Kotov, N. A. Self-Assembly of Chiral Nanoparticles into Semiconductor Helices with Tunable near-Infrared Optical Activity. Chem. Mater. 2020, 32 (1), 476–488. https://doi.org/10.1021/acs.chemmater.9b04143.
(23) Spangler, L. C.; Yao, Y.; Cheng, G.; Yao, N.; Chari, S. L.; Scholes, G. D.; Hecht, M. H. A de Novo Protein Catalyzes the Synthesis of Semiconductor Quantum Dots. Proc. Natl. Acad. Sci. 2022, 119 (51), e2204050119. https://doi.org/10.1073/pnas.2204050119.

(24) Yao, Y.; Wu, J.; Hu, Y.; Haubold, L.; Uzosike, O.; Cheng, G.; Yao, N.; Scholes, G. D.; Hecht, M. H.; Spangler, L. C. De Novo Proteins Template the Formation of Semiconductor Quantum Dots. ACS Cent. Sci. 2025. https://doi.org/10.1021/acscentsci.4c01826.
(25) Lowe, C. D.; Larson, H. C.; Cai, Y.; Chiang, H. T.; Pozzo, L. D.; Baneyx, F.; Cossairt, B. M. Induced Chirality in QDs Using Thermoresponsive Elastin-like Polypeptides. Langmuir 2025, 41 (1), 1047–1056. https://doi.org/10.1021/acs.langmuir.4c04339.
(26) Kuznetsova, V. A.; Mates-Torres, E.; Prochukhan, N.; Marcastel, M.; Purcell-Milton, F.; O'Brien, J.; Visheratina, A. K.; Martinez-Carmona, M.; Gromova, Y.; Garcia-Melchor, M.; Gun'ko, Y. K. Effect of Chiral Ligand Concentration and Binding Mode on Chiroptical Activity of CdSe/CdS Quantum Dots. ACS Nano 2019, 13 (11), 13560–13572. https://doi.org/10.1021/acsnano.9b07513.
(27) Varga, K.; Tannir, S.; Haynie, B. E.; Leonard, B. M.; Dzyuba, S. V.; Kubelka, J.; Balaz, M. CdSe Quantum Dots Functionalized with Chiral, Thiol-Free Carboxylic Acids: Unraveling Structural Requirements for Ligand-Induced Chirality. ACS Nano 2017, 11 (10), 9846–9853. https://doi.org/10.1021/acsnano.7b03555.
(28) Choi, J. K.; Haynie, B. E.; Tohgha, U.; Pap, L.; Elliott, K. W.; Leonard, B. M.; Dzyuba, S. V.; Varga, K.; Kubelka, J.; Balaz, M. Chirality Inversion of CdSe and CdS Quantum Dots without Changing the Stereochemistry of the Capping Ligand. ACS Nano 2016, 10 (3), 3809–3815. https://doi.org/10.1021/acsnano.6b00567.
(29) Puri, M.; Ferry, V. E. Circular Dichroism of CdSe Nanocrystals Bound by Chiral Carboxylic Acids. ACS Nano 2017, 11 (12), 12240–12246. https://doi.org/10.1021/acsnano.7b05690.
(30) Ben-Moshe, A.; Teitelboim, A.; Oron, D.; Markovich, G. Probing the Interaction of Quantum Dots with Chiral Capping Molecules Using Circular Dichroism Spectroscopy. Nano Lett. 2016, 16 (12), 7467–7473. https://doi.org/10.1021/acs.nanolett.6b03143.
(31) Gao, X.; Zhang, X.; Deng, K.; Han, B.; Zhao, L.; Wu, M.; Shi, L.; Lv, J.; Tang, Z. Excitonic Circular Dichroism of Chiral Quantum Rods. J. Am. Chem. Soc. 2017, 139 (25), 8734–8739. https://doi.org/10.1021/jacs.7b04224.
(32) Roberts, S.; Dzuricky, M.; Chilkoti, A. Elastin-like Polypeptides as Models of Intrinsically Disordered Proteins. FEBS Lett. 2015, 589 (19, Part A), 2477–2486. https://doi.org/10.1016/j.febslet.2015.08.029.
(33) Shen, H.; Fallas, J. A.; Lynch, E.; Sheffler, W.; Parry, B.; Jannetty, N.; Decarreau, J.; Wagenbach, M.; Vicente, J. J.; Chen, J.; Wang, L.; Dowling, Q.; Oberdorfer, G.; Stewart, L.; Wordeman, L.; De Yoreo, J.; Jacobs-Wagner, C.; Kollman, J.; Baker, D. De Novo Design of Self-Assembling Helical Protein Filaments. Science 2018, 362 (6415), 705–709. https://doi.org/10.1126/science.aau3775.
(34) Shen, H.; Lynch, E. M.; Akkineni, S.; Watson, J. L.; Decarreau, J.; Bethel, N. P.; Benna, I.; Sheffler, W.; Farrell, D.; DiMaio, F.; Derivery, E.; De Yoreo, J. J.; Kollman, J.; Baker, D. De Novo Design of pH-Responsive Self-Assembling Helical Protein Filaments. Nat. Nanotechnol. 2024, 19 (7), 1016–1021. https://doi.org/10.1038/s41565-024-01641-1.
(35) Hu, J.; Li, L.; Yang, W.; Manna, L.; Wang, L.; Alivisatos, A. P. Linearly Polarized Emission from Colloidal Semiconductor Quantum Rods. Science 2001, 292 (5524), 2060–2063. https://doi.org/10.1126/science.1060810.

(36) Hu, J.; Wang; Li, L.; Yang, W.; Alivisatos, A. P. Semiempirical Pseudopotential Calculation of Electronic States of CdSe Quantum Rods. J. Phys. Chem. B 2002, 106 (10), 2447–2452. https://doi.org/10.1021/jp013204q.
(37) Saunders, A. E.; Ghezelbash, A.; Sood, P.; Korgel, B. A. Synthesis of High Aspect Ratio Quantum-Size CdS Nanorods and Their Surface-Dependent Photoluminescence. Langmuir 2008, 24 (16), 9043–9049. https://doi.org/10.1021/la800964s.
(38) Krepkiy, D.; Försterling, F. H.; Petering, D. H. Interaction of Cd2+ with Zn Finger 3 of Transcription Factor IIIA: Structures and Binding to Cognate DNA. Chem. Res. Toxicol. 2004, 17 (7), 863–870. https://doi.org/10.1021/tx030057+.
(39) Malgieri, G.; Palmieri, M.; Esposito, S.; Maione, V.; Russo, L.; Baglivo, I.; Paola, I. de; Milardi, D.; Diana, D.; Zaccaro, L.; Pedone, P. V.; Fattorusso, R.; Isernia, C. Zinc to Cadmium Replacement in the Prokaryotic Zinc-Finger Domain. Metallomics 2013, 6 (1), 96–104. https://doi.org/10.1039/C3MT00208J.
(40) Brandis, J. E. P.; Zalesak, S. M.; Kane, M. A.; Michel, S. L. J. Cadmium Exchange with Zinc in the Non-Classical Zinc Finger Protein Tristetraprolin. Inorg. Chem. 2021, 60 (11), 7697–7707. https://doi.org/10.1021/acs.inorgchem.0c03808.
(41) Slocik, J. M.; Govorov, A. O.; Naik, R. R. Plasmonic Circular Dichroism of Peptide-Functionalized Gold Nanoparticles. Nano Lett. 2011, 11 (2), 701–705. https://doi.org/10.1021/nl1038242.
(42) Lu, F.; Tian, Y.; Liu, M.; Su, D.; Zhang, H.; Govorov, A. O.; Gang, O. Discrete Nanocubes as Plasmonic Reporters of Molecular Chirality. Nano Lett. 2013, 13 (7), 3145–3151. https://doi.org/10.1021/nl401107g.
(43) Martynenko, I. V.; Baimuratov, A. S.; Osipova, V. A.; Kuznetsova, V. A.; Purcell-Milton, F.; Rukhlenko, I. D.; Fedorov, A. V.; Gun'ko, Y. K.; Resch-Genger, U.; Baranov, A. V. Excitation Energy Dependence of the Photoluminescence Quantum Yield of Core/Shell CdSe/CdS Quantum Dots and Correlation with Circular Dichroism. Chem. Mater. 2018, 30 (2), 465–471. https://doi.org/10.1021/acs.chemmater.7b04478.
(44) Purcell-Milton, F.; Visheratina, A. K.; Kuznetsova, V. A.; Ryan, A.; Orlova, A. O.; Gun'ko, Y. K. Impact of Shell Thickness on Photoluminescence and Optical Activity in Chiral CdSe/CdS Core/Shell Quantum Dots. ACS Nano 2017, 11 (9), 9207–9214. https://doi.org/10.1021/acsnano.7b04199.
(45) Knauf, R. R.; Lennox, J. C.; Dempsey, J. L. Quantifying Ligand Exchange Reactions at CdSe Nanocrystal Surfaces. Chem. Mater. 2016, 28 (13), 4762–4770. https://doi.org/10.1021/acs.chemmater.6b01827.
(46) Baker, D. R.; Kamat, P. V. Tuning the Emission of CdSe Quantum Dots by Controlled Trap Enhancement. Langmuir 2010, 26 (13), 11272–11276. https://doi.org/10.1021/la100580g.
(47) Hässelbarth, A.; Eychmüller, A.; Weller, H. Detection of Shallow Electron Traps in Quantum Sized CdS by Fluorescence Quenching Experiments. Chem. Phys. Lett. 1993, 203 (2), 271–276. https://doi.org/10.1016/0009-2614(93)85400-I.
(48) Ma, W.; Xu, L.; de Moura, A. F.; Wu, X.; Kuang, H.; Xu, C.; Kotov, N. A. Chiral Inorganic Nanostructures. Chem. Rev. 2017, 117 (12), 8041–8093. https://doi.org/10.1021/acs.chemrev.6b00755.
(49) Wang, F.; Tang, R.; Buhro, W. E. The Trouble with TOPO; Identification of Adventitious Impurities Beneficial to the Growth of Cadmium Selenide Quantum Dots,

Rods, and Wires. Nano Lett. 2008, 8 (10), 3521–3524. https://doi.org/10.1021/nl801692g.
(50) Hamachi, L. S.; Yang, H.; Plante, I. J.-L.; Saenz, N.; Qian, K.; Campos, M. P.; Cleveland, G. T.; Rreza, I.; Oza, A.; Walravens, W.; Chan, E. M.; Hens, Z.; Crowther, A. C.; Owen, J. S. Precursor Reaction Kinetics Control Compositional Grading and Size of CdSe1−xSx Nanocrystal Heterostructures. Chem. Sci. 2019, 10 (26), 6539–6552. https://doi.org/10.1039/C9SC00989B.
(51) Yu, W. W.; Qu, L.; Guo, W.; Peng, X. Experimental Determination of the Extinction Coefficient of CdTe, CdSe, and CdS Nanocrystals. Chem. Mater. 2003, 15 (14), 2854–2860. https://doi.org/10.1021/cm034081k.

VITA

Chris grew up in Windsor, California with his parents Dave and Sonja and his younger sister, Kayla, and his two younger brothers, Derek and Dylan. His passion for chemistry developed during his time working at a water treatment plant while taking part time classes at a local community college. He started his full-time education in 2015 at Santa Rosa Junior college before attending University of California-Davis. During his time at UC Davis he developed a passion for inorganic chemistry and began his research under the tutelage of Professor Alan Balch where he worked on the synthesis and characterization of molecular gold complexes. He then attended the University of Washington where he continued his passion for inorganic chemistry under the mentorship of professor Brandi Cossairt. Outside of lab Chris enjoys playing tennis and weightlifting.

.